GA-ASSISTED NANOWIRE GROWTH ON NANO-PATTERNED SILICON

GA-ASSISTED NANOWIRE GROWTH ON NANO-PATTERNED SILICON

By SANDRA JEAN GIBSON, M.Sc.

A Thesis

Submitted to the School of Graduate Studies

in Partial Fulfillment of the Requirements

for the Degree of

Doctor of Philosophy

McMaster University

DOCTOR OF PHILOSOPHY (2014) McMaster University

(Engineering Physics) Hamilton, Ontario

TITLE: Ga-Assisted Nanowire Growth on Nano-patterned Silicon

AUTHOR: Sandra Jean Gibson, B.Sc. Physics (Acadia University), M.Sc. Physics (Laurentian University)

SUPERVISOR: Dr. R.R. LaPierre

NUMBER OF PAGES: xvii, 137

Abstract

GaAs nanowires (NW) have been grown on Si (111) substrates by the self-assisted vapor-liquid-solid (VLS) mechanism using molecular beam epitaxy (MBE). Substrates were prepared with nano-patterned oxide templates using electron beam lithography (EBL) in order to achieve position controlled NW growth.

Early experiments uncovered several key issues with regards to the patterning process. Cross-sectional lamella prepared using the focused-ion beam (FIB) technique were used to study the NW-substrate interface using transmission electron microscopy (TEM). Undesirable growth outcomes were found to be caused in part by an unintended residual layer of oxide. Uniform NW dimensions were then obtained by improving the pattern transfer method. The effects of deposition parameters on the growth results were then explored in further experiments.

The first systematic study of the axial and radial growth rates of vertical NWs in the positioned array was conducted. It was proposed that the observed expansion of the Ga droplet in Ga-rich growth conditions results in a slight inverse tapered morphology, promoting significant radial growth. While the growth rates were shown to be approximately constant in time, their measured values were found to increase with increasing pattern pitch and decrease with increasing hole diameter.

A phenomenological model was then developed based on the principle of mass conservation. A fit to the experimental data was obtained by calculating the collection of

growth material supplied by a secondary flux of both gallium and arsenic species desorbing from the oxide surface between the NWs, subsequently impinging on the liquid droplet and NW sidewalls. The reduction of this contribution due to shading of the incident and scattered flux by neighboring NWs in the array was able to account for the differences in final NW morphologies observed with increasing pattern pitch. This model demonstrates the significant impact of secondary adsorption in patterned self-assisted NW growth.

Acknowledgements

First of all, I would like to thank my supervisor Dr. Ray LaPierre. Through the low points when experiments were delayed or just didn't turn out as expected, his openness both reassured and motivated me to push through. His legendary promptness and discerning attention to detail will always be remembered. He allowed me the freedom to be creative while also reining me in when it was needed. Beyond the mechanics of good research, he facilitated and guided me through many other great opportunities for professional development. I really don't think I could have asked for a better supervisor. I would also like to thank my committee members Dr. Knights and Dr. Kleiman for their direction and input along the path of this work.

It is difficult to fully express my appreciation for all the members of the LaPierre Group, both past and present. Jonathan Boulanger, Chris Haapamaki and Andrew Chia were especially influential for all the training and support they have given me during this time. Each of them was always willing to discuss issues and provide perspective whenever I needed it. Robin Yee, Paul Kuyanov, Junpeng Zhang and Aziz Rahman were also such great comrades, it really could not have been the same without them.

I would like to acknowledge all the technical support which made the experiments presented in this thesis possible. So many people had a hand in this, including Shahram Tavakoli, Doris Stevanovic and Zhilin Peng at Centre for Emerging Technologies; Carmen Andrei, Fred Pearson, Chris Butcher and Julia Huang at Canadian Centre for Electron Microscopy; as well as Aju Jugessur, Alexander Tsukernik and Harlan

Kuntz at the Toronto Nanofabrication Center. Their expertise in operating and maintaining equipment, in addition to providing training and advice, was simply crucial.

So many collaborators also helped to add breadth and depth to this work through various experiments and discussions. I would like to specifically acknowledge Martin Aagesen, Simon Watkins, Ali Darbandi, Vladimir Dubrovskii, Peter Krogstrup, Anna Fontcuberta i Morral and Jean-Christophe Harmand, among many others.

To my family (including my awesome friends); you have each supported and added to me in your individual ways over these years. To my Mom and Dad especially, you never constrained me with expectations or opinions on what career path I should follow, but always encouraged and believed in me no matter what. In ten years of 'higher' education after high-school I have certainly deepened my knowledge of Physics, but all that can't come close to what I have learned about life from you guys back on the Farm. Besides, we all know I got this brain from somewhere, right?

Finally, to my wonderful husband, Jon. Despite our comfortable position and your bright career in Sudbury, you put it all on the line to relocate away from the mines and give me this opportunity. This thesis would never have been started without your courage and trust, and in the end it could never have been completed without your patience, love and abundant grace. I am so glad God put us on this path together and I wouldn't have done it any other way but with you.

This work is dedicated to my husband, Jonathan.

Table of Contents

List of Figures

1 Background

1.1 Introduction

Sufficiently reducing the size of a crystalline structure down to the nanoscale ($1x10^{-9}$ m) can have dramatic implications for its properties, behavior and potential applications. A nanowire (NW) is a one-dimensional nanostructure with a constrained diameter, typically in the tens of nanometers, and with unconstrained length usually on the scale of several microns. Physicists have recognized the value of these nanostructures for a variety of fundamental research in recent years, using them to realize spin qubits [1] and probe for signatures of Majorana fermions [2].

The idea of using self-assembled nanostructures to overcome the pressing limitations of conventional top-down planar device fabrication has been another main driving force behind the lively and sustained engineering interest in semiconducting NWs. Their unique geometry makes possible the realization of novel device architectures and improved performance capabilities. Many examples of NW-based electronic and optoelectronic devices have recently been demonstrated [3], including lasers [4,5], photodetectors [6], light emitting diodes (LEDs) [7], photovolatic cells [8,9], wrap gate transistors [10], high electron mobility transistors (HEMTs) [11] and single electron transistors [12]. However, for NW-based devices to truly contribute to future

post-complementary metal-oxide-semiconductor (CMOS) technologies, various issues surrounding scale-up and integration within large hierarchical systems must be solved.

This Chapter begins with an outline of the essential concepts surrounding bottom-up NW growth in Section 1.2. This concentrates mainly on self-assisted NW growth, which is used exclusively in this thesis, although understanding stemming from Au-seeded growth is included where appropriate. Comparisons are often made with Au-assisted results due to the prevalence and maturity of the Au-seeded method. Therefore, this discussion also highlights the intuitive commonalities as well as significant differences between these growth modes. Key features of the vapor-liquid-solid (VLS) mechanism are outlined in Section 1.2.1, followed by a summary in Section 1.2.2 of the factors which determine the resulting crystal structure and growth orientation. The technologically important concepts of lattice mismatch accommodation in NWs and the formation of unique junction geometries are introduced in Section 1.2.3. Random growth of self-assisted arrays is reviewed and the expected benefits of patterning for the fabrication of uniform NW arrays will be detailed in Section 1.2.4. The Chapter is concluded by an overview of the motivations behind the presented thesis in Section 1.3 and an outline of the contributions resulting from this work in Section 1.4.

1.2 Fundamentals of Nanowire Growth

1.2.1 Vapor-Liquid-Solid Mechanism

In 1964 Wagner and Ellis [13] of Bell Laboratories reported on the growth of silicon NWs by chemical vapor deposition (CVD) and introduced the so-called vapor-

liquid-solid (VLS) mechanism of NW growth. Nearly half a century later the VLS mechanism is still most the successful mode to generate large quantities of NWs with single crystalline structure [14,15]. The VLS mechanism emphasizes the role of liquid metallic particles in promoting an accelerated crystal growth rate along one dimension during vapor phase material deposition.

Initially, a liquid metal particle assembles on top of the heated substrate surface. Once the growth species are introduced into the chamber they begin to deposit onto the particle surface, forming a liquid alloy with it. As growth species are continually supplied from the constant vapor overpressure on the surface of the substrate, the system is pushed far out of equilibrium. The liquid eventually becomes supersaturated, providing the thermodynamic driving force for crystallization. Once a critical supersaturation level is achieved, nucleation occurs at the liquid-solid interface, resulting in precipitation of a crystalline layer beneath the droplet. Steady material delivery and preferential collection of growth species by the liquid phase maintains the growth beneath the droplet, which is then lifted up from the substrate surface. The diameter of the crystalline pillar is dictated primarily by the size and shape of the liquid droplet.

The most commonly used seed metal for semiconductor NW growth is by far gold (Au). The current dominance of Au for this purpose has been propelled in part by its reliable experimental performance and excellent material properties. For example, Au forms low temperature liquid alloys with many materials of interest including Si, Ga and In, and is relatively inert and so does not react with common gas-phase carriers including nitrogen, hydrogen and oxygen (or with most common solvents) [16].

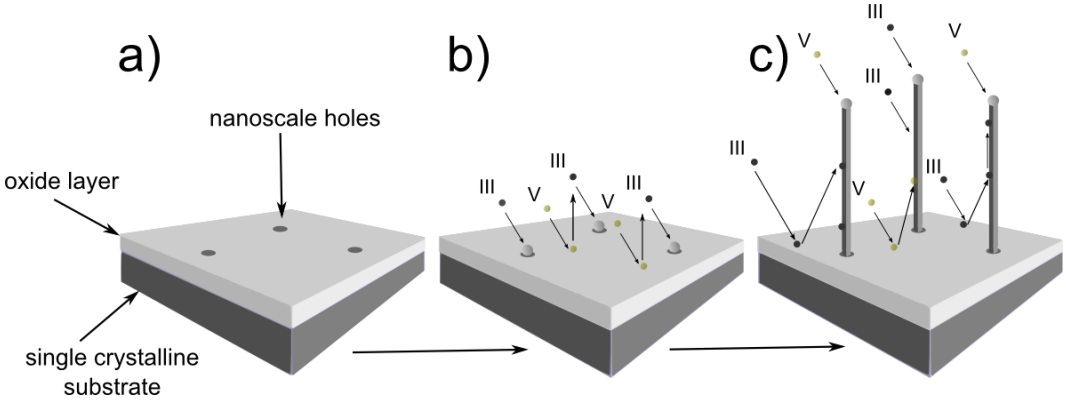

Figure 1.1: The self-assisted VLS growth mechanism. (a) Nanoscale holes are formed in an oxide layer on the substrate, reaching down to the underlying single-crystalline substrate. (b) Early during the deposition, or during a controlled pre-deposition of group-III species, droplets of liquid group-III species collect in the holes. (c) The droplets collect group-V species, eventually becoming supersaturated and precipitating the solid NW material beneath the droplet, lifting it up from the substrate. Continued layer-by-layer growth beneath the droplet forms crystalline pillars.

However, there has been a recent and rapid movement in the field of NW growth away from the use of Au seeds and towards Au-free growth methods, including so-called “self-assisted” NW growth [17–20]. This approach is attractive since it removes the risk of either substrate or nanowire contamination by the foreign seed material (i.e., Au) during growth by instead using a droplet formed from the group-III component of the NW itself.

The typical self-assisted growth process is illustrated in Figure 1.1. The substrate surface is first generally covered with a non-wetting layer (Figure 1.1 (a)), ideally with a negligible sticking coefficient of both group-III and group-V adatoms. This layer is intended to facilitate droplet formation and also inhibit accompanying parasitic film growth. Generally an oxide such as SiO_x is used for self-assisted growth on single crystalline III-V or Si substrates. Nanoscale openings which extend through this layer

down to the substrate surface are believed to be key to droplet collection and immobilization and enable the initial contact with the substrate surface required for epitaxial growth. For the growth of random arrays, these holes may be formed in situ as pinholes in a very thin or native oxide layer, most commonly by Ga-assisted deoxidization [21–24]. Alternatively, a thicker layer (typically tens of nm) may be patterned with nanoscale openings using advanced lithographic techniques, facilitating the growth of positioned NW arrays [25–27]. These two methods will be discussed further in Section 1.2.4. Group-III droplet collection occurs either during the early phase of the deposition or during a controlled pre-deposition of group-III material only (Figure 1.1 (b)), and is followed by the nucleation and growth of the NW crystal (Figure 1.1 (c)). In the just over half a decade since the preliminary works of A. Fontcuberta i Morral et al. [17,18] popularized this method, the self-assisted growth of NWs of many III-V materials have been demonstrated [28], including InAs [27,29], InP [30], InSb [31], GaAs [18] and several related ternaries [32–34].

The kinetics of crystallization by VLS have been extensively studied [35–37], and it is generally understood to proceed via the nucleation and lateral extension of two-dimensional islands at the liquid-solid interface. For NWs with relatively small diameters (< 100 nm) the expansion and spreading of a single nucleus across the entire top facet is generally rapid, establishing a mononuclear growth regime under most conditions. The details of the nucleation process therefore fundamentally mediate the one-dimensional (axial) growth of the NW through the accumulation of stacked crystalline monolayers.

During conventional Au-seeded NW growth, the droplet preferentially collects group-III material until the critical liquid supersaturation condition is reached. When the overall growth rate is dictated by the supply of group-III material replenishing the droplet in an excess of group-V, the growth is group-III limited. Details of the mass transport mechanism are often manifest in the length-radius $(L-R)$ dependence, having a characteristic shape determined by the active pathways by which the group-III adatoms reach the droplet, such as direct-impingement $(L \propto R)$ [38], or sidewall or surface diffusion $\left(L \propto 1/R\,, 1/R^2\right)$ [39–41]. More comprehensive treatments account for the full time-dependence of the growth rate [36,37,42] and finite size considerations such as the Gibbs-Thompson effect [43].

In an analogous manner, self-assisted NW growth is group-V limited, so that the axial growth rate increases with increasing group-V flux [17,44]. A simulation of the evolution of the arsenic concentration in the gallium droplet during the initial stages of Ga-assisted GaAs NW growth (adapted from Ref. [36]) is illustrated in Figure 1.2. Arsenic is dissolved into the liquid Ga phase until the critical concentration is reached. Due to the nano-sized volume of the droplet, the As concentration dips significantly as each individual nucleation event takes place, giving the plot a sawtooth appearance. As the V/III ratio (incoming As flux) is increased, the time required to replenish the droplet is decreased, and the growth proceeds at a faster rate.

However, the second key difference which separates the self-assisted mode from Au-assisted growth is the truly dynamic nature of the group-III seed droplet. Since

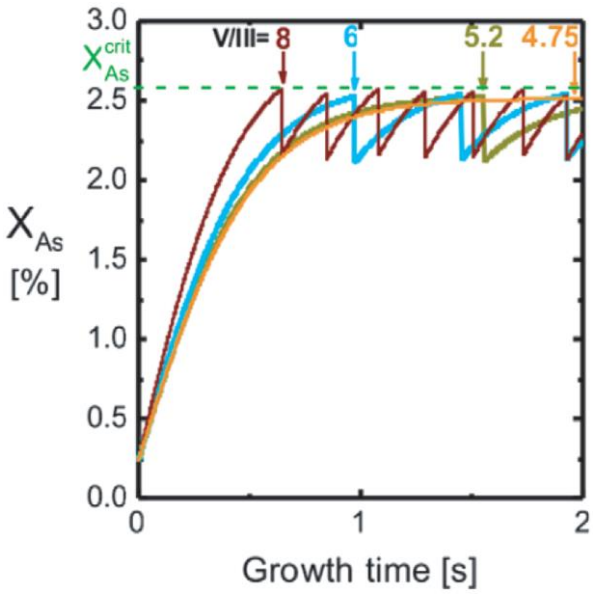

Figure 1.2: A simulation showing the As molar fraction $X_{As}(\%)$ in the liquid (Ga, As) phase during the first few seconds of deposition under different V/III flux ratios. As the droplet collects As, the concentration increases until it reaches the critical level $\left(X_{As}^{crit}\right)$. A nucleation event depletes the droplet of As and a finite amount of time is required to recover to the critical supersaturation level, generally occurring at a faster rate for higher V/III ratios. Adapted from [36].

the amount of Au in the seed is fixed, it typically acts as a volume reservoir which helps to mitigate large changes in droplet size during Au-assisted growth. However, depending on the deposition conditions, the Ga droplet can progressively inflate, deflate or eventually reach some average value during Ga-assisted NW growth [36,45,46]. For low effective V/III flux ratios, the droplet size generally increases with time as more Ga is incorporated into the droplet than is removed from it by the crystallization of each new layer. However, if the amount of Ga reaching the droplet is insufficient to replenish the volume lost to NW growth, the droplet will shrink with time and may even be entirely

consumed [45,46]. This can strongly affect the resulting NW morphology, with tapered and inverse tapered as well as cylindrical wires being produced depending largely on the effective V/III flux ratio reaching the droplet [25,36]. This also has very important consequences for the evolution of the crystal structure as the NW grows.

1.2.2 Crystal Structure and Growth Orientation

In early Au-assisted NW growth studies, uncontrolled polytypism was commonly observed in the growth of III-V semiconductors, with the unexpected appearance of the hexagonal wurtzite (WZ) phase in normally cubic zinc blende (ZB) structured materials. The difference between WZ and ZB crystal structures is easiest to understand in terms of stacking of bilayers (III-V pairs). The ZB phase follows an ABCABC type stacking whereas WZ follows an ABABAB sequence, as illustrated in Figure 1.3 (a). These polytypes have different optical and electronic properties [47,48], therefore understanding the formation mechanism is key to achieving structural control during VLS growth.

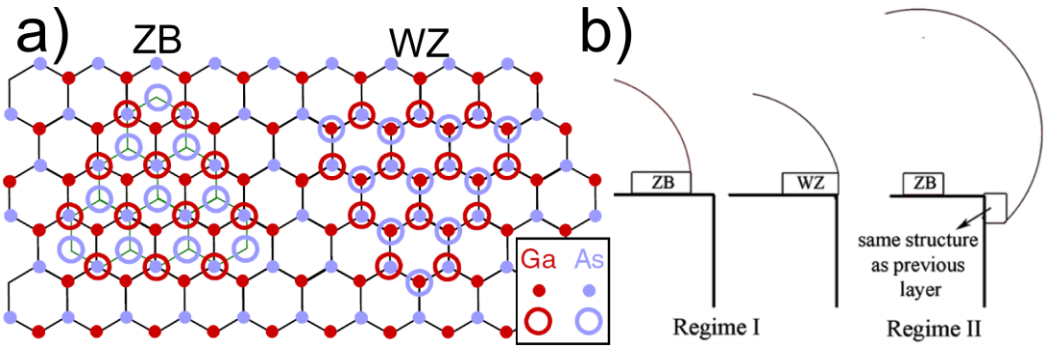

Figure 1.3: (a) The atomic positions in ZB and WZ stacked structures (open circles) on top of a single (111)B bilayer. Adapted from [49]. (b) A simplified illustration of the preferred crystal structure (wurtzite (WZ) or zincblende (ZB)) formed for nucleation at different positions and for different droplet shapes. Adapted from [50].

This understanding was initially provided by Glas et al. [49], who showed that subtle differences in interfacial energy favored the formation of a nucleus at the triple-phase-line (TPL) where the NW, Au-droplet and vapor meet at the edge of the NW facet. The energetics of TPL nucleation also favored WZ stacking, which explained the prevalence of this phase in Au-assisted NW growth. However, nucleation may occur away from the TPL if the liquid surface energy is sufficiently small and the droplet contact angle sufficiently large, favoring the ZB phase. Finally, if the TPL recedes from the NW side facets, the ZB phase is also favored. Each of these generalized regimes are illustrated in Figure 1.3 (b). More comprehensive statistical treatments have been developed which account for the nucleation probabilities of each phase given the droplet size, liquid surface energy and contact angle [36,50]. Therefore changes in droplet size as the growth progresses can strongly affect the resulting NW crystal structure.

When WZ is the dominant structure, stacking faults (single misplaced bilayers) are the main planar crystallographic defect which are observed. However, when ZB is the dominant structure, twin planes can also occur when the overall stacking sequence reverses (I.e ABCA*C*BA) after a flaw in the positioning of a bilayer. Effectively, the twin crystal is rotated by 60° about the [111]B growth axis relative to its neighbor. Avoiding these defects is generally desirable since the change in symmetry experienced traversing these defects may detrimentally affect the electronic properties [51,52].

Ga-assisted NWs are predominately found to form with the ZB phase [48,53]. This is due to the lower surface energy of the Ga droplet, which favors the wetting of

the droplet on the sidewalls of the growing NW [50,54] and large droplet contact angles under typical growth conditions. However, as mentioned in Section 1.2.1, changes in the effective V/III ratio during growth can lead to transitions in the droplet shape and therefore crystal structure from ZB to WZ back to ZB. In fact, control of the crystal structure, including the elimination of twin planes, has been demonstrated by tuning of the V/III flux ratio during growth [48,55].

The NW crystal grows in the direction which minimizes the total free energy, which is normally dominated by the surface free energy between the solid and the liquid phase. For a ZB structure, the lowest energy surface is normally the (111) plane and the NW growth generally occurs along one of the <111> directions [56]. Care must therefore be taken in the choice of substrate crystal orientation, as this determines the preferred orientations of the NWs grown on it (i.e. angle with respect to the substrate plane). When dealing with III-V compounds, crystal plane surfaces can be either terminated with group-III or group-V atomic layers (A and B polarity, respectively). Therefore, NW growth on zincblende (111)B substrates typically prefers the 90° or perpendicular (also often called vertical) orientation, as the B polarity yields the lowest surface energy. However, when growing III-V NWs on Si substrates with a non-polar diamond structure, all the (111) planes are equivalent. If a single seed with A polarity forms, the NWs will still prefer to grow along (111)B, but this will now require a tilt to a 19.5° orientation with respect to the substrate plane [57]. In fact, for Si there are three equivalent 19.5° tilted out of plane orientation possibilities separated by a 120° azimuthal angle in addition to the perpendicular <111> direction. Therefore, attaining

aligned growth on Si substrates often requires very careful tuning of growth conditions [58].

However, in self-assisted NW growth a manifold of different growth directions are often observed, and although the observed angles are quantized many of them do not have a direct epitaxial relation to the substrate. The appearance of these additional non-vertical NWs in the array is non-ideal and inconsistent with the crystallography of a single seed nucleus. An explanation for this phenomenon was proposed by Uccelli et al. [57], where the formation of secondary (or multiple order) seeds due to three-dimensional twinning of the original nucleus was shown to open up the possibility of unexpected growth orientations on the newly produced (111)B facets. The growth directions predicted in this scheme were found to correspond to those experimentally measured. So-called crawling NW growth, where the NW does not leave the substrate surface but instead spreads across it, is associated with those resulting growth orientations which point downward into the substrate.

Further studies revealed a link between the V/III ratio during growth and the probability of obtaining undesired non-vertical NW growth [23]. The authors saw a decrease in non-vertical NW growth as the V/III flux ratio was increased. They hypothesized that the larger size of the Ga droplet relative to the seed and/or fast changes in the liquid seed size during the initial stages of the growth increased the probability of both the nucleation of A polarity seeds and subsequent formation of secondary seeds via multiple-order twinning.

1.2.3 Lattice Mismatch Accommodation and Junction Structures

Perhaps one of the most promising aspects of NW growth is the capability to produce heterointerfaces coherently and free of defects despite a large lattice mismatch between materials. This is due to the capacity for efficient elastic relaxation of strain at the nearby sidewall surface, greatly increasing the effective critical layer thickness compared to the corresponding 2D film arrangement. This property can greatly expand practical design flexibility for device engineering using novel material combinations which are unavailable in conventional thin film systems. Dislocation-free growth of Au-assisted NWs on highly mismatched substrates below a critical diameter has been extensively studied experimentally and modeled theoretically [59,60], with an example given in Figure 1.4.

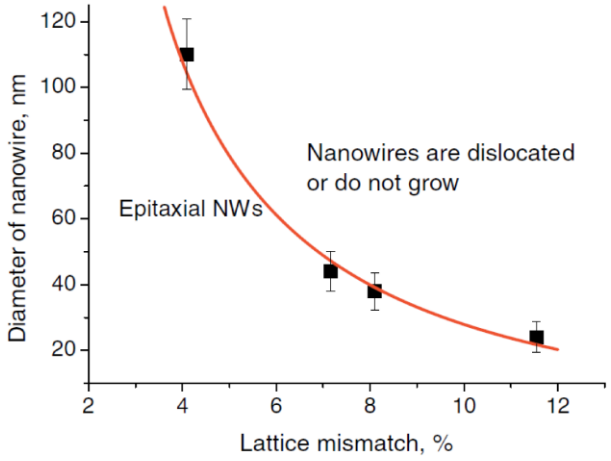

Figure 1.4: Theoretical (red curve) and experimental (data points) indicating the critical NW diameter as a function of the lattice mismatch with the substrate in Au-assisted NW growth by MBE. Adapted from [60].

assisted MBE growth studies [60]. It should be noted that a recent report indicates that this theoretically high value of critical diameter might not correspond for

Ga-assisted GaAs NW growth on Si, perhaps due to the reactivity of the Ga droplet with the Si, such that further study of this system will be needed [61]. However, the possibility of directly integrating high-performance III-V semiconductors on the inexpensive Si platform used in microelectronics holds such enormous potential that it has become the ultimate focus of a large fraction of current NW research, including the work presented in this thesis.

When VLS is the only active growth mode, the diameter of the NW will correspond exactly to the diameter of the seed droplet. For Au-assisted growth, this regime of growth generally results in rod-like NW morphologies. However, in addition to the axial VLS growth mode by which the NW is elongated, there is also the possibility of simultaneous vapor-solid (VS) deposition on the NW sidewall facets, increasing the overall NW diameter. This VS radial growth mode can be either enhanced or suppressed depending on the growth conditions. Specifically, low temperature and high relative V/III ratios were found to favor the formation of island nuclei on GaAs NW sidewall facets and promote radial growth [40].

Precise control of composition (or doping) during growth combined with fine tuning of deposition conditions so as to enhance or suppress the axial and radial growth processes permits the realization of abrupt heterostructures (or analogously p-n junctions) with unique axial and core-shell geometries, as illustrated in Figure 1.5. Axial structures such as quantum wells can be formed with various unique and interesting material combinations by switching or adjusting group-V or group-III species during growth. Coherent growth of axial structures is limited to a critical NW diameter in a

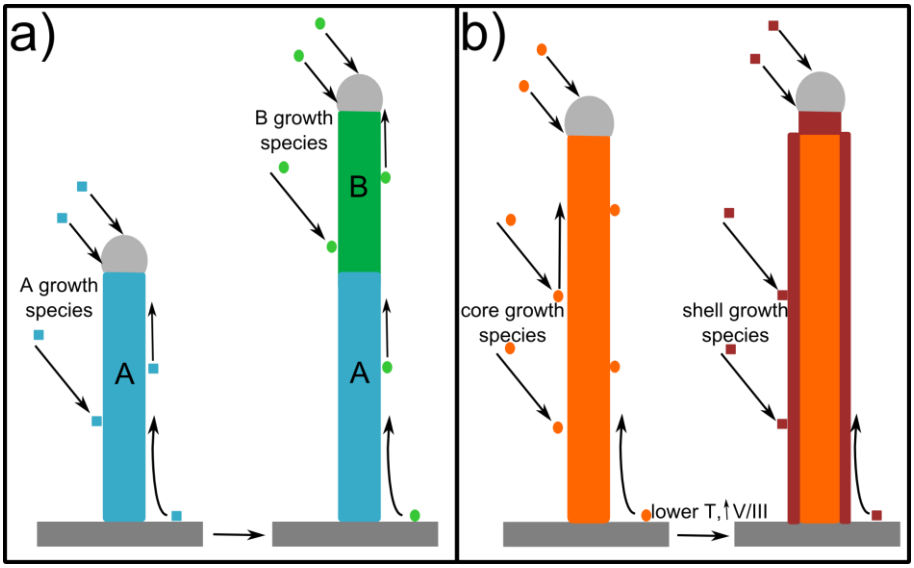

Figure 1.5: Illustration of the formation of (a) axial and (b) core-shell heterostructures (or analogously, p-n junctions) in NWs, by changing the composition (and/or adding dopants) during VLS growth under conditions favoring axial and radial growth respectively.

similar manner as on mismatched substrates [62]. Controlled growth of shell layers can be especially useful for surface passivation, limited to a critical thickness [63,64].

1.2.4 Random Nanowire Growth versus Array Patterning

As mentioned in Section 1.2.1, there are two distinct fabrication options for self-assisted NW growth. The first and most common is the growth of irregular or random NW arrays, which is generally accomplished using a self-assembly process for droplet formation on a thin amorphous oxide layer. Pinholes in the thin layer are generally formed by a process called Ga-assisted deoxidization [21–24], where deposited Ga reacts with and removes the oxide, perhaps pinning on some local defect. Given a thin enough layer, the underlying Si will quickly become exposed within a pinhole, allowing

the collected Ga droplet to establish the contact required for epitaxial VLS growth [18,19]. The oxide may be formed by various processes, such as CVD deposition or sputtering [65] or by annealing of spun hydrogen silsesquioxane (HSQ) layers [24,66]. Thick layers may be subsequently thinned by chemical etching. Although this type of growth on III-V substrates requires deposition of an oxide, Si naturally forms a native oxide (~10 Å thick) on exposure to ambient air. Therefore, an intact native oxide on Si provides a simple and inexpensive substrate for this purpose.

One troublesome issue with this method, however, is that growth results have generally been found to be unreproducible. Identical growths using Si wafers with intact native oxides from wafers purchased from different companies are often found to yield dramatically different results. This issue prompted systematic studies of the detailed role of surface properties. It has been shown that oxide layer thickness (with significant variations on the scale of angstroms), stoichiometry and surface roughness each play sensitive and significant roles in the resulting density and orientation of unpatterned self-assisted NWs [22,24]. This has been very challenging to control in practice.

Another problem is the uncontrolled nature of the NW arrays produced by this method. This can be seen in the example illustrated in Figure 1.6. Not only do many of the NWs grow tilted at undesired non-vertical angles (due to some of the reasons outlined in Section 1.2.3), but the uncontrolled NW diameters and spacing between the NWs leads to a highly inhomogeneous array. Future devices based on NW arrays and heterostructures are likely to demand not only high quality, uniformity and density, but precise control of NW positioning and dimensions.

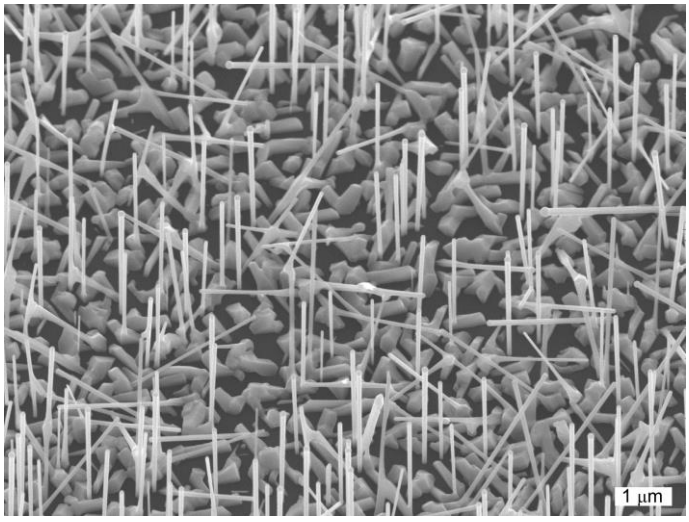

Figure 1.6: Example of unpatterned Ga-assisted GaAs NW growth by MBE on an n-type Si(111) substrate with an intact native oxide layer.

Although NW growth in patterned arrays requires special processing to pattern the mask with nanoscale holes, which often comes with additional effort and cost, it is expected to significantly improve the array uniformity and control over the NW growth which can be achieved. Patterning may also be used as a research tool to help deconvolute the factors which affect NW growth so that important details of the adatom collection environment and growth kinetics may be revealed.

1.3 Motivations of Present Work

The current interest in the development of Au-free NW growth processes is driven predominantly by the desire for the direct integration of NW fabrication processes into the existing Si based industrial framework for widespread commercial applications [20,28]. The conventional use of Au as VLS seed particle, although highly

successful, has been expected to pose a barrier to this goal. As gold impurities in Si form a mid-gap electronic state [67], it can degrade device performance and is therefore usually forbidden in CMOS processing equipment. Currently there is some controversy whether Au appreciably incorporates into III-V NWs during VLS growth or not [68,69], or if this ultimately results in decreased electrical or optical performance [70,71]. However, this type of Au contamination is entirely avoided using the self-assisted VLS method.

As a route towards the integration of III-V materials with existing and future silicon-based technologies, research involving self-assisted NW growth has expanded rapidly. Moving forward, establishing a repeatable method for obtaining uniform, positioned NW arrays with vertically aligned NWs will be essential. The self-assisted growth of positioned GaAs NWs on silicon, which was first demonstrated using lithographically patterned oxide templates by Plissard et al. in 2010 [25], is a potential path in this direction. However, the understanding and control of both the technical and theoretical details of this fabrication method is still quite limited. Therefore, the goal of this work is to develop further insights into these various issues in order to help expand the overall state of the art of this fabrication method.

The use of patterned GaAs NW arrays on Si for the production of lower-cost, high-efficiency solar cells [72,73] is one particularly attractive practical application of this work. Using a radial p-n junction geometry is expected to improve carrier separation and collection across shorter distances [73,74], while a patterned NW array with optimized pitch and NW diameter is able to provide optimal light trapping properties [29]. Therefore, certain features of this work may also contribute to achieving these targets.

1.4 Thesis Overview

In Chapter 2 the experimental methods used in this thesis are described. This includes a summary of the techniques used to prepare patterned substrates and perform the deposition process, as well as the methods which were subsequently used to characterize and study the obtained growth results. In addition to an outline of the practical details relevant to the research presented here, the theoretical foundations of each approach are also briefly reviewed.

Chapter 3 begins with the identification and diagnosis of several key issues related to the substrate patterning process which affect positioned NW growth. This work has been published in Semiconductor Science and Technology in 2013 [75]. Further investigations which isolate other relevant growth parameters are then summarized.

Next, Chapter 4 reports the first systematic study to measure the axial and radial NW growth rates of Ga-assisted GaAs NW arrays on patterned substrates. This study includes an analysis of the effect of pattern parameters such as interwire pitch and hole diameter. This work can be found in published form in Physica Status Solidi [76].

Finally, a phenomenological model was developed to theoretically address the observed pitch dependence of the axial and radial growth rates and is presented in Chapter 5. Applying mass conservation, this work calculates the collection of both As and Ga species, for the first time explicitly accounting for a secondary desorbing flux originating from the oxide mask as well as the effect of shading from the array. This contribution was published as an article in Nanotechnology.

2 Experimental Methods

Each of the experimental methods used in this thesis will be described in this chapter. A brief summary of the basic physical principles underlying each technique will be given, and matters of particular significance to the study of semiconducting NWs will be emphasized with further detail.

2.1 Molecular Beam Epitaxy

The growth of self-assisted NWs presented in this work was performed exclusively using the gas-source molecular beam epitaxy (GS-MBE) system built by SVT Associates and installed in the Centre for Emerging Device Technologies at McMaster University. A simplified illustration of this setup is given in Figure 2.1.

In a conventional MBE system, vapor-phase elemental species are deposited onto a heated substrate in an ultra-high vacuum (UHV) environment (10^{-9} Torr). Comprised of the constituents of the material to be grown, the beam of atoms or molecules do not undergo any collisions in traversing the UHV chamber to the substrate, constituting a 'molecular flow'. The final term, epitaxy, refers to the growth of ordered layers of material whose crystalline structure and alignment are determined by those of the underlying substrate in a well-defined manner.

In GS-MBE, the group III species are provided from high-purity solid material which is evaporated as monomers (Ga, In, Al) through resistive heating in effusion cells. An effusion cell is comprised of a specially designed crucible, typically fabricated using

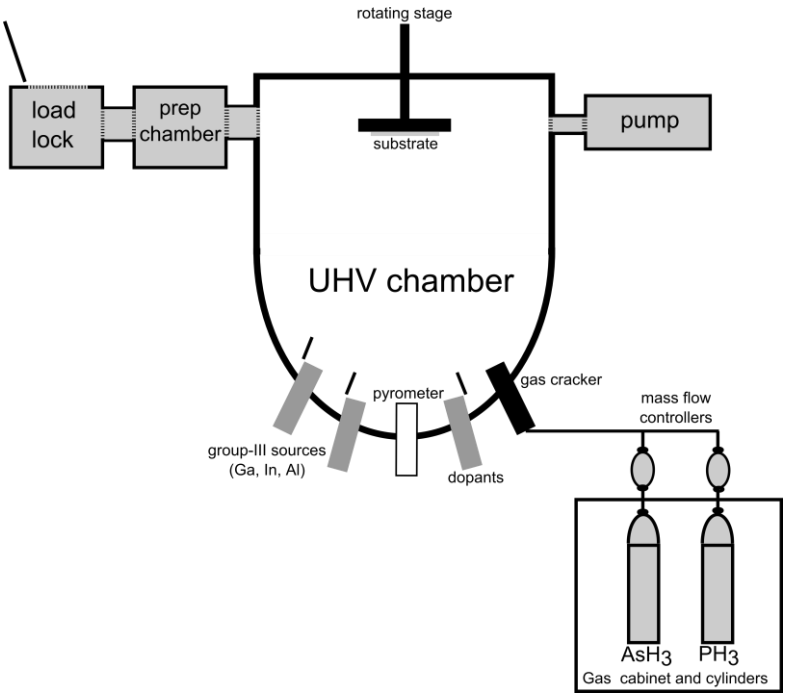

Figure 2.1: Simplified schematic of the GS-MBE system used for NW growth in this thesis.

pyrolytic boron nitride, surrounded by both heating and cooling elements. As the heated source material inside the cell evaporates, the pressure differential between the interior of the cell and the chamber generates the molecular flow outwards into the UHV. The flux is directed towards the substrate through an orifice and the angle between the beam and the substrate surface normal is 33° in the particular MBE system used here. A high-speed shutter is used to control the deposition time, while impingement rate is determined by the temperature of the source cell. Dopants (Si, Be and Te) are also supplied in this manner using effusion cells. The group V species, however, are instead cracked from gaseous hydrides (PH_3 and AsH_3). This occurs in a gas cracker operating at a temperature of 950^{o}C, which favors the formation of the dimer species (P_2 and As_2).

The gas-source method can be advantageous, since fast-acting mass flow controllers are used to regulate the group V flux. Replacement of the gas cylinders is also simpler since it does not require the venting of the UHV chamber.

Control of substrate temperature is accomplished via a combination of a thermocouple attached at the backside of the stage and a pyrometer. In the case of thin film growth, the pyrometer provides a higher accuracy, non-contact temperature measurement throughout growth. However, the light trapping effect of NWs on the surface decreases the effectiveness of the pyrometer method once the growth is initiated. Therefore the thermocouple is also used to provide ongoing growth temperature monitoring and control, and is calibrated using standardized growth of GaAs (100) thin film samples. In order to maintain UHV conditions a series of vacuum pumps are used, including liquid N_2 cryopanels which are used to trap any elemental species that subsequently desorb from the substrate surface.

A similar MBE technique which is often used for NW growth is solid-source MBE (SS-MBE), which uses all solid effusion cell sources, including for group V species. Effusion cells must be replenished over time, which can be a hazardous process when dealing with solid arsenic and phosphorus sources. The high vapour pressure of the group V materials requires the use of large effusion cells, since they are depleted rapidly. Larger cells are more difficult to heat and cool, making it relatively challenging to adjust the deposition rate. Solid group V sources also typically produce the tetramer species (As_4 and P_4). These species have significantly lower sticking coefficients compared to adatoms of the dimer species (As_2 and P_2). This means that higher V/III flux

ratios are often required during growth. With higher group V fluxes typically being used, these systems must also have higher pumping capacities for purging of the chamber. It is important to note this distinction as the particular molecular group V species which is used (dimer or tetramer) can also considerably affect the growth results. In Au-assisted growth of GaAs NWs for example, use of As_4 species is associated with higher axial growth rates, longer Ga sidewall diffusion lengths and significantly reduced sidewall growth compared to the As_2 species, yielding rod-shaped rather than tapered final NW morphologies [77].

There are many other related vapor phase epitaxy (VPE) techniques which are also often used to grow III-V NWs. The most commonly used are metal-organic MBE (MOMBE), chemical vapor deposition (CVD) and metal-organic CVD (MOCVD or MOVPE), where the growth species are instead supplied directly as precursor gases. Typical group III sources include trimethylindium (TMI), trimethylgallium (TMG), and trimethylaluminum (TMA), while trimethylphosphine (TMP), teriarybutylarsine (TBA), and trimethylarsine (TMA) are commonly used for group V. These precursors undergo dissociation via often complex chemical reactions, either at the heated substrate surface or with the aid of an applied plasma. This produces gaseous by-products which must then be purged from the chamber. During NW growth by these methods, precursors are often found to crack preferentially on the liquid seed particle surface (typically Au) under certain growth conditions [35,78]. The chemical action of the liquid droplet in this case is why this growth mode is commonly referred to as “Au-catalyzed”. It is important to note that this is not the case during MBE NW growth using pre-cracked species,

although the term catalyst is often incorrectly used throughout the literature. Since there are a great many differences between these techniques when compared to conventional MBE, especially in terms of adatom and growth kinetics, it is important to be attentive to the specific growth technique used when comparing growth results and deposition conditions from various reports of III-V NW growth.

2.2 Electron Microscopy

Electron microscopy encompasses a number of techniques which exploit the properties of electrons to enable high resolution imaging, as well as compositional and structural analysis. A combination of these techniques was used to characterize the morphology and structure of the NWs studied in this thesis. Scanning electron microscopy (SEM) was used for the characterization of as-grown sample topology and NW morphology, whereas structural and interfacial analysis was performed using transmission electron microscopy (TEM).

2.2.1 Principles of Electron Microscopy

The foundational insight which eventually led to the development of electron microscopy was de Broglie's famous wave-particle duality hypothesis. Since particles can also exhibit the properties of waves, they possess an associated wavelength (λ) which is given by;

$$\lambda = \frac{h}{p} = \frac{h}{mv} \qquad (2.1)$$

where h is Planck's constant and the momentum (p) is the product of the mass (m) and the velocity (v). The mass in this context is the relativistic mass given by;

$$m = \frac{m_o}{\sqrt{1-\frac{v^2}{c^2}}} \qquad (2.2)$$

where m_o is the corresponding rest mass of the particle and c is the speed of light. As a negatively charged elementary particle (of charge e), the electron experiences Coulomb interactions. If free to move as in a vacuum, electrons can gain kinetic energy by applying an external bias. The resulting wavelength of an electron (with rest mass m_e) which has been accelerated by an applied voltage V can therefore be written as [79];

$$\lambda = \frac{h}{\sqrt{2m_e eV\left(1+\frac{eV}{2m_e c^2}\right)}} \qquad (2.3)$$

In an electron microscope, accelerating voltages on the order of several kV to several hundred kV are used to generate a focused beam of electrons with wavelengths much shorter than that of the visible light used in conventional optical microscopes. By imaging using electrons instead of light, electron microscopes are able to access much higher spatial resolutions compared to conventional optical microscopes. This can be understood by analogy to classical ray optics, where the Rayleigh criterion describes the smallest resolvable separation $(\Delta l)_{\min}$ between two distinct points, given by [80];

$$(\Delta l)_{\min} = \frac{0.61\lambda}{n\sin\beta} \qquad (2.4)$$

where n is the index of refraction and β is the semi-angle of collection. The maximum resolution of a typical light microscope is therefore directly limited by the wavelength of visible light to the scale of hundreds of nm, whereas the corresponding theoretical resolution limit of electrons with energies of hundreds of kV would be on the order of picometers. Despite the fact that this ideal resolution limit cannot be achieved in practice due to technological limitations such as aberrations and astigmatisms in manufactured electromagnetic lenses, imaging of nanostructures and even atomic positions is made possible by use of these techniques.

There are a few mechanical components shared by most electron microscope systems. First, an electron gun provides a source of electrons through thermionic, Schottky, or field emission. The electrons then travel through an evacuated column and sample chamber which is maintained using a progression of vacuum pumps and gauges. A series of apertures and electro-magnetic lenses are used for focusing, magnifying and directing the electron beam through its trajectory onto the sample. Finally, specially designed detectors are positioned within the chamber to acquire the desired signals generated by the interaction of the primary electron beam with the specimen.

Scattering occurs as the primary electrons pass into the sample due to the Coulomb forces they experience while passing close to the nuclei or bound electrons making up the material. The probability that an electron will undergo any particular inelastic or elastic scattering event is dictated by the interaction cross-section, which has a strong angular dependence. In general forward scattering is more probable while backward scattering is far less likely to occur. The distribution of possible scattering

angles and energies determine the resulting electron trajectories which bound an average interaction volume within the sample. The exact shape and size of this interaction volume generally depends on the probe diameter (largely dictated by the beam current), incident energies of the electrons in the primary beam, and the sample material itself. Higher energy electrons experience lower scattering cross-sections and therefore penetrate more deeply, while materials with higher density, thickness or atomic number scatter more strongly. Many collateral signals are produced by the interaction of the primary electron beam with the sample under typical SEM and TEM imaging conditions are illustrated in Figure 2.2 (a) and (b), respectively, and include backscattered and secondary electrons, cathodoluminescence, x-rays and Auger electrons.

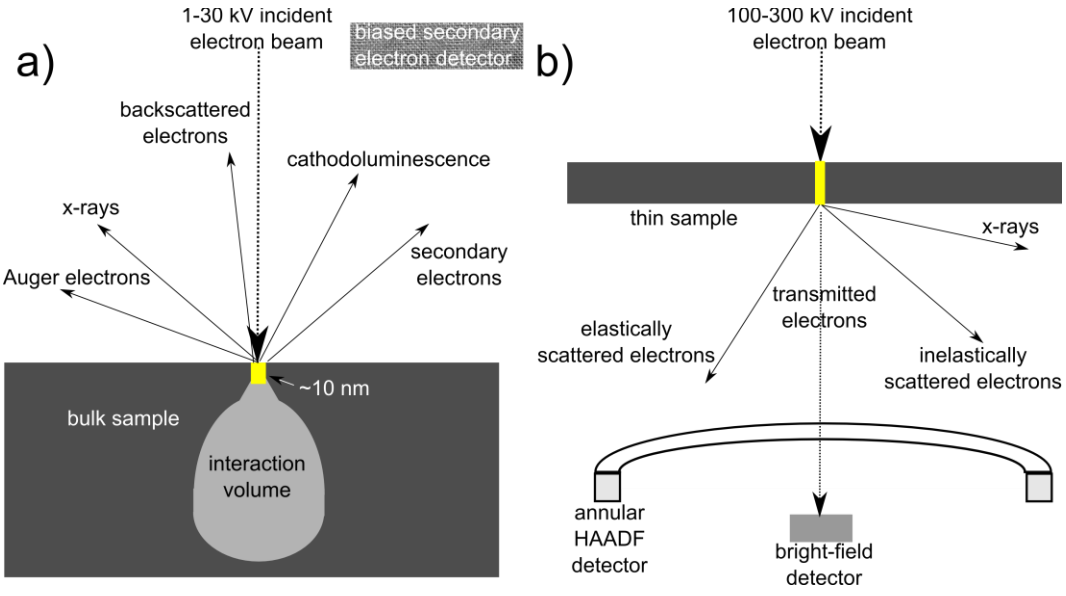

Figure 2.2: (a) Interaction volume of primary electrons with specimen atoms below the sample surface. Secondary, backscattered and Auger electrons, cathodoluminescence and X-rays are produced and may escape the surface under typical SEM imaging conditions. (b) Under typical TEM imaging conditions, electrons may be transmitted directly through a thin sample or undergo elastic or inelastic scattering.

2.2.2 Scanning Electron Microscopy

Secondary electrons may be produced when loosely bound valence electrons within the sample material undergo inelastic collisions with the electrons from the primary beam. Backward scattering angles for these secondary electrons are obtained with a lower energy distribution of several tens of electron-volts, so that they can only escape the sample surface from a depth of around 10 nm. Therefore, the relative intensity of the collected secondary electron signal as the primary beam is scanned over the sample surface yields predominantly topographical information. In general, a decrease of the signal is registered in depressions and increase is seen for raised features. Use of moderate accelerating voltages (~1-30 kV) helps to promote the generation and extraction of secondary electrons.

As-grown samples were mounted to aluminum stubs for SEM imaging in order to determine the overall obtained MBE growth outcomes, as well as to measure the length, radii and yield of vertically aligned NWs in the array. SEM imaging was also used to estimate the diameter of holes on patterned oxide templates. For plan view imaging or for moderate tilts (up to 45°), a flat stub with screw-tightened copper clamps was used. It was not necessary to apply any additional conductive paste or tape, since the clamps provided sufficient electrical contact to ground the sample. Since the SEM does not permit a full 90° tilt of the stage, 45° SEM stubs were used to increase the range of imaging angles so that full 90° side views of the NWs could be obtained. Double-sided carbon tape was used to affix the sample to the stub in this case, and the edge of the substrate was positioned to hang over the lip on the top facet of the stub.

A JEOL JSM-7000F field emission scanning electron microscope (SEM) was used throughout this work. For best imaging results, typical accelerating voltages of 5 or 10 kV were used in conjunction with moderate to low spot sizes between 4-6 (related to the beam current, ~100 pA) and working distances between 6-8 mm.

2.2.3 Transmission Electron Microscopy

As opposed to SEM, where the topology of a bulk specimen is imaged using the secondary electrons ejected from a volume close to the sample surface, in a TEM a combination of high accelerating voltages (typically greater than 100 kV) and specimen thicknesses of less than 200 nm are used to transmit electrons out through the other side of the sample. Although in general much higher resolutions may be achieved in a TEM, different detectors and contrast mechanisms may be used to produce the images, each yielding different types of information about the sample.

A detector positioned directly beneath the sample on the primary beam axis is used in conventional bright-field (BF) TEM imaging, where brightness contrast is produced by weakening in the transmitted beam through a combination of differences in specimen density, thickness, or elemental composition, as well as its crystalline structure. However, if only diffracted electrons are collected, then a dark field (DF) image can be produced. In this case, the directly transmitted beam is blocked by positioning an objective aperture and selecting only reflections from a particular lattice plane to form the image. Areas with different crystalline orientations (such as twin planes) will appear with higher contrast in DF images.

High resolution TEM (HR-TEM) imaging at even higher magnifications can be used to study the crystalline phase of the material, as well as to determine the density of defects such as dislocations in the lattice. Bragg reflections from the crystalline solid can produce distinct spots (phase contrast) in HR-TEM images which resemble the atomic lattice, although they cannot in general be interpreted as such directly without first taking into account the TEM operating conditions and aberrations [81].

If the back focal plane, instead of the image plane, is projected onto the detector, electron diffraction patterns can be collected. Selected-area diffraction (SAD) patterns are formed using apertures positioned in front of the sample and can be used to gain detailed structural information from a particular region of the sample.

High-angle annular dark-field imaging (HAADF) in the scanning transmission electron microscopy (STEM) mode was also used for some of the images in this work. Since the nuclei of different elements scatter electrons at high angles with different cross-sections, an annular (ring shaped) detector is used to selectively capture those transmitted electrons which have been scattered at high angles. This can yield dark-field images with a much higher contribution from Z-contrast, so that differences in brightness due to atomic composition are produced in the resulting images.

2.2.3.1 TEM Sample Preparation

For TEM analysis of the morphology and crystal structure of individual NWs, it is often sufficient to detach the NWs from the substrate and disperse them onto a holely carbon TEM grid. As the diameter of the NWs are typically less than 100 nm, they are naturally transparent to the electron beam in a TEM without any further thinning by

milling or polishing. This was done by cleaving a small piece of the as-grown sample, which was then sonicated for 1-3 min in a small amount of semiconductor-grade isopropyl alcohol. The NWs break off the substrate and are suspended in the liquid. A micro-pipette was then used to apply several 2 µL drops to the TEM grid. The solvent was then allowed to evaporate in ambient air, leaving a low density of NWs lying on the grid.

In order to better study the interfacial region between the NWs, oxide layer and silicon substrate, TEM imaging of as-grown patterned sample cross-sections was required. For this purpose, a focused ion beam (FIB) milling system was used to prepare samples for TEM analysis using a 200 kV JEOL 2010F system, which was especially useful for the investigations of pattern preparation issues which is described in Chapter 3.

The Zeiss SMT NVision40 SII CrossBeam system used in this work is equipped with full SEM imaging capabilities as well as an ion beam column, which is oriented at 54.5° from the vertical electron beam column. Gallium ions (Ga^+) are emitted in a focused beam (as small as 4nm in diameter [82]), which is directed onto the area to be milled. Since Ga^+ is a heavy ion, inelastic collisions between the accelerated ion beam and the constituent atoms of the sample can transfer sufficient energy to sputter the material. The ability to raster scan the ion beam facilitates highly localized milling, while the tandem SEM-imaging mode in the dual-beam configuration allows fine site-specific control.

The Zeiss SMT NVision40 FIB system is not only capable of ion milling, but can also be used to deposit a variety of materials. This is done by in-situ FIB-induced

deposition, where a precursor gas is introduced close to the sample surface via an inserted nozzle. The Ga^+ beam is then used to dissociate the precursor gases, such that material is only deposited on the area over which the ion beam is scanned. This is an important feature of the system in its primary function as a tool for the preparation of cross-sectional TEM samples. Trimethyl platinum and naphthalene precursors were used to deposit platinum and carbon layers respectively [83].

Figure 2.3 illustrates the basic steps involved in the preparation of a TEM lamella using the FIB technique. The area of interest on the sample is first located in SEM imaging mode. Figure 2.3 (a) shows the selection of an area close to the edge of an EBL patterned field from which a lamella was to be prepared. A layer of carbon is then deposited in order to add structure and protect the area of interest during the rest of the milling process (Figure 2.3 (b)). Then, two trenches are milled into the sample on either side (Figure 2.3 (c)), exposing a slice of material centered about the area of interest. A tungsten probe tip is then brought to the site using a micro-manipulator and welded to the slice with deposited Pt. Milling about the edges of the slice then allows it to come free of the sample (Figure 2.3 (d)). Pt welding is then used to attach the lamella to a TEM grid. The probe is then detached (Figure 2.3 (e)). The final step involves further milling of the lamella from both sides, this time using lower ion beam currents for finer control. This is done in order that the final lamella is thin enough to be transparent to electrons for subsequent TEM analysis (typically with energies greater than 100 kV). Figure 2.3 (f) shows a finished TEM lamella, where a specific row of NWs has been removed from an as-grown sample.

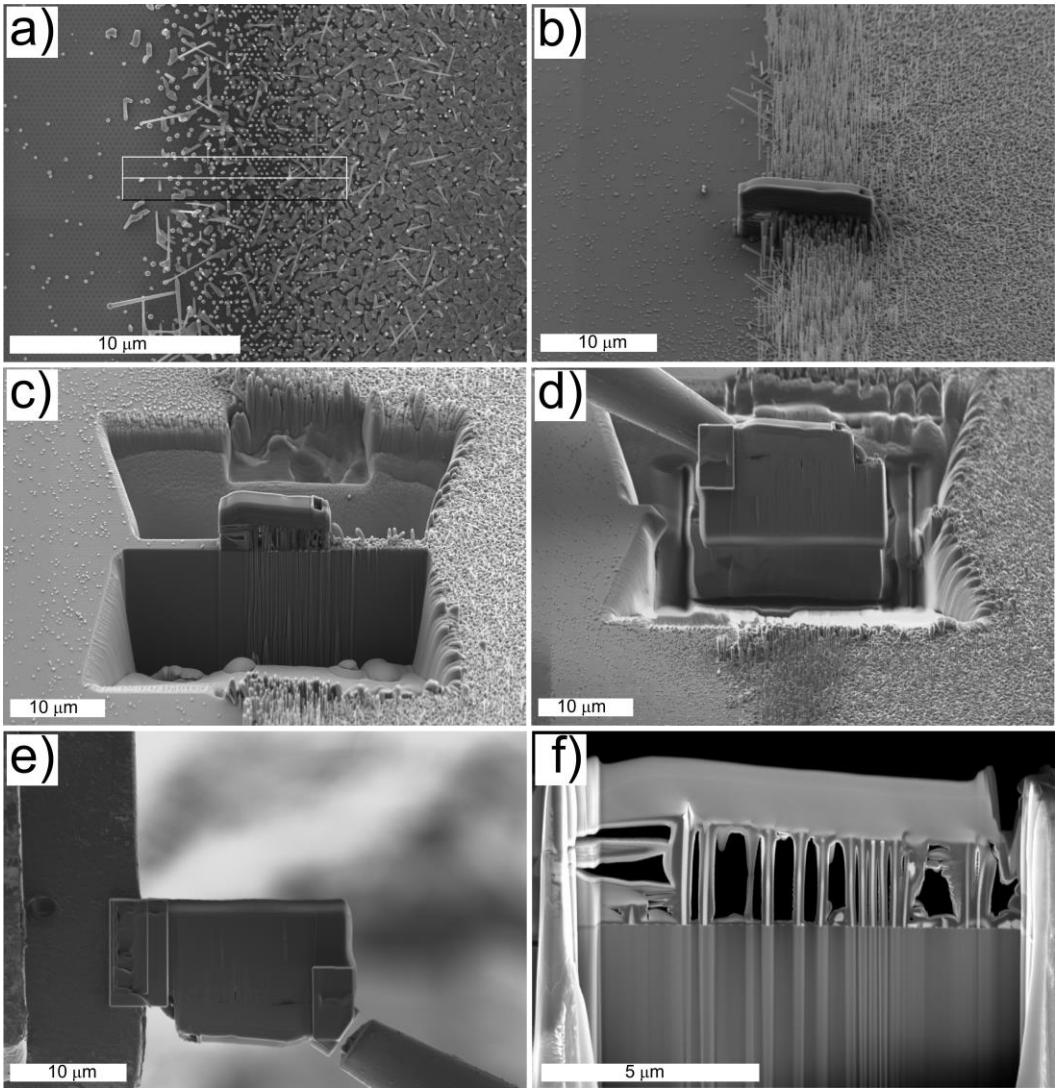

Figure 2.3: Process of lamella preparation using FIB for cross-sectional TEM analysis. (a) Location of the area of interest, indicated by the white box aligned along a row of NWs. (b) Deposition of protective carbon layer. (c) Ion-milling of trenches on either side of the area of interest. (d) Pt-welding to the probe tip and liberation of the lamella. (e) Pt-welding of lamella to the TEM grid and detachment from probe. (f) Lamella after further thinning using fine probe current ion-beam. Nanowires, still attached to the underlying substrate are now exposed.

This FIB preparation method allows free-standing NWs to be removed intact and still attached to the underlying substrate material, allowing the interfacial region to be

studied. However, high-resolution TEM imaging can often be impaired due to the interference of carbon originating from the thick protective coating. A small number of NWs also bend under the carbon layer, although the majority appear unaffected.

2.3 Electron Beam Lithography

Section 1.2.4 described how patterning an array of nano-scale holes in an oxide layer could be used as a template for growing positioned self-assisted NW arrays. Electron-beam lithography (EBL) was used for this purpose in this work. EBL is a high-resolution (>10 nm) form of maskless lithography, where the function of a focused electron beam is to penetrate and modify the properties of a thin resist layer applied overtop a substrate. This method is used to create arbitrary structures in the resist, which can subsequently be transferred into the underlying layers either by deposition, implantation or etching.

EBL as a tool for research and prototyping applications on the nanoscale is advantageous since the details of the pattern may be manipulated entirely in the software environment, allowing both fast design and custom engineering between writes. It is therefore straightforward to adjust the hole diameter and pitch within each field and then to place multiple fields on a single sample. In this way, the use of EBL for this purpose enabled the efficient study of the effect of the pattern parameters on the NW growth in this thesis. However, EBL is a relatively time-consuming direct-write process and therefore is usually considered a prohibitively expensive option for some commercial applications. However, the use of other patterning methods such as

nanoimprint lithography [84,85] have recently been successfully demonstrated and may be better poised to allow the economical scaling of the template NW growth technique to full wafer patterning and high throughput processing in the future.

2.3.1 Principles of EBL

The EBL technique requires equipment for producing and controlling a focused electron beam which is similar in many ways to the SEM apparatus described in section 2.2.2. For example, a small probe diameter is required in order to achieve the highest possible spatial resolution in both cases. While in SEM a focused beam is essential for the formation of clear topographical images, in EBL it determines the minimum line-width which can be written in the resist.

When the beam of high energy electrons penetrates the resist layer, collisions transfer energy into the polymers making up the resist. The resist itself is specially designed such that this causes a chemical change, either weakening the polymer by rupture or scission of the polymer chains, or strengthening it by random cross-linkage. This modification of the polymer structure makes it so that the exposed area becomes selectively soluble (positive type) or insoluble (negative type) when soaked in a solvent called a developer.

As electrons from the primary beam penetrate the resist, they experience a distribution of scattering events, causing a broadening of the interaction area by the same mechanisms described in section 2.2.2. However, the secondary and backscattered electrons are which are produced by small and large angle scattering are

undesirable artifacts in this case, as they can further expose the resist and therefore reduce the minimum attainable linewidth. This is the reason operating voltages in EBL are usually much higher than those used in SEM. Where accelerating voltages between 1-30 kV are used in SEM in order to promote secondary and backscattered electron extraction for imaging, a dedicated EBL system uses a beam voltage of 100 kV to minimize collateral electron production and beam spreading.

One of the crucial actions of an EBL system is the deflection of the primary beam away from the substrate, termed beam blanking. This is essential as a method to limit exposure so the beam can be moved between desired write areas. Once desired writing within an individual field is completed, the stage is translated to move the beam to the next region on the substrate.

There are several important trade-offs to recognize in EBL. While the write completion time decreases with increasing beam current, raising the beam current increases the minimum probe size as the electrons repel one another, reducing the resolution. Also, since even industrial grade EBL systems such as that used in this thesis can only typically provide a maximum beam blanking frequency of ~50 MHz, there is a minimum dwell time on the order of 20 ns. An EBL write can therefore be frequency-limited, which happens when the beam blanking time is the dominant factor dictating the speed of write completion.

As with the analogous term used in photography, the electron exposure of the pattern is given by the total charge received per unit area, typically reported as $\mu C/cm^2$. This is usually referred to as the “dose”, and is determined mainly by the beam current

and the beam dwell time. A minimum dose is required to uniformly expose the area and produce a clear pattern, termed the clearing dose. Since the clearing dose is determined by a combination of experimental factors such as the type and thickness of the resist layer, the accelerating voltage and beam current, it is usually determined through a dose test. This involves writing a series of test patterns while systematically decreasing the dose, until the developed pattern is no longer clearly resolved.

In this thesis, a strategy called single spot exposure [86] was used to form the pattern. This technique produces uniform, nanometer scale periodic holes over large areas in the millimeter range and the write time is much faster when compared to the conventional direct-write technique. The principle of this approach exploits the finite size of the probe interaction volume in order to expose the desired area of the resist in a single electron beam shot. The spot naturally adopts the inherently circular and Gaussian shape of the electron beam, and the exposed spot diameter is increased by increasing the applied dose. In this thesis, typical dose values between 9000-60000 $\mu C/cm^2$ were used in patterning, with beam currents of 25 and 15 nA, although lower beam currents have recently become available for this scheme.

2.3.2 Oxide Template Preparation

A general outline of the process developed to fabricate the oxide templates used for positioned self-assisted NW growth is illustrated in Figure 2.4. A more detailed procedure specifying each individual step is given in Appendix A. The Vistec EBPG 5000+ system installed at the Toronto Nanofabrication Centre at the University of Toronto was used to perform the all the required EBL for this thesis work.

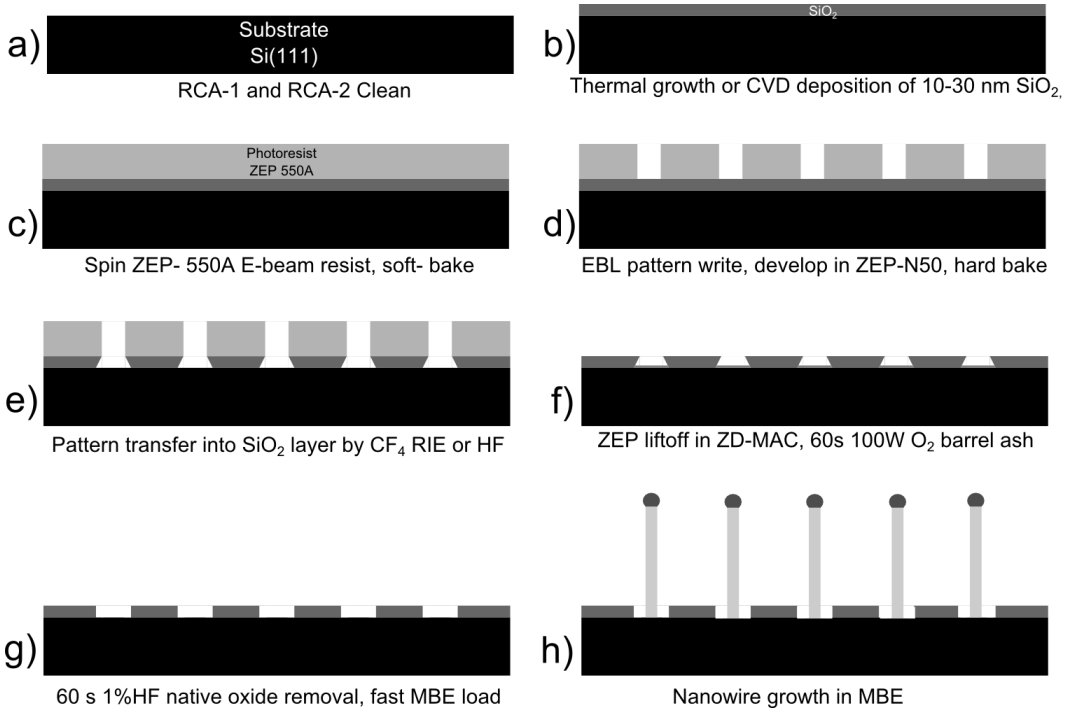

Figure 2.4: Steps in the fabrication of oxide templates for positioned NW growth (a) A Si (111) wafer is RCA cleaned. (b) A thin SiO_2 layer is grown by thermal oxidation or deposited by CVD. (c) A resist layer is spun on the sample and soft-baked. (d) The pattern is written by EBL and immersed in developer solution. Areas of the resist exposed by the electron beam are selectively removed. (e) Wet or dry etching then removes the SiO_2 in spots no longer covered by resist. (f) The resist is lifted-off by ultrasonication in solvents. Organic residues are further removed in an O_2 barrel asher. (g) Just prior to loading in the MBE vacuum, the sample may be dipped in 1% HF for 60s to remove native oxide from the holes. (h) Nanowire growth.

Each new wafer is first cleaned using a sequence of wet chemical mixtures which are designed to remove any organic residues or heavy metals from the surface (Figure 2.4 (a)). After the native oxide layer is removed in buffered HF, a new SiO_2 layer is then grown either by thermal oxidation or by CVD deposition (Figure 2.4 (b)). The oxide should be grown to a specific thickness (±20 Å or less) typically between 10-30 nm, which was measured using variable-angle spectroscopic ellipsometry (VASE). A ZEP-550

A resist layer is then spun on the sample and soft-baked (Figure 2.4 (c)). The sample is mounted on a specially designed stage and leveled such that a height variation of no more than ±10 μm is attained. The stage is then loaded into the EBL system. After the EBL write is complete, the sample is removed and immersed in a developer solution (Figure 2.4 (d)). A positive resist is used so that the areas of the resist which were exposed by the electron beam are selectively removed. Wet or dry etching is then used to remove the oxide from beneath the spots, which is no longer protected by the resist layer (Figure 2.4 (e)). The resist is then lifted-off by ultrasonication in solvents (Figure 2.4 (f)). As an optional step, organic residues may also be further removed using an O_2 barrel asher. Finally, just prior to loading in the MBE vacuum, the sample is dipped in 1% HF for 60s (Figure 2.4 (g)). This step significantly widens the final hole diameter (by ~10 nm), but is required to ensure the removal of any native oxide which subsequently formed in the holes during storage in ambient air. The loaded substrate is then ready for degassing and MBE deposition (Figure 2.4 (g)).

A custom machined sample holder was used throughout this work to load both patterned and unpatterned samples. The photo in Figure 2.5 (a) shows the holder, which is a 2 inch diameter molybdenum disk with 6 sample slots arranged around the circumference. Each slot accepts a 5.45 x 9.45 mm rectangular chip. Since Si (111) wafers naturally form triangular pieces, cleaving at 60° angles, the samples had to be cut into the correct size using a diamond blade wet dicing saw. In order to preserve the surface during this step, a protective photoresist layer was first spun onto the substrate (details given in Appendix A). However, the use of this holder rendered the pyrometer

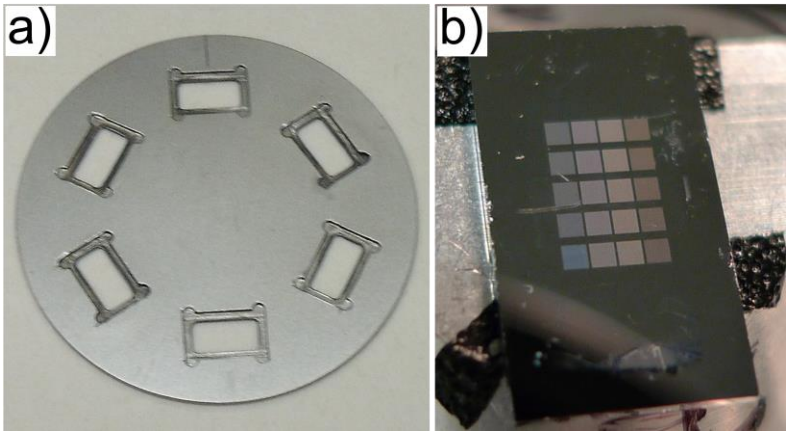

Figure 2.5: (a) The custom machined molybdenum sample holder. The holder allows 6 rectangular samples to be loaded into the substrate tray simultaneously for growth in the MBE system. (b) A photo of an EBL patterned sample post-MBE growth, where the 20 different patterned fields are visible to the eye due to NW and crystallite growth.

method of substrate temperature measurement inaccurate. Thermocouple readings were then used in conjunction with the pyrometer in order to maintain a constant substrate temperature during each growth and from run-to-run.

A hexagonal pattern of holes was chosen in order to maintain a fixed distance between neighboring NWs in the array in all directions. A range of hole diameters were also required. In general, five values of EBL spot dose (9000 $\mu C/cm^2$ at 15 nA and 10000, 25000, 40000 and 60000 $\mu C/cm^2$ at 25 nA) and four values of pattern pitch (250, 500, 1000 and 2000 nm) were exposed in twenty 560 µm x 560 µm (0.31 mm^2) fields. A typical patterned sample is shown (post MBE-growth) in Figure 2.5 (b). The matrix EBL patterned fields, positioned in the center of the sample, are clearly visible to the eye. This is due to the presence of the NW and crystallite growth within the areas patterned with holes. This growth absorbs incident light, with each field appearing different colors due to the combination of hole diameter and interhole spacing.

3 Ga-Assisted Nanowire Growth on Nano-patterned Silicon

An exploration of the effect of both deposition conditions and sample preparation on patterned self-assisted GaAs NW growth will be presented in the following Chapter. Section 3.1 largely contains published work from "Opportunities and pitfalls in patterned self-catalyzed GaAs nanowire growth on silicon" by Sandra J. Gibson, J.P. Boulanger and R.R. LaPierre, published in Semiconductor Science and Technology in 2013 [75]. The various challenges detailed in this work pertain predominantly to the patterning process itself, observed by keeping the MBE growth conditions constant. These "pitfalls" can result in undesired sample outcomes and include the process of pattern transfer by wet/dry etching, oxide layer thickness variations, native oxide re-growth during storage in ambient air and/or incomplete removal of the oxide from the holes.

In particular, it was found that a linearly increasing length-radius distribution, analogous to that observed for unpatterned self-assisted growth on substrates with thin oxides, may be obtained even when using patterned oxide masks due to an unintended residual layer of oxide. The observation of a linear length-radius dependence was explained as resulting due to the individual NWs beginning their growth at different times accompanied by significant radial growth. The spread in obtained NW dimensions was then shown to be significantly decreased by improving the patterning method. Subsequent efforts to measure and model the axial and radial growth rates of the vertically oriented NWs in the array followed these advances.

In Section 3.2, positioned NW growth outcomes using patterned oxide templates obtained while surveying a range of deposition conditions will be summarized. While the sample preparation method was kept consistent, parameters including the Ga pre-deposition time, V/III flux ratio, gallium flux, substrate temperature, and dopants were varied. Preliminary experiments involving Ga droplet consumption and Te-doped shell growth will be presented. Finally, a discussion of the effects of oxide thickness on the hole pattern transfer by RIE and the resulting vertical NW yield will be given.

3.1 Opportunities and Pitfalls in Patterned Self-assisted Nanowire Growth on Si

3.1.1 Introduction

A template of nanoscale holes defined in a thin (100-300 Å) oxide layer is used to facilitate the growth of positioned self-assisted NWs while also avoiding accompanying parasitic film deposition [25–27,87]. Patterning is required to produce the controlled NW morphology, uniformity and areal densities that are necessary for device engineering such as optimal anti-reflection properties or electrical contacting methodologies. Despite the importance of achieving high-quality patterned NW growth, controlling the substrate preparation process is still non-trivial. Therefore, we endeavor here to describe many of the pitfalls of this method which we have encountered, and which can disrupt the growth of position-controlled self-assisted NW arrays in general.

3.1.2 Patterning Details

The substrates used in this study were 300 µm thick n-type (Sb-doped) 3" silicon (111) wafers. A masking layer of oxide with holes in a periodic configuration was prepared on substrates using electron beam lithography (EBL). This template of holes is meant to collect Ga droplets in the early stages of the deposition and enable the nucleation and growth of the NWs positioned in an ordered hexagonal array.

3.1.2.1 Pre-patterning substrate preparation

The wafers were first treated using a standard RCA clean procedure. They were then thermally oxidized in a Jipelec JetFirst 100 rapid thermal annealer (RTA) at fixed lamp power in a dry O_2 environment (~1000 °C). At the end of the desired growth time, the resulting oxidized film thickness was measured by variable angle spectroscopic ellipsometry (VASE) using a J.A. Woollam Co., Inc. M-200UI spectroscopic ellipsometer. The total oxide layer thickness was typically between 100-300 Å for an annealing duration of 200-400 s. It is important to note that the thickness of the oxide layer grown using this method can be non-uniform over the wafer surface, with standard deviations as high as ±35 Å. Layers subsequently grown by CVD for this purpose obtained much higher uniformity over a 3 inch wafer (±5 Å), significantly improving reproducibility.

The wafer was then spun with a protective layer of S1818 photoresist and then diced into 5.45 x 9.45 mm rectangular chips sized for a custom sample holder. After dicing, the chips were cleaned by successive 3 min ultrasonication steps in de-ionized water, acetone and isopropyl alcohol.

3.1.2.2 EBL

The oxidized Si chips were spin-cast with ZEP-550A resist at 6000 rpm for 1 min followed by baking at 180 °C for 90 s. This process yields a nominal resist thickness of approximately 400 nm. A VISTEC EBPG 5000+ E-beam tool operating at 100 kV was used to expose dots in hexagonal arrays in 560 µm x 560 µm (0.31 mm^2) fields. The EBL write was programmed such that the beam would dwell for a specified time at each individual point in the array, which was pre-determined according to the total accumulated dose (µC/cm^2). In this way, increasing hole diameters are obtained with increasing accumulated dose. Using this method, it is relatively straightforward to obtain different values of pattern parameters such as hole diameter and pattern pitch, which allows the study of these effects on the NW growth on a single sample. After exposure, the samples were developed for 60 s in ZEP-N50 and 30 s in 90:10 MIBK:IPA mixture.

3.1.2.3 Pattern transfer and cleaning

The patterns were transferred onto the substrate by etching the oxide layer through the mask of holes developed in the resist. There are many different etching techniques which can be used. Each method should be expected to yield distinct results due to differences in etch rate, anisotropy, selectivity and cleanliness. As an example, we have measured the resulting oxide hole diameter as a function of total EBL dose (µC/cm^2) achieved using four different wet/dry etching methods when etching through a 230 ± 20 Å oxide layer, which are given in Figure 3.1 (a). The apparent hole diameters were measured in plan-view by scanning electron microscopy (SEM), as shown in Figure 3.1 (b). Each etching technique is described in more detail below.

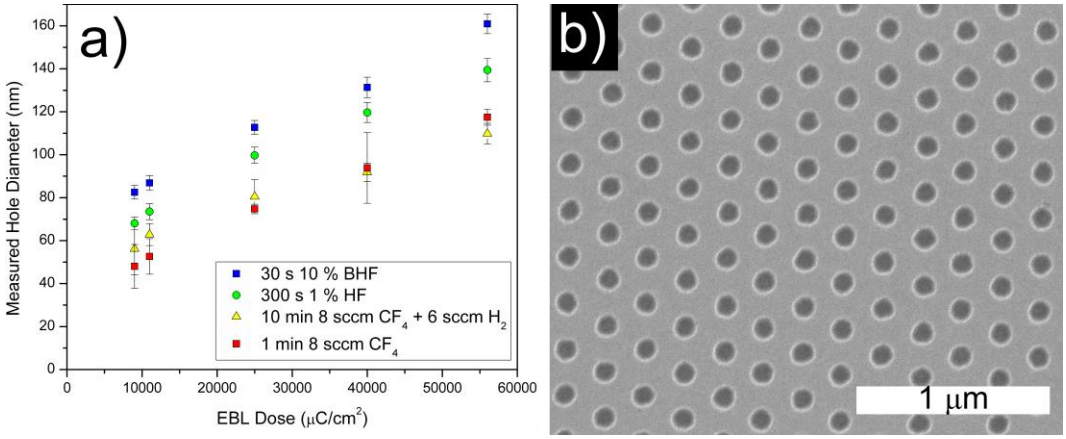

Figure 3.1: (a) Apparent EBL hole diameter vs. total EBL dose (μC/cm^2) for several different wet/dry pattern transfer recipes as measured from plan-view SEM images. (b) Example of a plan-view SEM image of an area patterned using 25,000 μC/cm^2 point EBL dose with 250 nm inter-hole spacing which was transferred into a 250 ± 20 Å oxide layer by etching for 300 s in 1% HF.

Wet-etching techniques gave samples which were generally cleaner, with less organic residues; however, they also etch isotropically and inevitably undercut the resist, resulting in much wider final hole diameters than originally defined by EBL. This can be seen by comparing the final obtained hole diameters in Figure 3.1 (a) for samples etched for 30 s in 10 % buffered HF (BHF) solution and for 300 s in 1% HF diluted with de-ionized water, with those obtained using two other reactive ion etching (RIE) recipes. We note that it can be especially difficult to control the hole diameters obtained using BHF due to the high etch rate (~20 Å/s). We have measured widely different results even using the same procedure and etch times.

Dry etching techniques such as RIE may be optimized to give controlled, highly anisotropic etching conditions. We have used both CF_4 and $CF_4 + H_2$ mixtures, where H_2 is added to increase the anisotropy of the etch in order to achieve minimum hole

diameters [88]. However, a much lower etch rate was observed when compared with pure CF_4, requiring much longer total etch times in order to etch through the same thickness of oxide. We also noted a hardening of the ZEP 550A resist using a mixture of 8 sccm CF_4 and 6 sccm H_2, total chamber pressure of 320 mTorr and a power of 100 W, which made subsequent lift-off and cleaning of the samples more difficult. Overall, a 1-2 min 8 sccm CF4 RIE at 320 mTorr and 100 W gave reasonable results, with a minimum attained hole diameter of ~48 nm using 1 min. etch time.

Lift-off of the ZEP-550A resist was generally performed by soaking in ZEP remover (ZD-MAC) for at least 12 hrs, followed by successive 10 min ultrasonication steps in ZD-MAC, acetone and isopropyl alcohol. The chips were then dried with nitrogen and a final 60 s O_2 barrel ash step at 100 W was performed to remove any remaining organic residues, resulting in a clean, smooth SiO_2 surface. Failure to complete the process with this barrel ash step resulted in samples with unacceptable organic residues often in and around the patterned EBL holes, which could often be seen in SEM images.

3.1.2.4 MBE growth conditions

Since the samples are stored in ambient air, the patterned substrates were etched in a 1% HF solution for 60 s in an attempt to remove the native oxide re-growth within the holes before immediate transfer in ambient air into the MBE vacuum. The total oxide layer thickness is also expected to be reduced in this step, typically by 50-70 Å. The samples were then degassed at 300 °C for 15 min, and the substrate temperature was subsequently ramped to the final growth temperature of 630 °C. Gallium was

introduced for a fixed 30 s pre-deposition time with the intended purpose of aiding the formation of Ga droplets, after which NW growth was initiated by opening the As_2 shutter. The deposition was performed with a V/III flux ratio of 1.8 and 2D equivalent Ga impingement rate of 1 µm/hr for a total growth duration of 15 min. The V/III ratio given is a ratio of actual fluxes, which are based on geometrical calculations and the configuration of the system. The flow of arsine is calibrated as that required to achieve a 2D equivalent growth rate of 1 µm/hr of (100) GaAs for a fixed Ga impingement. The samples were then cooled under ambient As_2 flux.

3.1.3 Results and Discussion

The resulting NW growth was observed using a JEOL JSM-7000F SEM, and JEOL 2010F scanning transmission electron microscope (TEM) operated at 200kV. TEM sample preparation was conducted with a Zeiss NVision 40 cross-beam focused-ion beam (FIB) equipped with a Schottky field emission gun (FEG) SEM. In this section results will be given for several growths performed, using identical MBE conditions, to compare the effect of different substrate treatments on the resulting growth.

3.1.3.1 Insufficient pattern etching

The use of plan-view SEM imaging to measure apparent hole diameters after pattern transfer (by any method) can be a fast and straightforward process; however, the contrast in SEM images cannot be used to ascertain if oxide removal extended fully through to the underlying silicon substrate. Figure 3.2 (a) is an example of a 9,000 $\mu C/cm^2$ dose EBL patterned area with 250 nm inter-hole pitch which was etched for an insufficient amount of time. In this example the pattern was transferred into the oxide

layer using 3 min of 6 sccm CF_4 + 4 sccm H_2 RIE with a total chamber pressure of 320 mTorr and a power of 100 W. Using a FIB milling system, a cross-sectional lamella of the patterned area of the sample was prepared for TEM analysis prior to MBE growth. Figure 3.2 (b) is a bright-field TEM (BFTEM) image showing the oxide/Si interface. It is apparent from this image that, using this recipe, a significant depth (~130 Å) of the oxide layer was not etched through. The tilted SEM image in Figure 3.2 (c) shows the results obtained post-MBE growth. In this case, no NW growth is obtained. Some Ga droplets and crystallites were found in scattered areas over the whole sample surface.

Similar results were qualitatively obtained, regardless of etching technique, for samples where no 60 s dip in 1% HF was performed just prior to loading the sample into the MBE, leaving a fully established native oxide layer intact. An example of this is given in Figure 3.2 (d). These results indicate that an oxide layer thicker than a certain threshold inhibits NW nucleation and growth, as might be expected. Similar observations in unpatterned self-assisted GaAs [89] and InAs NW growth [22] have been made. It is important to be certain that the thermally grown oxide layer is completely etched through so that a short final etch in 1% HF prior to loading in the MBE is certain to remove any remaining oxide in the bottom of the holes without significantly thinning the total thermal oxide layer thickness in the unpatterned areas. The etch rates must be characterized (including the degree of pattern undercut) for the particular etching recipe employed. In addition, since re-growth of the native oxide layer occurs very quickly, the use of in-situ methods for native oxide removal within the MBE

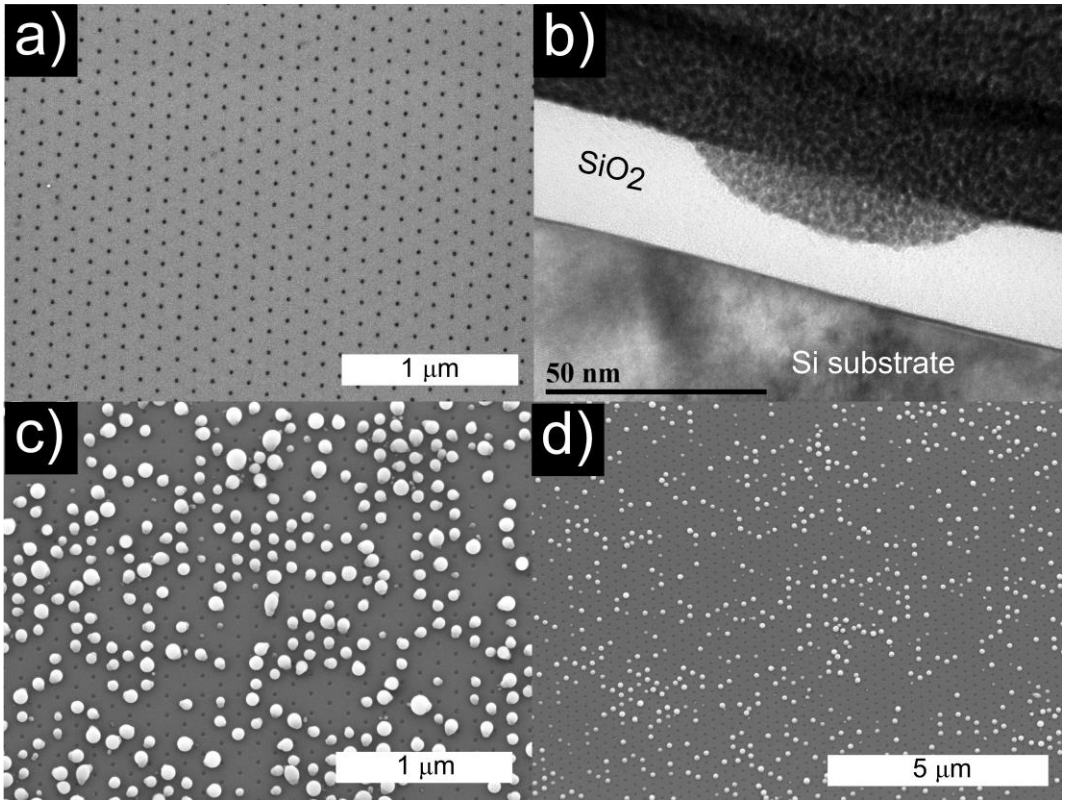

Figure 3.2: (a) Plan-view SEM image of a 9,000 μC/cm^2 dose EBL patterned area with 250 nm inter-hole pitch which was transferred into a 250 ±10 Å oxide layer by 3 min CF_4 + H_2 RIE. (b) Cross-sectional BFTEM image of sample taken from the same area before MBE growth. (c) 25° tilted SEM image showing the area post-MBE growth. (d) 25° tilted SEM image of another sample which was not etched for 60 s in 1% HF just prior to loading in the MBE vacuum.

vacuum will likely be important for improving reliability of this process. For example, methods such as Ga-assisted de-oxidization [90,91] have been used to increase the density of self-catalyzed InAs NWs grown on native oxide covered silicon substrates [22]. In-situ annealing of Si in an ultra-high vacuum environment can be also be used to remove native oxide using substrate temperatures in excess of 850 °C [92], although these would cause instabilities in our MBE system. Hydrogen plasma cleaning

at lower substrate temperatures may also be used under specific conditions to remove native oxides on Si in combination with wet-etching.

3.1.3.2 Qualitative growth comparison

Next we will compare samples for which successful vertical NW growth was achieved but with different sample preparation. Figure 3.3 (a)-(b) show the results obtained for a sample with a 1 µm pitch pattern transferred into a 250 ± 10 Å oxide layer by a 20 s dip in BHF. The NWs grew only from patterned holes, with approximately 60% yield of NWs growing perpendicular to the substrate. No parasitic GaAs film growth occurred on the oxide surface. One of the ultimate goals of the patterning process is to achieve uniform NW length and diameter throughout the patterned array. However, as observed in the boxes in Figure 3.3 (b), both tall and short NWs were found throughout the array. This image clearly shows that tall NWs have larger overall radii than NWs which are shorter. In addition, a number of empty holes are also visible throughout the array. A fraction of NWs originating from the remaining hole locations were either tilted or grew irregularly, often appearing as crystallite growth "crawling" on the oxide surface. This irregular growth is thought to arise due to a 3D twinning phenomenon in the initial seed nucleus [57]. This phenomenon can result in NW growth which is not directly aligned with the crystalline orientation of the underlying substrate and has been shown to be mainly linked with the initial MBE growth conditions [23].

Figure 3.3 (c)-(d) show the results obtained for a sample with a 1 µm pitch pattern transferred into a 230 ± 20 Å thick oxide by a 1 min CF_4 RIE with total chamber pressure of 320 mTorr and a power of 100 W. Similar to the patterned sample in Figure

3.3 (a) any accompanying GaAs film or crystallite growth is completely prevented as a result of the thermal oxide layer masking the surface. In this case, a more modest 20% yield of vertically oriented NWs is obtained. Unlike the sample in Figure 3.3 (a), there are no empty holes visible whatsoever, with all the patterned hole positions occupied by either a vertical, tilted or irregular GaAs NW or is otherwise obscured by crystallite growth. Qualitatively, the vertically aligned NWs in the array appear to have more or less uniform length and radii, which will be discussed further. Although we have not optimized the growth conditions used here (which could affect the NW growth result significantly), a comparison between the two patterned samples presented in Figure 3.3 were all grown under the same growth conditions, and the number of crystallites and vertical NWs differs significantly. This result certainly suggests that the type of pre-patterning has a strong influence on the yield of vertical NWs and the number of crystallite, although a full explanation of this effect is outside the scope of this work.

Finally, Figure 3.3 (e)-(f) shows the results obtained for self-assisted GaAs NW growth on a sample which was not patterned. In this case, none of the processing described in Section 3.1.2 is necessary, since the native oxide layer which naturally forms on the Si surface is purposefully left intact. In this circumstance, Ga-droplets have been shown to collect on the surface and dissolve a pinhole through the thin oxide layer from which NWs nucleate. Using cross-sectional TEM analysis it has been shown that a

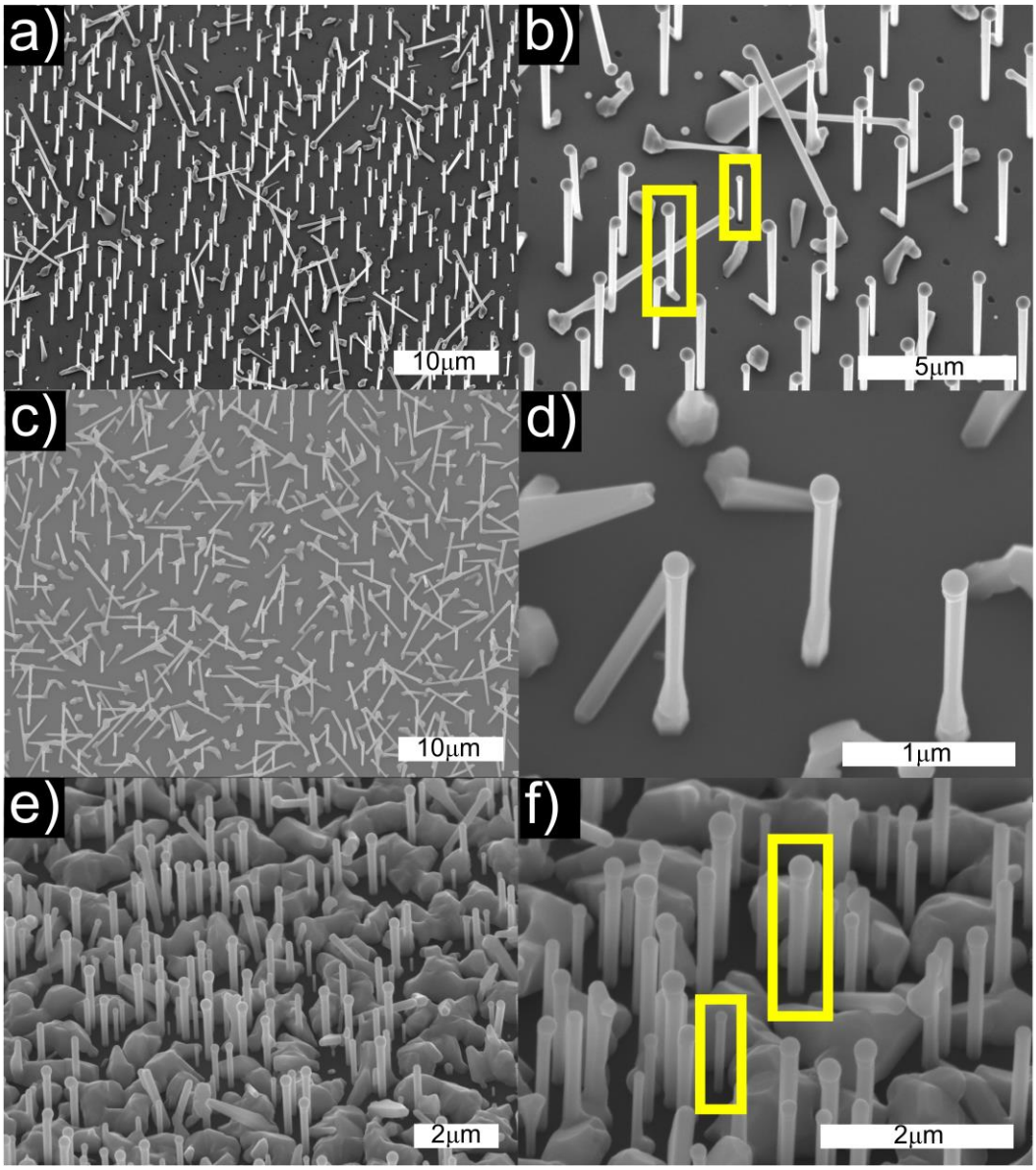

Figure 3.3: 25° tilted SEM images showing typical results for samples grown under the same conditions but with different preparations. (a)-(b) 1μm pitch EBL pattern transferred into a 250 ± 10 Å oxide layer by 20 s dip in BHF, with a large dispersion in NW length and radius as indicated by the boxes. (c)-(d) 1μm pitch EBL pattern transferred into 230 ± 20 Å oxide layer by 1 min CF_4 RIE, with a lower length-radius dispersion. (e)-(f) Unpatterned sample with growth on native oxide.

GaAs seed often diffuses into the substrate and that the epitaxial contact area is much smaller than the final NW diameter [18,23]. There is also some GaAs crystallite growth visible between the NWs. Interestingly, it is evident in Figure 3.3 (f) that this sample exhibits a similar correlation between overall NW length and diameter as is observed for the patterned sample in Figure 3.3 (a)-(b). This will be addressed in the discussion.

3.1.3.3 Cross-sectional TEM analysis

To better understand the differences observed between samples like those compared in the preceding section, cross-sectional samples were prepared using FIB milling in order to perform TEM analysis of the NW/substrate interface. Alignment of the FIB cross-section is crucial for accurate characterization by TEM. Failure to align the cross-section through the center of each hole will lead to the appearance of smaller holes in TEM than observed in SEM. Moreover, the cut must also be parallel to the holes along the 10 µm section. Improper alignment will result in a systematic variation of hole diameters from one end of the cross-section to the other.

For the TEM analysis, a sample was prepared identically to the sample shown in Figure 3.3 (a)-(b). In this case, a 250 nm pitch pattern was transferred into a 250 ± 10 Å thermally grown oxide layer by a 20 s BHF dip. Similar post-growth results were obtained, confirming that the growth results were reproducible and related to the pattern transfer method. The high angle annular dark field (HAADF) image in Figure 3.4 (a) shows the prepared cross-section, with both vertical NWs and unoccupied holes visible. A higher magnification image (Figure 3.4 (b)) shows an individual NW within a ~150 nm diameter patterned hole. A small region of GaAs extending into the substrate

from the center of the NW can be seen. The high-resolution TEM (HRTEM) image of the pinhole area in Figure 3.4 (c) shows that a thin residual oxide layer (~20 Å) remains in the bottom of the hole, with a ~10 nm diameter pinhole extending through this layer. The HAADF and BFTEM images of Figure 3.4 (d)-(e) show a similar thickness of residual oxide within unoccupied holes. It is possible that this oxide layer could have remained after the combined 20 s etch in BHF and 60 s etch in 1% HF just prior to loading. It is also possible that this layer could have formed during the time (~5 min) required to load the sample into the MBE vacuum, or that the oxide layer grew upon removal from the chamber and exposure to ambient air post-MBE. However, the fact that Figure 3.4 (b)-(c) clearly show a small NW/substrate contact area, with the NW/substrate separated only by a thin oxide strongly indicates the presence of the oxide layer during the growth of the NW. We conclude that the presence of this residual oxide layer is linked to the growth results obtained as discussed further below.

A cross-sectional sample was also prepared from a 250 nm pitch patterned area of the sample shown in Figure 3.3 (c)-(d), where the pattern was transferred into a 230 ± 20 Å oxide by a 1 min CF_4 RIE with total chamber pressure of 320 mTorr and a power of 100 W. The HAADF TEM image in Figure 3.5 (a) shows the prepared cross-section, with both vertical NWs and GaAs crystallites occupying the patterned holes. Figure 3.5 (b) shows an individual NW within a patterned hole, where the NW/substrate contact area extends the entire ~48 nm width of the hole. The HRTEM image of the NW/substrate interface in Figure 3.5 (c) shows that no residual oxide layer remains in the bottom of the hole. The HRTEM images of Figure 3.5 (d)-(e) show a hole occupied by a GaAs

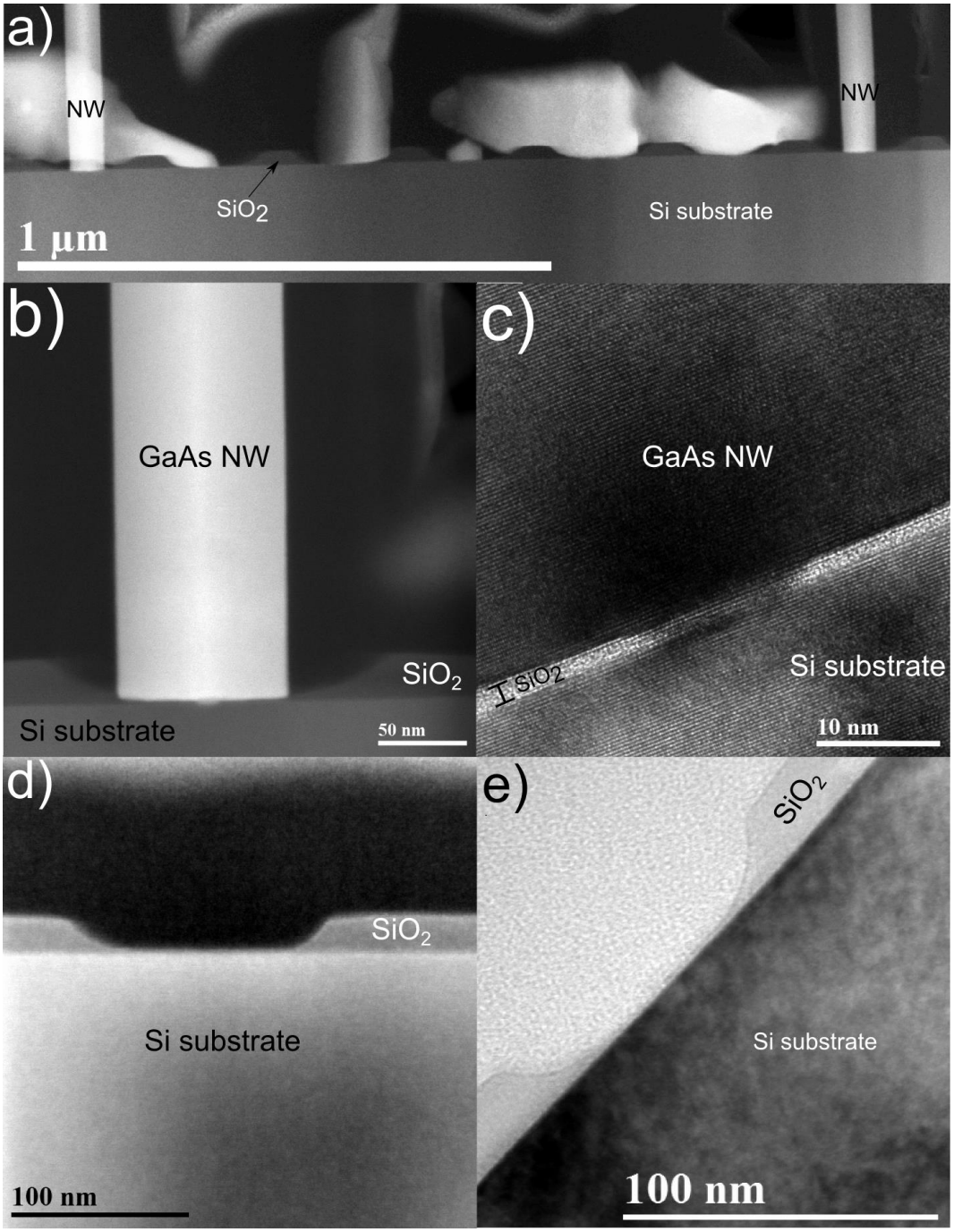

Figure 3.4: Cross-sectional TEM images of NW-substrate interface of a sample with a 250 nm pitch EBL pattern transferred into a 250 ± 10 Å thick oxide layer by a 20 s BHF etch. (a) HAADF image showing the cross-section with two vertical NWs and several empty EBL holes. (b) HAADF image showing NW with a GaAs seed extending into the Si substrate. (c) HRTEM image showing the GaAs seed extending through a residual ~20 Å thick oxide layer at the bottom of the EBL hole. (d) HAADF and (e) BFTEM images of an unoccupied EBL hole showing residual oxide in the bottom of the hole.

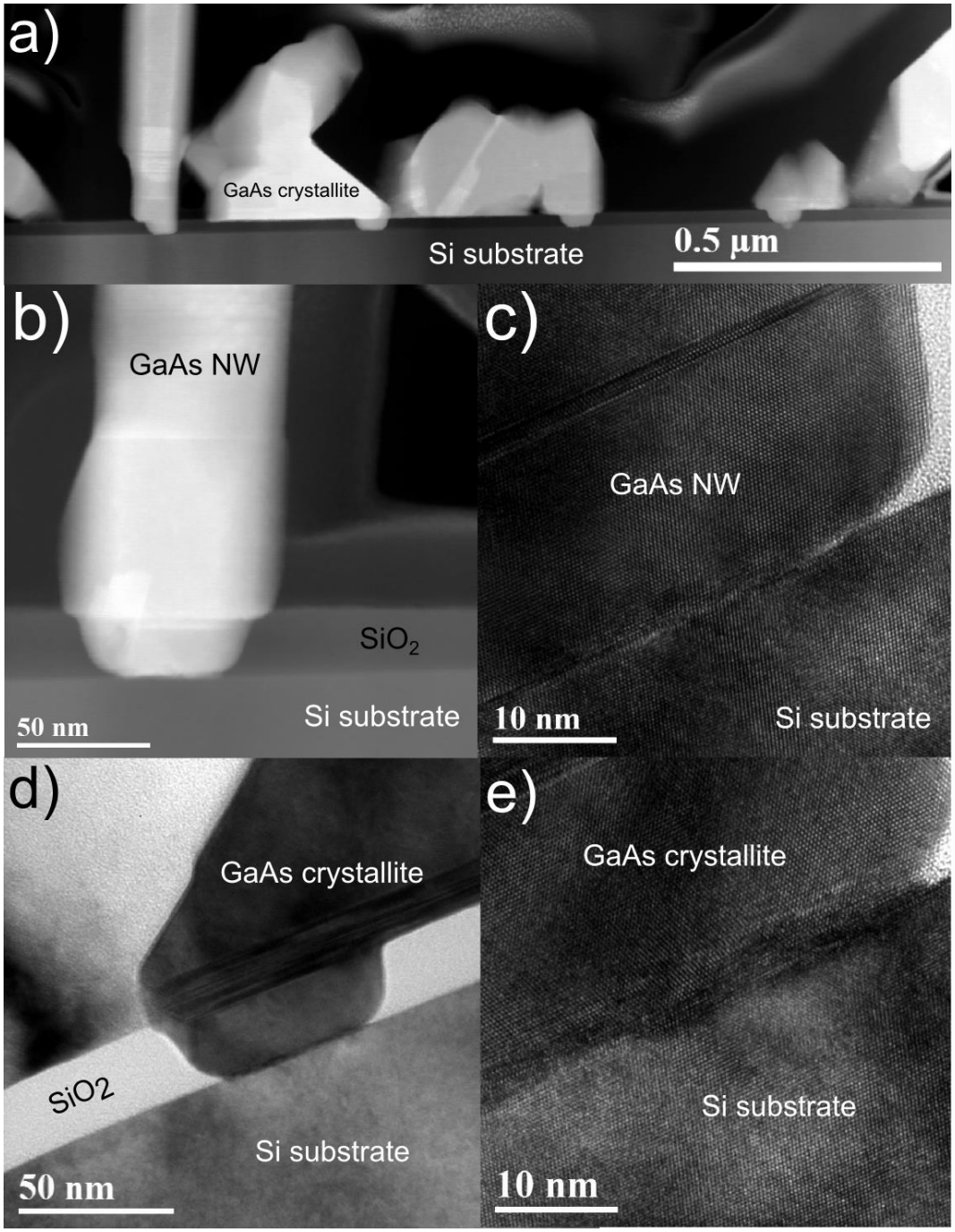

Figure 3.5: Cross-sectional TEM images of NW-substrate interface of the sample with EBL pattern transferred by 1 min CF_4 RIE etch. (a) HAADF image showing a vertical NW and several "crawling" crystallites originating from EBL holes (~48 nm diameter hole). (b) HAADF image showing a vertical NW and EBL hole. (c) HRTEM image showing the NW-Si interface. (d) BFTEM image showing a crystallite in an EBL hole. (e) HRTEM image showing the crystallite-Si interface.

crystallite, which also shows no evidence of residual oxide. Comparing the results in Figure 3.5 with those of Figure 3.4, it may be concluded that the RIE etch is more effective both at producing smaller holes and ensuring the oxide is fully removed from the hole. This conclusion is further supported by the length-radius distributions to be discussed below. The formation of crystallites in some holes, instead of NWs, is believed to be caused by the growth conditions [23,57].

3.1.3.4 Origin of L-R distributions

The length and radius (L-R) distributions of vertically oriented NWs on samples prepared using the three different procedures presented were measured using tilted SEM images and are given in Figure 3.6. Figure 3.6 (a) gives the L-R distribution obtained after 15 min of MBE growth in a 1 µm pitch patterned area with EBL holes transferred into a 250 ± 10 Å oxide layer by 20 s BHF dip, yielding holes with a hole diameter of ~170 nm as measured in plan-view SEM. There is a clear spread in the NW dimensions in this case, with a linear correlation between the NW length and radius. Similar results were also obtained in areas on the same substrate with ~150 and ~130 nm hole diameters. Figure 3.6 (b) gives the measured L-R distributions of MBE growth in a 1 µm pitch patterned area with ~48 nm diameter EBL holes transferred into a 230 ± 20 Å oxide layer using 1 min CF_4 RIE. In this case, three separate MBE growths were performed, with 5, 10 and 15 min total growth duration, respectively. Not only does this show a reduced spread in the obtained NW dimensions, a desired result of the patterning process, but it also indicates that significant simultaneous radial growth of the NWs is obtained using the MBE conditions considered in this study. Similar results were obtained in areas with larger (53, 75, 94 and 117 nm) hole diameters and different inter-hole spacing (250 nm,

500 nm and 2 μm). The unpatterned self-assisted NW growth obtained for 15 min of MBE growth under identical conditions on native oxide covered Si also yielded a linearly increasing L-R correlation, with a generally uniform spread in the obtained NW dimensions. The majority of the NWs in this sample also had shorter lengths (<1 μm) and smaller radii (<50 nm) compared to the patterned growth represented in Figure 3.6 (a).

The axial and radial growth rates have been fully characterized [76] as a function of pattern parameters such as the hole diameter and pattern pitch. A summary of this work is given in further detail in Chapter 4. For the growth conditions employed in this study, the axial VLS growth is accompanied by simultaneous vapor-solid radial growth. Using the average NW lengths and diameters obtained as a function of total growth duration, constant average radial and axial growth rates (GR_{radial} and GR_{axial}) can be measured and these are given in the inset of Figure 3.6 (b). In addition, the initial radius of the Ga droplet (r_o) can be extrapolated from this data [76]. The incubation time refers to the time required to form the droplet of size r_o from which axial VLS growth begins. The value of r_o is constant for a given pattern pitch and growth condition. In our work, the axial and radial growth rates were found to depend on the pattern pitch and degree of surface crystallite coverage (i.e. vertical NW yield) and not the seed/silicon contact area (i.e. the patterned hole diameter) [76].

For growth on native oxide covered substrates, the Ga droplet must first be formed and then subsequently dissolve a hole through the thin oxide layer [18]. As a result, droplets of size r_o and the corresponding GaAs nuclei are not all formed

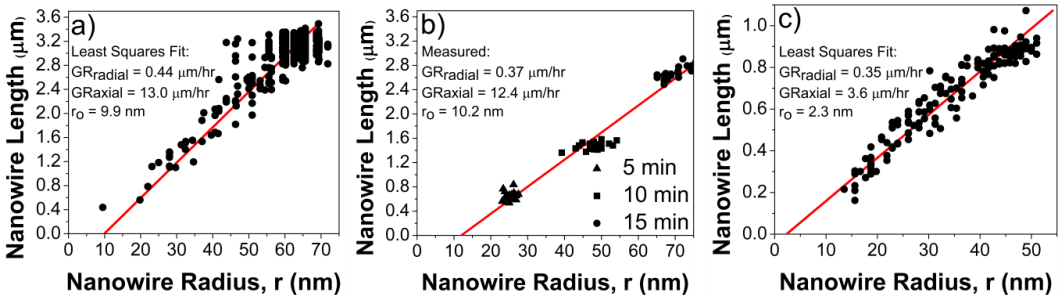

Figure 3.6: Measured length and radius of NWs with linear fitting parameters for (a) a 1μm pitch EBL pattern transferred into a 250 ± 10 Å oxide layer by 20 s dip in BHF for 15 min MBE growth, (b) 1μm pitch EBL pattern transferred into a 230 ± 20 Å oxide layer by 1 min CF_4 RIE for three separate MBE growths for 5, 10 and 15 min total durations and (c) unpatterned growth on native oxide for 15 min growth time. The radial growth rate (GR_{radial}), axial growth rate (GR_{axial}), and initial droplet radius (r_o) are indicated in each case.

simultaneously at the beginning of growth but may form at different times in the early stages of the deposition (where the delay is known as the incubation time). Therefore, we expect that droplets having longer incubation times which initiated NW growth at latter times should have a shorter NW length, but would also have proportionately smaller NW radius. The same can be expected for growth on patterned samples where a residual oxide layer is present at the bottom of the holes which results in the same incubation mechanism. In contrast, the CF_4 RIE etch procedure used for the sample represented in Figure 3.6 (b) resulted in no residual oxide in the patterned holes, as confirmed by our TEM analysis. Hence, the spread in incubation times was diminished in this case, resulting in much smaller length-radius dispersion.

A least-squares fit was used to estimate the axial and radial growth rates for both the patterned and unpatterned samples using the measured length-radius data given in Figure 3.6 (a) and (c). This was done by assuming that individual NWs initiated

growth at different times (i.e., had different incubation times), and the axial and radial growth rates are constant throughout the growth following the incubation time. Therefore, each NW is in principle allowed to have an individual incubation or growth initiation time. The values of the growth rates, along with the initial droplet radius (r_o) were then allowed to vary simultaneously until the least square error between the measured L-R data set and the linear fit was minimized. The axial and radial growth rates as well as r_o were directly measured for the patterned sample in Figure 3.6 (b). These were used as initial values (12.4 μm/hr, 0.37 μm/hr, and 10.2 nm, respectively) in the least-squares fit algorithm. The axial and radial growth rates obtained for the patterned sample with residual oxide (data in Figure 3.6 (a)) were 13.0 μm/hr and 0.44 μm/hr, respectively, with an initial droplet radius, r_o, of 9.9 nm. These values are similar to those measured for the patterned sample in Figure 3.6 (b) prepared with the same oxide layer thickness and pattern pitch. However, the thin residual oxide found at the bottom of the holes in the sample of Figure 3.6 (a) (see Figure 3.4) seems to have caused the spread in the incubation times, unlike a fixed incubation time for the sample of Figure 3.6 (b) where the holes were clear of oxide (see Figure 3.5).

The axial and radial growth rates obtained for the unpatterned sample was 3.6 μm/hr and 0.35 μm/hr, respectively, with a r_o of 2.3 nm. This implies the axial growth rate was significantly reduced compared to the patterned samples. This could be due to the higher density of the random NW growth in this case and the accompanying crystallite growth between the NWs. It has been proposed that adatoms evaporating off the oxide surface might impinge on the droplet or sidewalls of the NWs, significantly

contributing to the overall growth rate [36,44,66,76]. Reduction of this flux due to the competing crystallite growth on the surface or shadowing effects from close neighboring NWs might explain the difference in axial growth rate despite the fact that identical growth conditions were used. The relative thinness of the surrounding native oxide compared to the thermally grown layer used on patterned samples may also reduce the secondary flux of adatoms originating from the surface [36].

3.1.4 Conclusions

NWs grown in patterns transferred using improved etching techniques, where the oxide layer is completely cleared from the bottom of the hole, are shown to have low dispersion in obtained vertical NW length and radius. NWs grown in patterns with residual oxide present in the bottom of the holes exhibited linear L-R correlation similar to that obtained for growth on native-oxide covered substrates. Similar results were obtained for patterned areas with different values of pitch and hole diameter. The likely origin of this linear L-R correlation is the presence of the residual oxide layer which increases the likelihood that individual NWs begin growth at different times. Since deposition under the conditions studied here also resulted in significant radial growth, delayed initiation of NW growth not only results in NWs with shorter overall length, but also with correspondingly smaller overall radius R. The observation of this linear length-radius dispersion may be used as an indication of residual oxide present in the bottom of the patterned holes after the pattern transfer/native oxide removal steps.

3.2 Exploration of Growth Parameters

3.2.1 Introduction

The question of how the deposition parameters affect vertical NW yield in patterned arrays is as yet a largely unresolved issue. The evidence thus far suggests that only specific combinations of Ga flux, V/III flux ratio, Ga pre-deposition time and growth temperature maximize the obtained vertical NW yield on Si(111) [87], while certain interdependencies between these parameters are likely to exist. Secondly, it appears that steps undertaken prior to growth, such as template fabrication details and parameters such as the oxide thickness, oxide quality, hole size, as well as in-situ substrate pre-annealing steps, also very strongly affect the overall growth results [29,85,93].

Patterned samples were prepared using the same general procedure detailed in Section 3.1.1 for an exploration of the effect of growth conditions. In general, a matrix of 20 different 560 µm x 560 µm (0.31 mm^2) fields were patterned into a 230 ± 20 Å layer of silicon oxide on n-type silicon (111) using EBL. Unless otherwise stated, ECR-CVD grown oxide was used in these experiments since a more uniform oxide thickness could be obtained, and the patterns were normally transferred using 2 min of 320 mTorr CF_4 RIE at 100 W. After liftoff, involving sequential ultrasonication steps in ZD-MAC, actetone and IPA and concluded with a 1 min O_2 barrel ash (see Appendix A), a 60 s dip in 1% HF was performed just prior to loading the substrate in the MBE vacuum to remove subsequent native oxide re-growth from the bottom of the holes. The substrates were then degassed for 15 min. at 300 °C before introduction into the UHV

chamber. A nominal Si doping level of 4 x 10^{18} atoms/cm^{-3} was used in each of these growths (unless otherwise stated).

3.2.2 Ga Pre-deposition Time

In patterned Ga-assisted growth, the amount of pre-deposited Ga has been shown to have a strong effect on the obtained vertical NW yield and final morphology [29,87,93]. This is likely linked to the size and shape of the Ga droplet in the early stages of the growth as it is possible that, under a particular combination of growth conditions, the Ga droplet size and/or shape which promotes the vertical growth direction is unique. Therefore, identically prepared samples were grown for 15 min with a substrate temperature of 630 °C and a nominal thin film growth rate of 1 μm/hr each using different Ga pre-deposition times. The results are summarized in Figure 3.7, where the fields imaged were all patterned with electron beam dose of 9000 μC/cm^2 and beam current of 15 nA, typically resulting in a hole diameter of ~50 nm.

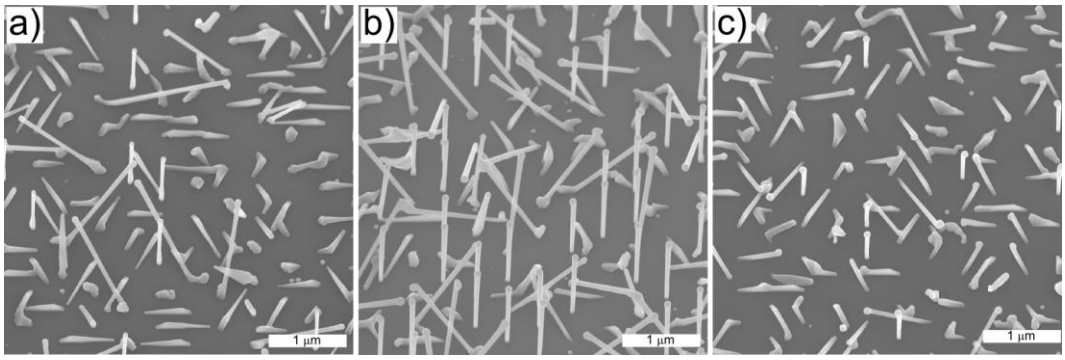

Figure 3.7: Selected SEM images (30° tilt), illustrating the effect of increasing Ga pre-deposition time from (a) 0 s, (b) 30 s and (c) 60 s on the growth results obtained with a Ga impingement rate of 1 μm/hr. The areas imaged here were each patterned with an interhole pitch of 1 μm.

The highest vertical yields (20 ± 4 %) were obtained with a Ga pre-deposition time of 30 s (Figure 3.7 (b)). Assuming a spherical droplet shape [87], 30 s Ga pre-deposition at the given flux (1 μm/hr) is expected to produce droplets that are ~22 nm in diameter in a ~50 nm diameter hole, which is significantly smaller than the ~40 nm diameter optimum droplet size reported previously to give the highest yields (up to 80-95 %) [87,93]. However, other groups have also obtained their highest vertical nanowire yields (between 30 and 65 %) using no Ga pre-deposition step [29,94]. Yields of 10-15 % were obtained for both lower (0 s, Figure 3.7 (a)) and higher pre-deposition times (60s, Figure 3.7 (c)) suggesting that the optimum droplet size may also be correlated with other growth and/or pattern parameters, requiring further investigation.

3.2.3 Gallium Flux and V/III Flux Ratio

The effective V/III flux ratio has been proposed as one of the important factors determining the preferred growth direction of self-assisted NWs. A low local V/III flux ratio is expected to increase the probability of three-dimensional twinning, causing the NWs to grow along (111) directions which are not oriented with the underlying silicon [23,57]. A high local V/III flux ratio has been shown to favor crystallite formation in patterned arrays [25,26]. Therefore, a series of depositions were performed to study the impact of the gallium flux and the V/III flux ratio simultaneously. A growth temperature of 630˚C was used, and the gallium flux is given throughout in units of equivalent two-dimensional growth rates (μm/hr), obtained from calibrated growths of GaAs (100) films. Nominal thin film growth rates of 0.25, 0.5 and 1 μm/hr were used for

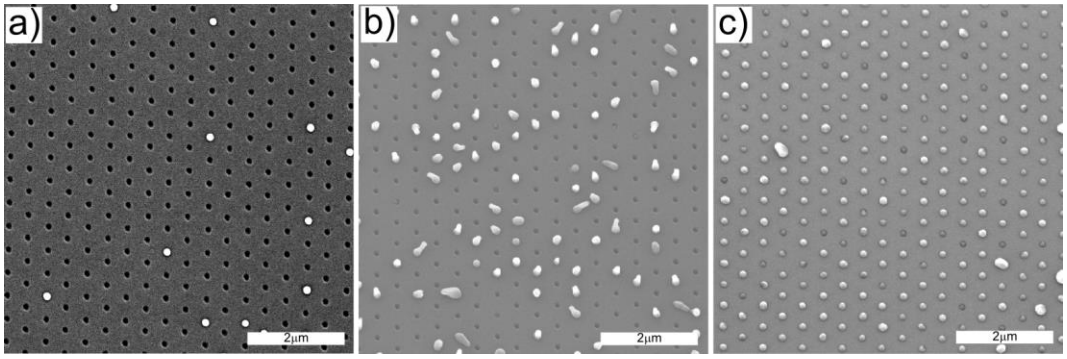

Figure 3.8: Selected SEM images (25° tilt), illustrating the effect of increasing V/III flux ratio from (a) 1.8, (b) 3 and (c) 6 on the growth results obtained with a growth rate of 0.25 μm/hr. The areas imaged here were each patterned with an interhole pitch of 250 nm.

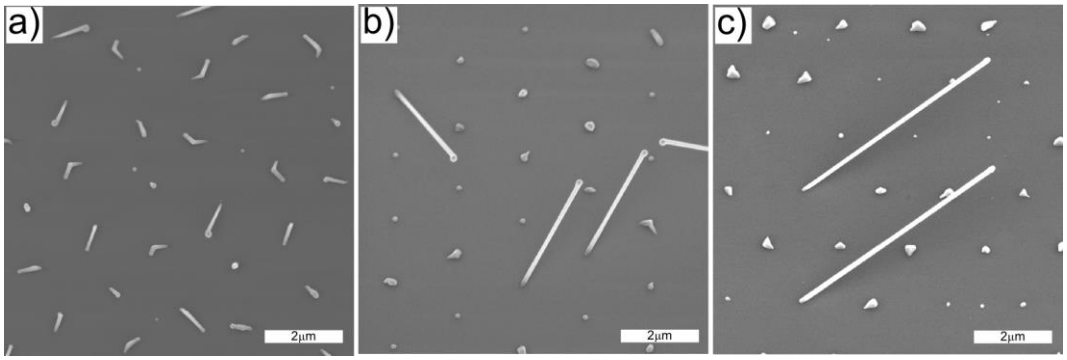

Figure 3.9: Selected SEM images (30° tilt), illustrating the effect of increasing V/III flux ratio from (a) 1.8, (b) 3.6 and (c) 4.4 on the growth results obtained with a growth rate of 0.5 μm/hr. The areas imaged here were each patterned with an interhole pitch of 2 μm.

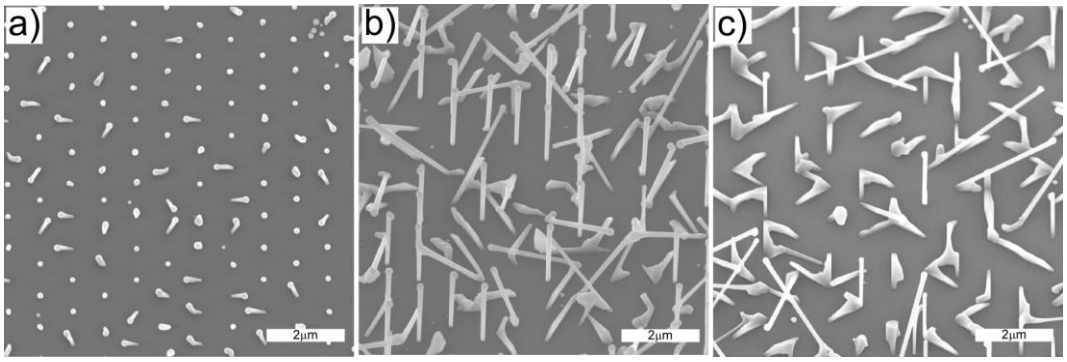

Figure 3.10: Selected SEM images (30° tilt), illustrating the effect of increasing V/III flux ratio from (a) 0.9, (b) 1.8 and (c) 2.2 on the growth results obtained with an growth rate of 1 μm/hr. The areas imaged here were each patterned with an interhole pitch of 2 μm.

this comparison, and the results are summarized in Figure 3.8, Figure 3.9 and Figure 3.10, respectively.

As the gallium flux was increased in this series, the total growth duration (60, 30 and 15 min) and Ga pre-deposition time (120, 60, 30 s) were also adjusted in order to maintain the same total amount of material deposited. This gives a more accurate comparison of the results. In each figure the row of SEM images going from left to right illustrate the effect of increasing the V/III flux ratio. The fields imaged were all patterned with electron beam dose of 9000 $\mu C/cm^2$ and beam current of 15 nA, typically resulting in a hole diameter of ~50 nm.

In the first series of experiments, no vertical or tilted NW growth was obtained for growth with a nominal thin film growth rate of 0.25 μm/hr (see Figure 3.8). A range of V/III flux ratios, 1.8, 3 and 6, were investigated in three separate depositions. For the lowest V/III flux ratio (1.8), sporadic gallium droplets formed on the exposed silicon within the holes, with fewer droplets forming in the smaller holes. Increasing the V/III flux ratio to 3, a combination of Ga droplets and GaAs crystallites are formed within the holes. As the V/III ratio is further increased to 6, all the holes are filled with faceted GaAs crystallites, with sizes linked to the area of the exposed silicon within the patterned hole. In each case the oxide surface is free of parasitic GaAs film growth. There are no gallium droplets collecting on the oxide surface, either inside the EBL patterned fields or in on the areas outside of them.

Similarly, no vertical NW growth was obtained for growths with a nominal thin film growth rate of 0.5 μm/hr. V/III flux ratios of 1.8, 3.6 or 4.4 were attempted (Figure

3.9), with a lower maximum obtainable V/III flux ratio due to the limitations on the As cracker output in our MBE system. For the lowest V/III flux ratio (1.8), tilted and crawling NWs are obtained, with visible gallium droplets found on the tips of the majority. Increasing the V/III flux ratio to 3, a few tilted NWs are also found, but a majority of holes are filled with GaAs crystallites. Further increasing the V/III flux ratio to 4.4, the growth rate of the few tilted NWs increases, as expected from the arsenic-limited nature of Ga-assisted NW growth. The average size of the crystallites also increases. In each case the oxide surface is free of parasitic GaAs growth, with a small number of gallium droplets visible on the oxide surface.

The most successful results were obtained with a nominal thin film growth rate of 1.0 μm/hr (Figure 3.10). For the lowest V/III flux ratio (0.9), a combination of Ga droplets and tilted/crawling NWs are obtained, with visible gallium droplets found on the tips of the majority of the NWs. Increasing the V/III flux ratio to 1.8, a moderate yield of vertically oriented NWs was obtained, with a slightly higher average yield obtained in ~50 nm holes (20 ± 4 %) compared to the ~115 nm holes (18 ± 3 %). Further increasing the V/III flux ratio to 2.2, the vertical NW yield dropped, with the increased spreading of the crawling crystallites growth from the patterned NW positions. Once again the oxide surface does not support the growth of any parasitic GaAs film, and only a small number of gallium droplets have formed on the oxide surface.

In general, growth rates lower than 1 μm/hr did not support the growth of vertical NWs within the EBL patterned oxide template in this series. For a low enough Ga flux (e.g. Figure 3.8), it is possible that desorption of gallium from the exposed Si surface

delays or prevents the formation of gallium droplets during the pre-deposition and/or early deposition phase. It is also likely, however, that reaching the required arsenic concentration in the droplet is prevented or delayed due to the significant desorption flux of arsenic from the liquid gallium phase [95], which is highly temperature dependent. Crystallite growth may then nucleate on the exposed silicon surface and spread over the opening and neighboring oxide provided arsenic flux is high enough.

3.2.4 Substrate Temperature

Lowering the substrate temperature to 550˚C resulted in the formation of a parasitic GaAs film over the entire oxide surface, both inside and outside the EBL patterned fields. This is illustrated in Figure 3.11, where a V/III flux ratio of 1.8, a nominal thin film growth rate of 1 µm/hr and Ga pre-deposition of 17 s were used with a total growth time of 15 min.

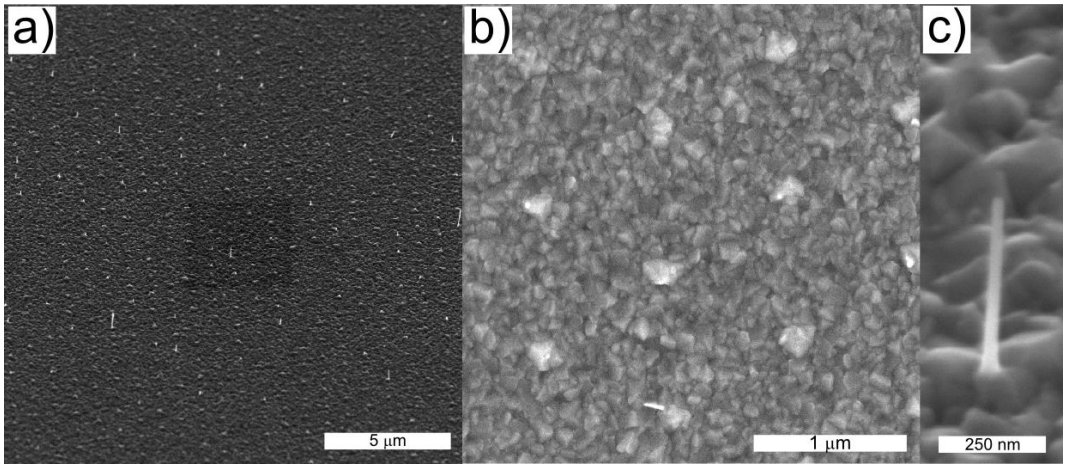

Figure 3.11: (a) 45° tilted SEM image illustrating the effect of lowering the growth temperature to 550°C. The patterned field imaged here was 60000 µC/cm^2 and 1 µm pitch. (b) Plan-view image of the same area, showing the parasitic film covering the entire surface. (c) 45° tilted SEM image showing a single NW in the array.

A raised crystallite formed in most holes, while the few NWs which are visible are highly tapered, with no visible gallium droplets found at the tips. This parasitic film disrupts the growth of the NWs in the array, colliding with the NWs and competing for Ga until the droplet is eventually consumed, halting the NW growth. The so-called selective growth regime, where such undesirable film growth is inhibited, requires the temperature to be high enough for a zero effective sticking coefficient of both Ga and As_2 on the surface [96,97]. As lower temperatures of around 550˚C are typically used during radial NW growth, lower growth rates will be required during these steps to avoid this issue.

3.2.5 Ga droplet Consumption and Shell Growth

As one of the principle motivations for this work is the fabrication of a GaAs-on-Si tandem solar cell, a preliminary attempt was made at growing a Te-doped GaAs shell over a Si-doped NW core in order to form a radial p-n junction.

Consumption of the Ga droplet at the end of growth was expected to halt undesired competing VLS axial growth during shell formation. This process was tested by adding a pause at the end of the growth, shutting off only the Ga flux while maintaining the As_2 flux and substrate temperature. Nominally p-type (Si-doped $4x10^{18}$ cm^{-3}) NW cores were grown at a growth temperature of 630°C, a V/III flux ratio of 1.8, a nominal thin film growth rate of 1 μm/hr and with a Ga pre-deposition of 30s. After 15 min of growth, a pause of 5 min with As_2 overpressure was added before cool-down. The SEM images given in Figure 3.12 (a) show that though the introduction of this step all Ga droplets were completely crystallized at the tops of NWs. This resulted in the formation

of a tapered GaAs tip at the top of each NW, as confirmed by HRTEM imaging (Figure 3.12 (c)).

In the next experiment identical nominally p-type NW cores were grown, with an addition of a step designed to form a nominally n-type shell. Following the 5 min pause, the growth temperature was reduced to 570°C to favor vapor-solid deposition on the NW sidewalls while still avoiding parasitic film growth on the oxide (observed at 550°C, see Figure 3.11). Te dopants ($4x10^{18}$ cm^{-3}) were added, and a reduced growth rate of 0.5 μm/hr and increased V/III flux ratio of 3.6 were chosen in an effort to inhibit the collection of Ga droplets on the surface and encourage uniform shell growth [40]. According to the recommendations of the core-shell depletion model of Chia et al. [98], a growth time of 6 min was chosen in an attempt to form a ~50 nm thick shell layer.

Figure 3.12 (d)-(f) illustrate the outcome of this experiment. Although parasitic film growth was successfully avoided through the use of lower impingement rates during the shell growth step, a low density of Ga droplets did collect on the surface of the mask. The most conspicuous result, however, is the formation of a pronounced spike with a diameter much smaller than the original NW at the tip of the NWs. Measurements of the overall diameter increase in the section below the spike showed that a shell of only ~10 nm was formed over most of the NW core. This can be explained by the subsequent re-formation of a small Ga droplet on top of the NW, which assisted the growth of the spiked section by VLS. This VLS axial growth then competed for growth material (via sidewall diffusion) and reduced the thickness and uniformity of the resulting shell. HRTEM imaging confirmed the presence of a small Ga droplet on the

spike tip (Figure 3.12 (f)). This re-growth effect has recently been reported in the self-assisted growth of unpatterned GaAs NWs [30,31]. This experiment indicates that the use of much lower growth rates and higher V/III flux ratios will be required during shell growth in order to avoid the re-formation of a Ga seed on the NW top.

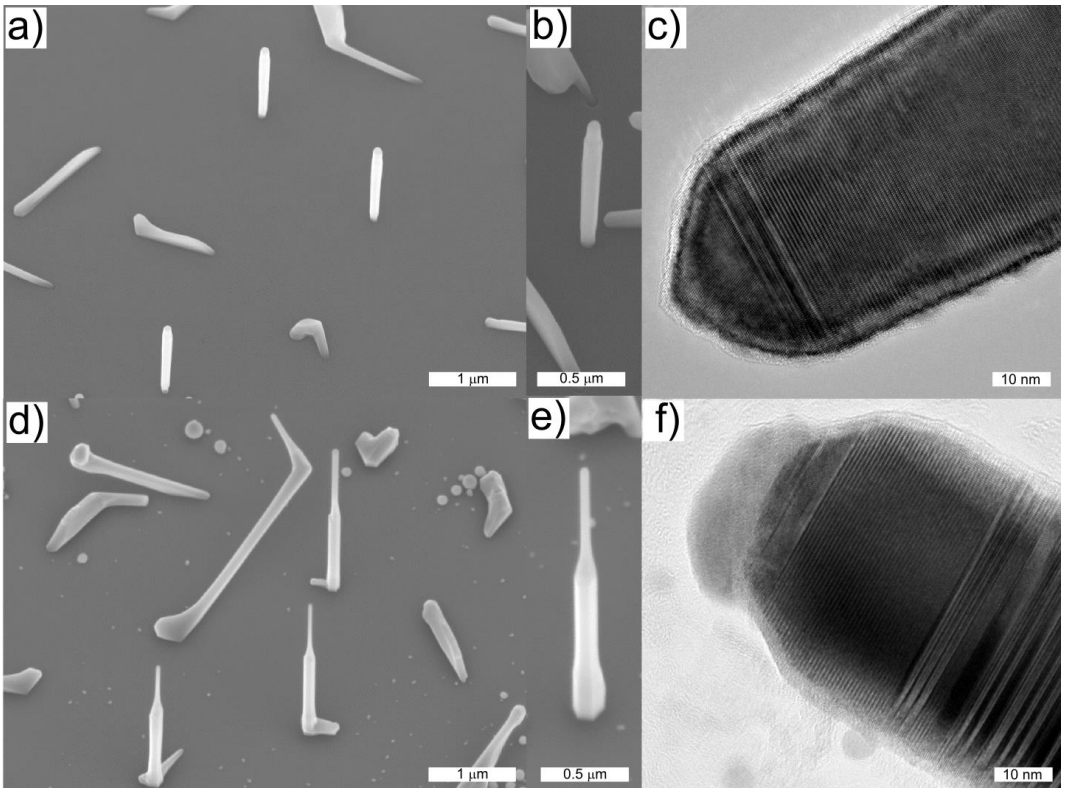

Figure 3.12: (a),(b) 30° tilted SEM images illustrating the consumption of the Ga droplet after a 5 min. pause with As_2 overpressure. (c) HRTEM image showing a fully crystalized NW tip. (d),(e) 30° tilted SEM images illustrating the undesired axial re-growth observed during Te-doped shell growth. (f) HRTEM image confirming the presence of a Ga droplet at the tip of the spiked section.

3.2.6 Be Doping

Although Si is generally an amphoteric dopant in GaAs, it has been used throughout this study as a nominal p-type dopant, as it has been shown to favor

incorporation at As sites under the high growth temperatures used in Ga-assisted MBE growth [100], with successful radial p-i-n structures previously reported [101]. However, self-compensation effects have been shown to deactivate many of the carriers [102], leading to lower than expected conductivity.

In order to investigate the electrical properties of the Si doped (with a nominal doping level of $4x10^{18}$ cm^{-3}) NW cores, samples were sent to Ali Darbandi at Simon Fraser University for study by a technique called nanoprobe [103,104]. This technique uses an electrical probe attached to a micromanipulator installed in an SEM, where the probe tip is brought into contact with the tip of a single freestanding NW, allowing electrical measurements to be done without the use of lithography. NWs with both an intact Ga droplet on the tip and without a Ga droplet were probed (approximately 20 in each sample, as illustrated in Figure 3.13 (a)) and in each case found to have no electrical conductivity. These results suggest a revision of the growth recipe is required.

Recently, Ohmic contacts have been demonstrated in unpatterned Be doped self-assisted GaAs NWs [105]. Therefore, instead of Si, a nominal Be doping level of 4 x 10^{18} atoms/cm^{-3} was tested. This is illustrated in Figure 3.13 where a V/III flux ratio of 1.8, a nominal thin film growth rate of 1 µm/hr and Ga pre-deposition of 30s were used with a total growth time of 20 min.

The most striking effect was that large droplets of Ga accumulated over the entire oxide mask surface, both inside and outside the patterned areas. Be doping has been observed to roughen surfaces and decrease selectivity in SAE [106], therefore the droplets may be able pin to defects introduced on the oxide over the course of the

deposition. While no deleterious effects were observed for growth using Si dopants, high Be doping (greater than 10^{19} cm^{-3}) has been shown to significantly affect the morphology of unpatterned Ga-assisted GaAs NWs [107], causing kinking and pronounced tapering. However, this was not observed and the NWs themselves appear largely unaffected. With further efforts to reduce Ga droplet accumulation such as reduced growth rates and increased temperatures, Be may be used as an appropriate alternative p-type dopant.

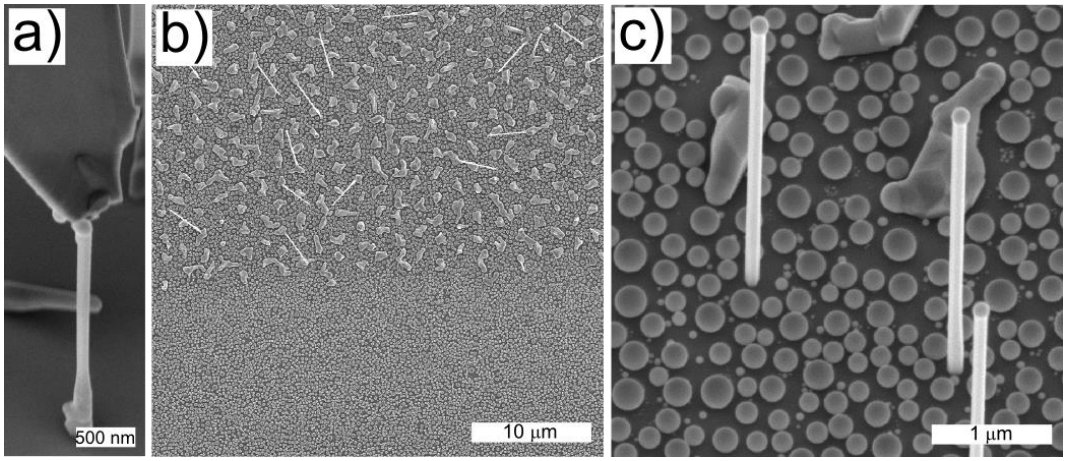

Figure 3.13: (a) 52° tilted SEM image showing a nanoprobe tip being brought to a freestanding nominally Si-doped NW for conductivity measurements. (b), (c) 30° tilted SEM images illustrating the effect of replacing Si with Be doping at a nominal level of 4 x 10^{18} atoms/cm^{-3}.

3.2.7 ARDE-lag and High Vertical NW Yields

Previous reports have noted very different results for identically patterned samples with different oxide thicknesses [29,87], although the cause for this effect was unclear. In addition, the reported optimum oxide thickness varies greatly between

reports (10 nm [87], 18 nm [29], 20 nm [94], 30 nm [85] and 40 nm [93]). Therefore, in several experiments patterned samples with both higher and lower oxide thicknesses than the 230 ± 20 Å typically used were included in the sample set. In these cases the oxide layer was grown thermally as described in Section 3.1.2.1. In the following comparison the samples were all grown at growth temperature of 630°C, a V/III flux ratio of 1.8, a nominal thin film growth rate of 1 μm/hr, nominal Si doping of $4x10^{18}$ cm^{-3} for a total of 15 min with a Ga pre-deposition of 30s. Identical EBL patterns were transferred by 320 mTorr CF_4 RIE at 100 W.

The sample illustrated in Figure 3.14 had a slightly thicker than typical oxide layer (~28.5 nm) and by etching for 60 s a high vertical NW yield (~60 %) was obtained in the EBL field with highest dose (D5, 60000 μC/cm^2), while empty indents in the oxide were found in each of the other EBL fields, suggesting incomplete etching in those areas.

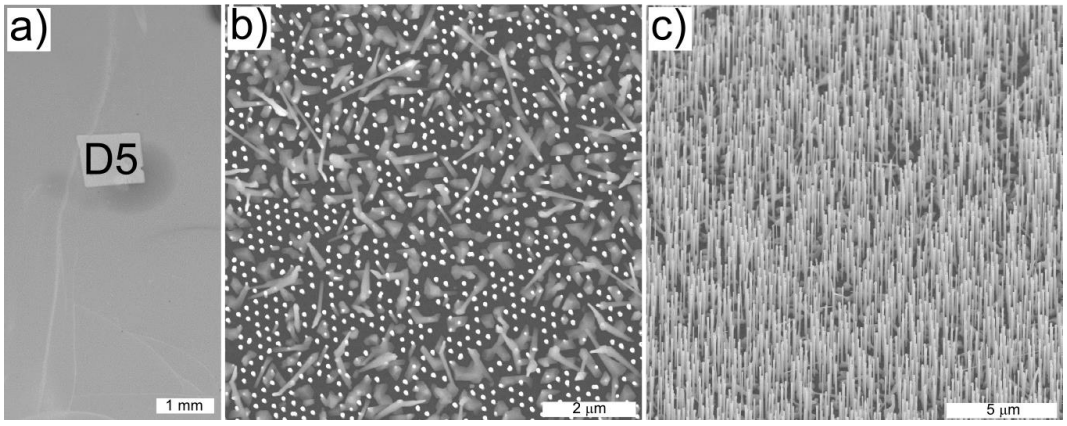

Figure 3.14: (a) Plan-view SEM image showing an under-etched sample overview. This sample had ~28.5 nm oxide, etched by 320 mTorr CF_4 RIE at 100 W for 60 s. The field is labeled (D5, 60000 μC/cm^2) (b) Plan-view and (c) 30° tilted SEM images showing the ~60% yield of uniform vertical NWs in the patterned field.

This high yield effect was not entirely a function of the oxide thickness as suggested in other reports [29,87], however, but rather a combination of the overall etch depth (combined oxide and e-beam resist thickness) and etch time. The sample shown in Figure 3.15 had a much thicker oxide (~32.7 nm) and by etching for only a slightly longer time (70 s) the area with similarly high vertical NW yield (~60 %) was shifted to the EBL field with the next lower dose (D4, 40000 μC/cm^2), while the field patterned with larger holes was overtaken by crawling crystallite growth.

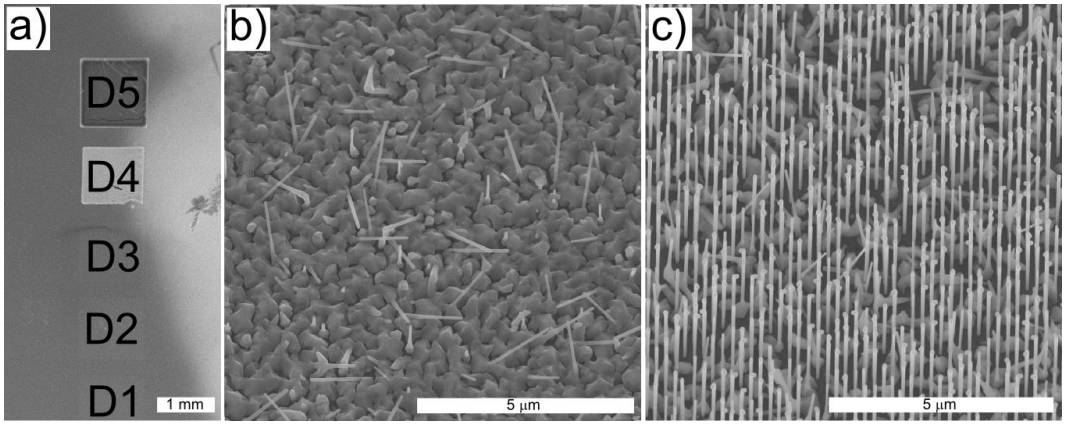

Figure 3.15: (a) Plan-view SEM image showing an under-etched sample overview. This sample had ~32.7 nm oxide, etched by 320 mTorr CF_4 RIE at 100 W for 70 s. The position of the EBL fields are labeled in order of increasing EBL dose (D1-5, 9000-60000 μC/cm^2). (b) 30° tilted SEM images of field D5 and D4, respectively.

This is strong evidence of aspect-ratio dependent etching lag (ARDE-lag), where etching occurs faster in a larger area pattern than a smaller one [108]. Due to the fact that gas conductance into a deep, narrow hole is lower, it is more difficult for reactants to reach the bottom of the hole effectively or reaction products to be removed. In addition, ion bombardment on the bottom can be reduced by sidewall collisions. The

effect of ARDE-lag in reducing the oxide etch rate is also dynamic, generally increasing with etch time as the etched structure evolves. Since the spun thickness of the ZEP e-beam resist is ~400 nm, this will give an aspect ratio greater than 8:1 for a 50 nm hole, high enough for ARDE-lag to be a significant factor in this process.

In order to better understand this issue and the effect on vertical NW yield, another sample with a slightly thinner oxide (~27.7 nm) was etched for 60 s. This sample showed a unique graded effect along the edge of the EBL field, with a clear progression from predominately crawling crystallite growth and low vertical NW yield in the interior, to a section with high vertical NW yields, transitioning finally to empty indentations in the oxide layer going out to the exterior edge. A cross-sectional TEM sample was prepared using the FIB technique in order to study this particular area of the sample.

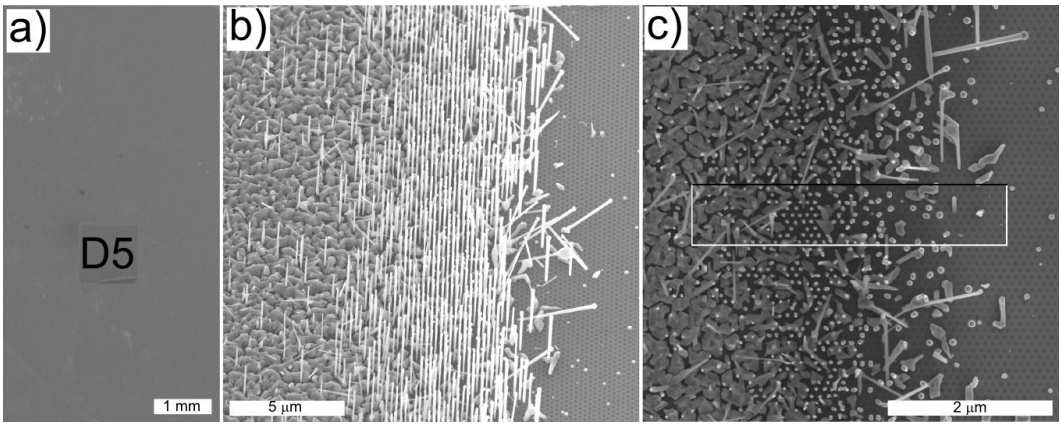

Figure 3.16: (a) Plan-view SEM image showing an under-etched sample overview. This sample had ~27.7 nm oxide, etched by 320 mTorr CF_4 RIE at 100 W for 60 s. The field is labeled (D5, 60000 μC/cm^2) (b) 30° tilted and (c) plan-view SEM images showing a graded area at the edge of the EBL field. Crawling crystallite growth transitioned to an area with high vertical NW yields then to empty indentations in the oxide layer going from left to right in these images. The center of the area indicated by the box in (c) was cross-sectioned for TEM analysis using the FIB technique.

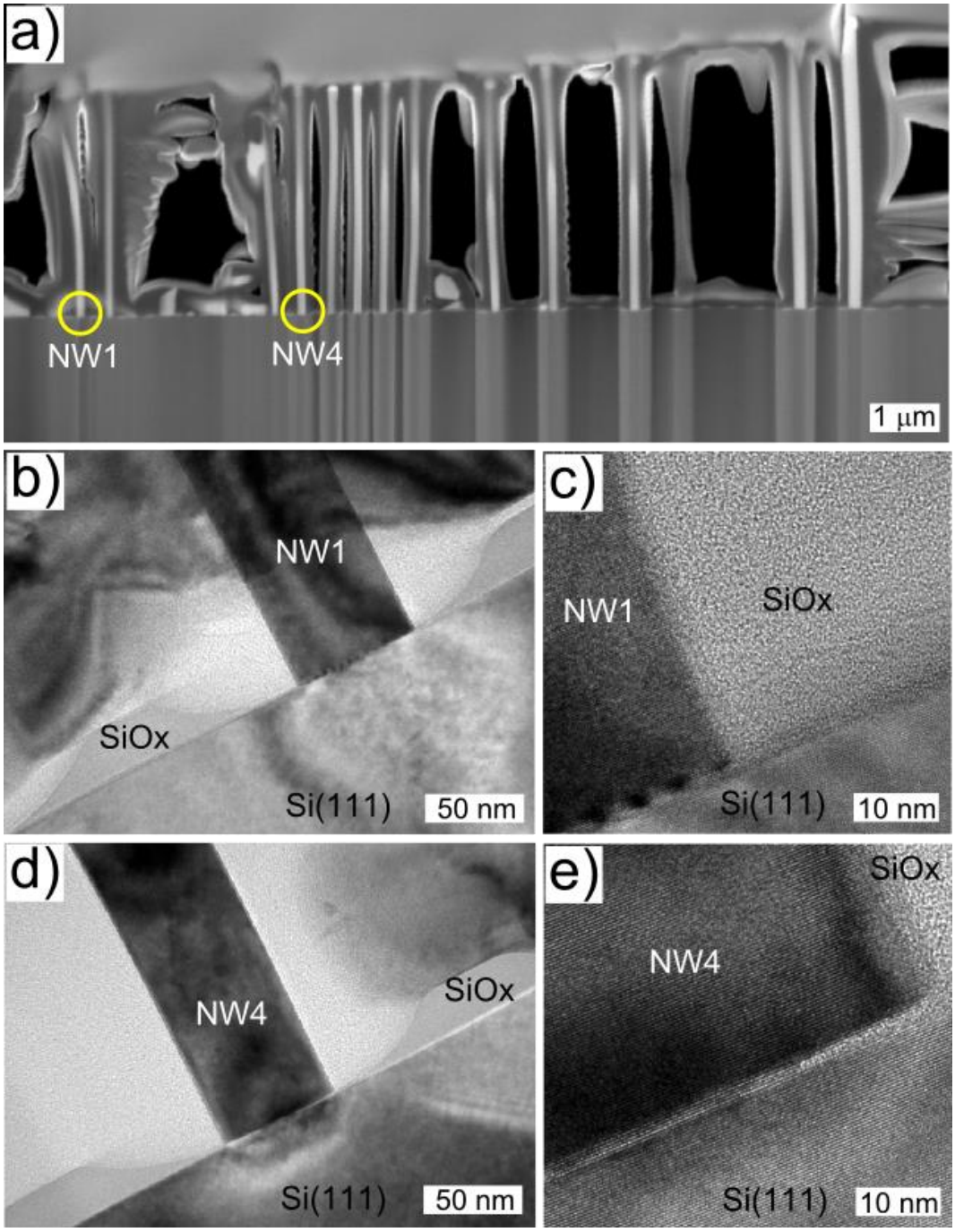

Figure 3.17: (a) 90˚ tilted SEM overview of the FIB cross section. A NW in the interior surrounded by mostly non-vertical crystallites (NW1) and a NW in the high yield section (NW2) are indicated. (b), (c) BF and HRTEM images showing the interfacial region of NW1, which shows full contact with the underlying Si. (d), (e) BF and HRTEM images showing the interfacial region of NW4, which shows a reduced contact area of ~20 nm.

Figure 3.17 (a) shows an SEM overview image of the cross-section prepared by the FIB technique. The interfacial region of each of the 13 NWs in the row were imaged by TEM, and the results showed that while the oxide thickness did not change significantly, the etched depth was slightly decreased going from the interior of the array to the exterior, so that the NW substrate contact area was decreased going from left to right in the image.

It is unclear what caused this effect on this particular sample. One possibility is that there was a local thickness variation in the e-beam resist, causing differences in ARDE-lag. It could also be caused by an RIE effect called reverse microloading. Microloading is caused by a localized depletion of the reactive species or accumulation of reaction by-products as a result of the local pattern density on the wafer, so that features which are close to a pattern edge will etch faster [108]. Under certain etch conditions, however, this situation can be reversed.

A vertical NW from the interior area of the pattern, which is surrounded by mostly non-vertical crawling NW growth (NW1, Figure 3.17 (b), (c)) was found using HRTEM imaging to have contact with the substrate for its entire width (~60 nm). The interface structure is also visibly quite rough. Such interface roughness has been observed for larger diameter unpatterned Ga-assisted GaAs NWs on Si and is associated with residual strain in the NW despite the formation of a high number of dislocation defects [61]. It may be caused by melt-back etching of the substrate due to the reaction of the Si with the initial Ga droplet [109,110], which is possible since Si is soluble in Ga at ~1% at the growth temperature used here [54,55].

However, a vertical NW in the area of high yield (NW4, Figure 3.17 (d), (e)) was found to have a reduced Si/NW contact area of approximately ~20 nm, with an amorphous oxide layer clearly visible beneath the outer edges of the NW. There is also a much smoother interface structure, associated with full strain release at the NW/substrate boundary [61].

Although the cause still remains uncertain, several possibilities could account for the increase in yield observed here in under-etched samples. The reduced area of exposed Si (~20 nm) could be the exact correct size to collect the optimum Ga droplet, producing just the right droplet shape during the 30 s Ga pre-deposition phase to promote the vertical growth direction. Under-etching the layer during the RIE phase and allowing the rest of the original oxide layer to be removed during the 60 s dip in 1% HF just prior to loading could also reduce ion induced damage and polymer contamination of the exposed Si surface at the bottom of the holes. Reactions of the initial Ga droplet with the underlying silicon and interfacial roughness may also be a factor.

If ARDE-lag is significant, using the same RIE recipe will produce the same size hole only if the oxide thickness and e-beam resist thickness is also kept constant. Therefore, this may in part explain the dependence of vertical NW yield on oxide thickness previously reported [29,87], since attention to the actual opening diameters produced using a particular oxide thickness is an additional consideration which may have been largely overlooked.

3.2.8 Conclusions

Efforts to increase the vertical NW yields by adjusting Ga pre-deposition time, nominal thin film growth rate (i.e., Ga flux) and V/III flux ratio have shown that the patterned Ga-assisted growth mode is very sensitive to each of these factors. For the EBL patterned samples investigated here, smaller holes (~50 nm or less), higher Ga flux (1 μm/hr) and 30 s Ga pre-deposition time generally gave the best repeatable yields of vertical NWs in the array (20 ± 4 %). Higher yields (~60 %) were obtained in under-etched samples, revealing a subtle dependence on the actual exposed Si area and suggesting that previously observed differences in vertical NW yield with different oxide thickness could be due to the effects of ARDE-lag. In addition to using more a specialized and flexible RIE system than the one currently available, a thinner e-beam resist layer could be used to help mitigate the effect of ARDE-lag, as this significantly reduces the aspect ratio and would help to increase sample-to-sample repeatability. The use of lower EBL beam currents can also be used to further reduce hole sizes, although removal of the native oxide layer by 60 s dip in 1% HF widens the holes by ~10 nm and introduces a lower achievable limit for such efforts unless an alternative method is used.

Achieving radial NW growth without promoting film growth on the mask is important for producing NW-based devices using this method. This can be done by maintaining a high enough growth temperature to allow a selective growth mode, although there exists several other schemes which allow lower growth temperatures to be used. The simplest is by lowering the impingement rates of both Ga and As_2, which decreases the size and increases the decomposition rates of droplets/crystallites which

initially form on the surface and aid film formation [96,97].Periodic supply epitaxy [111] and hydrogen assisted epitaxy [112] are other possible options for this.

The preliminary study presented here also indicates that avoiding the re-formation of a Ga droplet on the NW top is a further concern during radial growth processes. Undesired re-growth should be mitigated though the use of lower impingement rates and higher V/III flux ratios during the growth of doped shells [30,31].

While Si doping (nominal level $4x10^{18}$ cm^{-3}) did not significantly affect the growth, nanoprobe measurements could not obtain any conduction through the NWs. This indicated that much higher doping levels and/or larger NW core diameters would be required to avoid the effects of surface depletion, although self-compensation effects might be the ultimate limitation for the use of Si as a p-type dopant. Be doping was shown to increase Ga droplet formation on the oxide surface, although no deleterious effects on the NW growth itself were observed at nominal doping level of $4x10^{18}$ cm^{-3}.

4 Study of Radial and Axial Growth Rates

4.1 Introduction

This Chapter largely contains published work from "Study of radial growth in patterned self-assisted GaAs nanowire arrays by gas source molecular beam epitaxy" by Sandra J. Gibson and R.R. LaPierre, published in 2013 [76]. This was the first reported measurement of the growth rates of Ga-assisted GaAs NWs on patterned oxide templates in the literature. Both the axial and radial growth rates were measured and systematically characterized as a function of the pattern parameters, specifically the opening diameter and interhole spacing or pitch. The observed pitch dependence of the axial and radial growth rates lead to the proposal of unique growth kinetics in this system, involving the collection of growth material desorbing from the oxide surface between the NWs. A phenomenological model of patterned self-assisted NW growth was then formulated based in part on the observations presented here.

4.2 Experimental Details

4.2.1 Substrate Preparation

An antimony doped n-type 3" silicon (111) wafer was first treated using a standard RCA clean procedure and then thermally oxidized in a dry O_2 environment (approx. 1000 °C), with a final film thickness of 230 ± 20 Å as measured by spectroscopic ellipsometry. A protective layer of S1818 photoresist was then spin-cast onto the substrate for dicing into 5.45 x 9.45 mm rectangular chips for a custom MBE sample

holder. After dicing, the chips were cleaned by successive 3 min ultrasonication steps in de-ionized water, acetone and isopropyl alcohol.

In order to achieve patterned NW growth, a regular array of nanoscale holes was defined in the thin SiO_2 layer using electron beam lithography (EBL) to facilitate ordered Ga droplet collection and positioning. A VISTEC EBPG 5000+ electron-beam tool operating at 100 keV was used to write hexagonal arrays of holes. A 5X4 matrix of 20 patterns were written in the centre of each chip with five different hole diameters (48, 53, 75, 94 and 117 nm) and four different values of inter-hole spacing or pitch (250, 500, 1000 and 2000 nm). The patterns were then transferred into the oxide layer by a 1 min reactive ion etch in 320 mTorr CF_4 at 100 W. Lift-off of the ZEP-550A resist was followed by a 60 s O_2 barrel ash at 100 W, resulting in a clean, smooth SiO_2 surface. Finally, in order to clear the holes of any native oxide re-growth, the patterned samples were etched in a 1% HF solution for 60 s and then directly transferred in ambient air into the MBE vacuum.

4.2.2 Growth Procedure

The samples were first degassed at 300 °C for 15 min, then the substrate temperature was ramped to the final growth temperature of 630 °C. Gallium was introduced for a fixed 30 s pre-deposition time (to form the Ga droplets), after which NW growth was initiated by opening the As_2 shutter. The deposition was performed with a V/III flux ratio of 1.8 and 2D equivalent Ga impingement rate of 1 µm/hr. Samples were then cooled under As_2 flux. Three separate MBE growths were performed on identically prepared samples, with total growth durations of 5, 10 and 15 min,

respectively. The resulting NW growth was then observed by scanning electron microscopy (SEM) imaging using a JEOL JSM-7000F.

4.3 Results

4.3.1 Length and Diameter Measurements

All samples were free of parasitic GaAs crystallite growth, since the oxide surface between the patterned holes inhibits thin film nucleation. Figure 4.1 (a) shows an example of the results obtained after 15 min of growth for a pattern of 48 nm diameter holes with 500 nm pitch. The NWs grew only from patterned holes, with approximately 20% growing perpendicular to the substrate in the majority of patterns. Many of the NWs originating from the remaining holes were either tilted or irregular, often appearing as “crawling” crystallite growth on top of the oxide surface. This is likely due to 3D twinning of the NW seed nuclei, as reported previously for NWs grown by solid source MBE [23,57]. This phenomenon has been shown to be related to the growth conditions, and was mitigated in solid source MBE by using high V/III flux ratio. A similar optimization is expected to improve the yield in NWs grown here by gas source MBE, although such an optimization is outside the scope of the present study. The growth conditions could be tuned in the future in an attempt to increase vertical NW yield.

The lengths and diameters of the vertically oriented NWs were measured by SEM. An example of the length-diameter data is given for patterns with 48 nm diameter holes in Figure 4.1 (b), showing data collected for all three growths (5, 10 and 15 min)

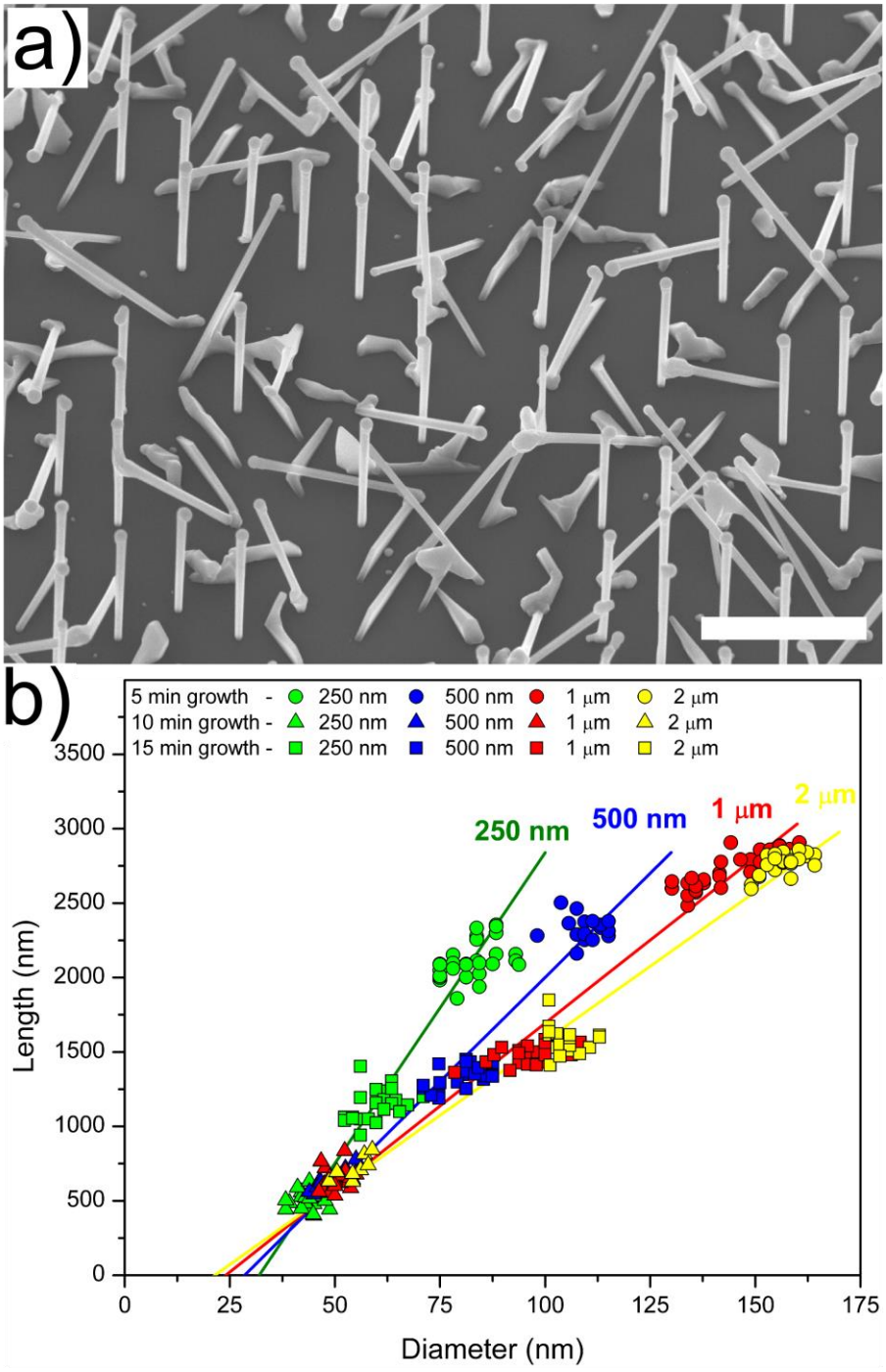

Figure 4.1: (a) 25° tilted SEM image of a sample grown for 15 min with 48 nm diameter holes and 500 nm pitch. Scale bar is 2 μm. The yield of vertically oriented NWs is approximately 20%. (b) Measured NW lengths and diameters for 48 nm diameter holes.

and for each patterned pitch (250, 500, 1000 and 2000 nm). The vertical NWs exhibited only a slight inverse tapering with the diameter at the top of the NW only ~1.5% larger than that at the bottom.

Although there is a certain spread in the patterned NW diameters in Figure 4.1 (b) an overall trend is visible, with lines added to help guide the eye. First, as the pitch of the pattern increased, the average diameter and length of the NWs increased. This trend may be seen qualitatively by comparing the SEM images in Figure 4.2 (a)-(d). Second, as the growth duration increased, the average length and diameter of the NWs in a given pattern increased. This trend may be seen qualitatively by comparing the SEM images in Figure 4.2 (e)-(g). The initial gallium droplet diameter may be inferred as the intercept of the length versus diameter line with the diameter axis, as shown in Figure 4.1 (b), which lies between 20-30 nm for each data set.

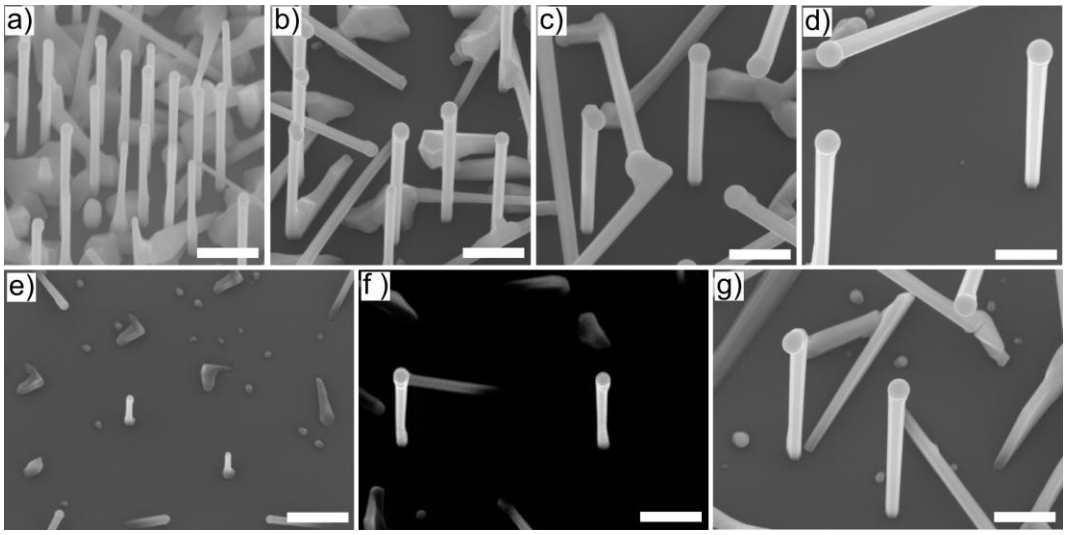

Figure 4.2: SEM images of patterned areas with 48 nm diameter holes and (a) 250, (b) 500, (c) 1000 and (d) 2000 nm pitch after 15 min MBE growth. SEM images after (e) 5, (f) 10 and (g) 15 min growth for a pattern with 48 nm diameter holes and 1 µm pitch. All images are tilted at 25° with 500 nm scale bar.

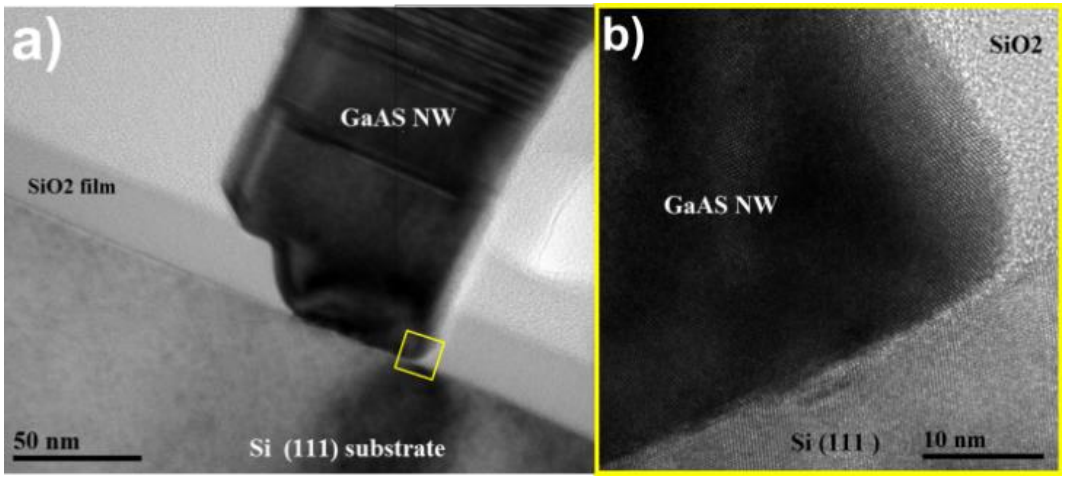

Figure 4.3: (a) Cross-sectional bright-field TEM image of a single vertically oriented patterned NW after 15 min of MBE growth (48 nm diameter holes, 250 nm pitch). (b) High-resolution bright-field TEM image of the NW/Si substrate interface (position indicated in (a)).

The measured diameter of the NWs is also always greater than the diameter of the holes patterned into the oxide layer (48 nm in Figure 4.1 (b)), even after the shortest growth duration (5 min). To directly confirm this using transmission electron microscopy (TEM), cross-sectional samples were prepared using a focused ion beam technique to investigate the NW/silicon interface. A bright field TEM image of an as-grown vertically oriented NW is given in Figure 4.3 (a). The crystal structure of the NWs was zincblende, with multiple twinning planes. After 15 min of MBE growth, the diameter of the NW is roughly twice the original diameter of the hole (48 nm). The NW contact area with the Si substrate is also entirely free of oxide at the interface (Figure 4.3 (b)), confirming that the oxide layer was entirely etched through.

4.3.2 Calculated Growth Rates

The average measured lengths and diameters of the NWs in each patterned area were then used to estimate the average axial and radial growth rates, assuming that they are approximately constant over 15 min of growth. Due to the irregular base of many NWs (see Figure 4.2 (g)), all the NW diameters were measured at the top of the NW just below the gallium droplet. Using the measured tapering angle, the average diameters were then determined for a fixed height of 500 nm.

The results are given in Figure 4.4 (a) and (b) as a function of the pattern pitch for each of the five prepared hole diameters. The axial growth rate shows a slight increase from 500 nm to 1000 nm pitch, and does not vary significantly with the patterned hole diameter.

The radial growth rate, however, increased significantly with increasing pitch from 250 nm to 1000 nm, apparently saturating beyond that point. The radial growth rate also increased slightly with decreasing patterned hole diameter.

4.4 Discussion and Conclusions

We have shown that self-assisted NW arrays grown on nano-patterned oxidized silicon substrates exhibit pronounced radial growth rates that increased with increasing pattern pitch. This suggests that the area of oxide surface surrounding the NWs has an important effect on the NW growth. It has recently been shown, under similar growth conditions as reported here, that the diffusion of both Ga and As adatoms on the surface of the oxide could be negligible [36]. Therefore, it is likely that essentially all the

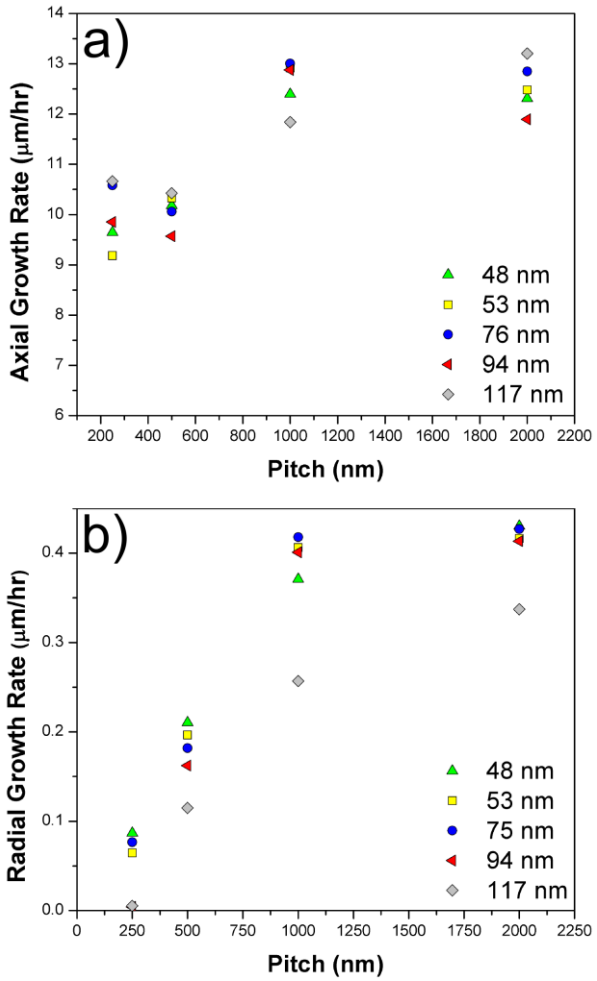

Figure 4.4: (a) Axial and (b) radial growth rates as a function of the pattern pitch. Each data set represents a different prepared hole diameter.

material (both gallium and arsenic species) incident on the surface between the NWs desorbs. If the surface between the NWs does not contribute adatoms via diffusion, it is still possible that a secondary flux of desorbing material may impinge on the NWs and contribute to both radial and axial growth. Shadowing of the surface and crawling NW overgrowth may decrease this secondary flux, accounting for the observed decrease in the axial and radial growth rates for small pitch. Simulations of shadowing in patterned

NW arrays have predicted a significant decrease in the total flux impinging on both NW sidewalls and the surface between the wires for small pattern pitch once the NWs reach a certain height [113].

Despite the fact that the overall NW diameter was not linked to the hole diameter, as it is with selected area epitaxy [114], there were some notable effects. Firstly, as the hole diameter was increased a distinct pedestal was observed to develop at the base of the NWs. Figure 4.5 (a)-(e) show individual NWs selected from the 2 µm pitch area, and it can be seen that the pedestal becomes sequentially more pronounced as the hole diameter grows. This morphological change is limited to the first few hundred nanometers of the nanowire length close to the base, and likely occurs due to crystallite growth on the vacant oxide-free area within the patterned hole [85,94]. This crystallite growth may compete for growth material (via sidewall diffusion) in the early stages of the growth, reducing the overall axial and radial growth rates somewhat for NWs grown in holes much larger than the initial Ga seed diameter.

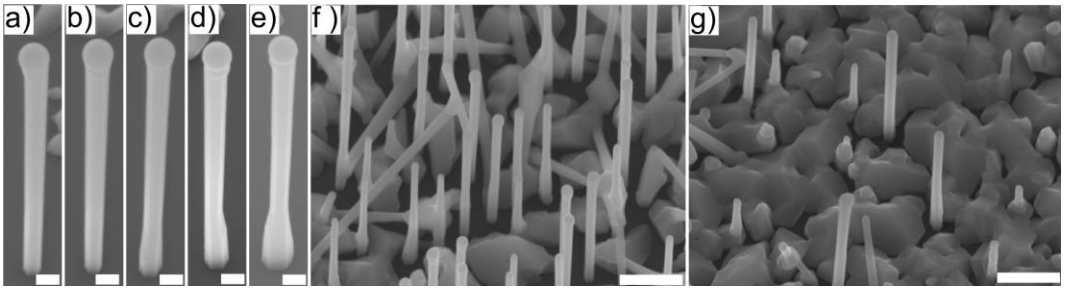

Figure 4.5: SEM images of patterned areas with 2 µm pitch holes and (a) 48, (b) 53, (c) 75, (d) 94 and (e) 117 nm hole diameters after 15 min MBE growth. SEM images of patterned areas with 2 µm pitch holes with (f) 48 and (g) 117 nm holes. All images are tilted at 25° with 150 nm scale bar for (a)-(f) and 500 nm scale bar for (f)-(g).

The largest diameter holes (117 nm) were also found to have a significantly decreased yield of vertical NWs (~5%) for the smallest pitch (250 nm), with a much greater part of the surface between the wires covered by irregular, crawling NW growth, as illustrated in Figure 4.5 (f)-(g). However, the larger pitches (500 nm, 1 μm and 2 μm) with smaller hole diameters had only slightly higher overall vertical NW yields (+2%).

Ramandi et al. [44] and Rieger et al. [66] have both argued that re-evaporation of arsenic from both substrate and NW sidewalls significantly contributes to self-assisted NW growth on unpatterned, oxide covered substrates on the basis that the flux of arsenic species from direct impingement and surface diffusion was not sufficient to account for observed axial growth rates. Indeed, the axial growth rates calculated in Figure 4.2 (a) are very high; 10-13 times higher than the nominal thin film growth rate (i.e. 1 μm/hr). Given that arsenic is expected to have very low diffusivity on the NW sidewall and oxide surfaces, no diffusion flux of arsenic should contribute to the growth, and therefore must be supplied by some other pathway such as secondary adsorption.

Radial growth is expected to be more pronounced in growth systems where As_2 is the dominant species [77], which is the case for our gas-source MBE. However, Rieger et al. [66] also observed radial growth in unpatterned self-assisted GaAs NWs grown by solid-source MBE, where the arsenic species is As_4. In both cases the NWs were found to have a notable inverse tapering. This is likely due to gallium-rich conditions progressively increasing the diameter of the liquid droplet [36,66], an effect unique to the self-assisted VLS system. It is possible that the inverse tapering of the NWs

may favor step-flow growth on the sidewalls, and could be the mechanism accounting for the increased radial growth observed here.

Therefore, it is likely that evaporation and secondary adsorption of both gallium and arsenic species play an important role in the growth kinetics. Future NW-based device design will require improved control over NW morphology, including the diameter. Significant lateral growth may be used as a tool to obtain larger overall NW diameters while at the same time maintaining the small contact area (e.g. Figure 4.3 (a)) required to prevent misfit dislocations.

5 Model of Patterned Self-assisted Nanowire Growth

This Chapter contains work from "Model of Patterned Self-assisted Nanowire Growth" by Sandra J. Gibson and R.R. LaPierre, which was accepted in August 2014 for publication in Nanotechnology. A mass conservation model is developed which describes both the axial and radial growth rates of self-assisted NWs grown using patterned oxide templates. This model represents a simplified phenomenological treatment of this growth mode, predicting the expected growth rates based solely on considerations related to droplet and array geometry which ultimately control the amount of material collected from each pathway. Particularly, this work presents the first explicit calculation which includes the secondary collection of adatoms desorbing off the oxide layer between the NWs, which must be accounted for in order to achieve the observed accelerated axial growth rates, as well as including the effects of shading from neighboring wires.

5.1 Introduction

A dependence of the axial growth rate on the pattern pitch has frequently been observed in NW growth studies. Pitch dependences in the growth of Au-assisted III-V NW arrays grown by both MBE [113,115] and chemical beam epitaxy (CBE) [116,117] have been previously reported for patterned growth on bare substrates. In these cases an observed decrease of both the axial and radial growth rate with decreasing pitch in dense arrays was attributed to two main factors: shadowing of the direct group-III flux

impinging on the NW sidewalls [113,115], and diffusion of group-III adatoms a finite length on the substrate with subsequent competition between shared collection areas [113,116,117]. In addition, a synergetic growth regime has been observed in Au-assisted NW growth by metal-organic vapor phase epitaxy (MOVPE) [78]. However, this effect is attributed to precursor decomposition behavior and is not generally active in other growth systems such as MBE.

Patterned arrays are also grown by selective area epitaxy (SAE), a technique which uses oxide templates to grow NWs without the aid of metal droplets [118]. Elevated temperatures confine growth to the patterned openings and favor axial growth by elongation of the sidewall facets. SAE growth of both GaAs [97] by MBE and InAs arrays by both MBE [29,119] and MOVPE [120] have shown decreasing growth rates with decreasing pattern pitch, which has also been attributed to competition for group-III adatoms.

Nanowire growth via a combined approach called selected-area VLS (SA-VLS) has recently been shown to have great potential for producing uniform patterned arrays. This technique combines both selective growth, avoiding accompanying film/crystallite growth on the surface between the NWs, and the use of a liquid seed particle for growth via the vapor-liquid-solid (VLS) mechanism. The SA-VLS process involves a masking layer (usually a few hundred Angstroms of oxide) which is lithographically patterned and etched to expose the underlying substrate in a regular array of nanoscale openings. During a self-assisted process, liquid group-III droplets collect within the holes in the early phase of the deposition, often aided by a short “pre-

deposition" of group-III material. MBE growth of Ga-assisted GaAs NWs using this technique was initially demonstrated by Bauer et al. [26] on GaAs (111)B and by Plissard et al. [25,87] on Si (111). Other examples of this method include the recent works by Heiss et al. [29] and Munshi et al. [84]. Each of these studies have systematically shown that technologically important array elements such as vertical NW yield and final NW morphology are very sensitive to a wide range of experimental parameters.

In this work we discuss the details of the SA-VLS growth mechanism and how pattern parameters can strongly affect the subsequent morphology of self-assisted NWs. We have previously characterized both the axial and radial growth rates of patterned self-assisted GaAs NWs grown by MBE [76], and have found that while remaining roughly constant with time, the growth rates decrease strongly with decreasing pattern pitch. Using a simplified analysis we will illustrate how an additional As flux scattered off the oxide surface surrounding the NW can account for the observed axial growth rate and the effect of interhole spacing. We also propose that secondary adsorption of Ga scattered off the oxide surface can account for the radial growth rate.

5.2 Experimental Details

As described previously [75,76], electron beam lithography (EBL) was used to define 48 nm diameter holes with several different values of pattern pitch (250, 500 1000 and 2000 nm) in a thin (230 ± 20 Å) SiO_x layer which was thermally grown on Si(111) substrates. Immediately prior to loading in the UHV chamber of the gas source MBE system, the prepared substrates were etched in a 1% HF solution for 60 s to

remove any native oxide from the bottom of the holes. Substrate de-gassing was then performed at 300 °C for 15 min, after which the temperature was ramped to the final growth temperature of 630 °C. The deposition was performed with an As/Ga flux ratio of 1.8 and 2-D equivalent Ga impingement rate of 1 μm/h. Ga was pre-deposited for 30 seconds to form droplets within the patterned openings, immediately followed by initiating the As flux to commence NW growth for a total of 5, 10, 15 and 20 minutes. Arsenic flux was supplied in the form of As_2. The samples were cooled under As_2 flux after growth.

Figure 5.1 shows typical results obtained in patterns with 48 nm diameter holes after 20 minutes of growth. For the largest pitch of 2 μm (Figure 5.1(a)), the NWs have the highest axial and radial growth rates, the former being almost twice the rate expected due to the directly impinging As alone. Some NWs grow along non-vertical directions, likely caused by three-dimensional twinning during the initial nucleation phase [57]. The surface between the NWs was free of parasitic film growth with only a few droplets of Ga visible on the oxide. In denser arrays both the axial and radial growth rates drop sharply, which can be seen in the 250 nm pitch pattern shown in Figure 5.1 (b). We also note that NWs at the edge also have longer lengths and larger diameters compared to those in the interior of the array. The oxide surface outside of the patterns is clean, indicating a zero sticking probability of adatoms under the growth conditions used. A slight inverse tapering (<1.5%) is apparent in patterns with the largest spacing (2 μm). The recorded radii were therefore consistently measured at the top of the NWs,

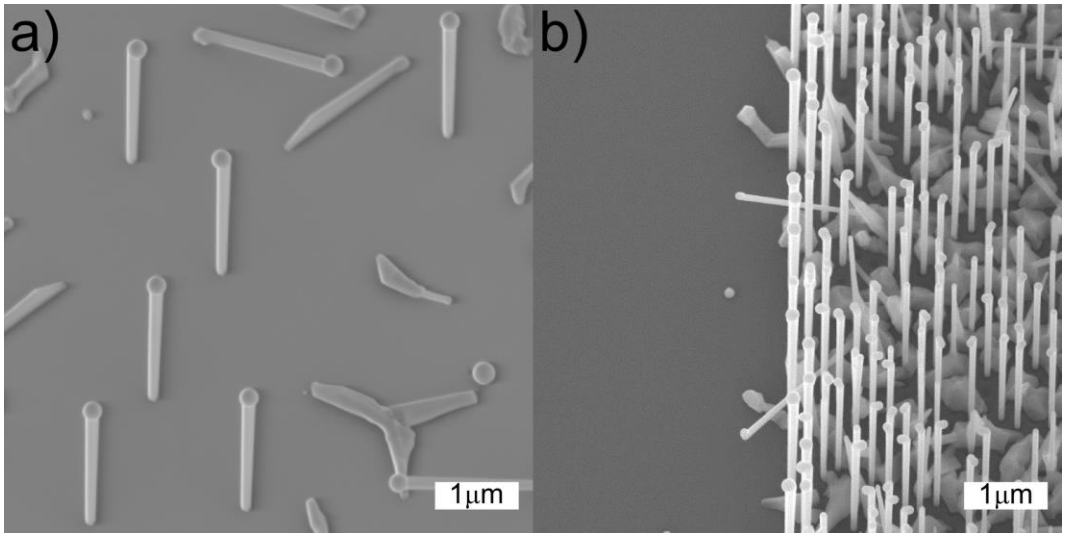

Figure 5.1: Scanning electron microscopy (SEM) images (30° tilt) of self-assisted GaAs NW arrays grown in patterns on Si(111). Areas patterned with 48 nm diameter holes having (a) 2 μm and (b) 250 nm pitch, which show the differences in NW morphology.

directly below the Ga droplet. All measurements were taken from the center of the array, away from the pattern edges.

5.3 Model Description

First, we consider the axial growth of the Ga-assisted GaAs NWs. We assume that axial growth is group-V limited as appropriate for Ga-assisted growth. The axial growth rate of the NWs is far in excess of that which can be accounted for solely by the molecular beams that impinge directly on the droplet surface [26,44,95,121]. The excess As supply may be due to diffusion from the substrate surface or NW sidewalls, or due to secondary desorption off the surrounding oxide mask. Estimates of the diffusion lengths of As adatoms on the oxide surface have shown the growth to be effectively desorption-limited in the range of growth conditions commonly used for Ga-assisted

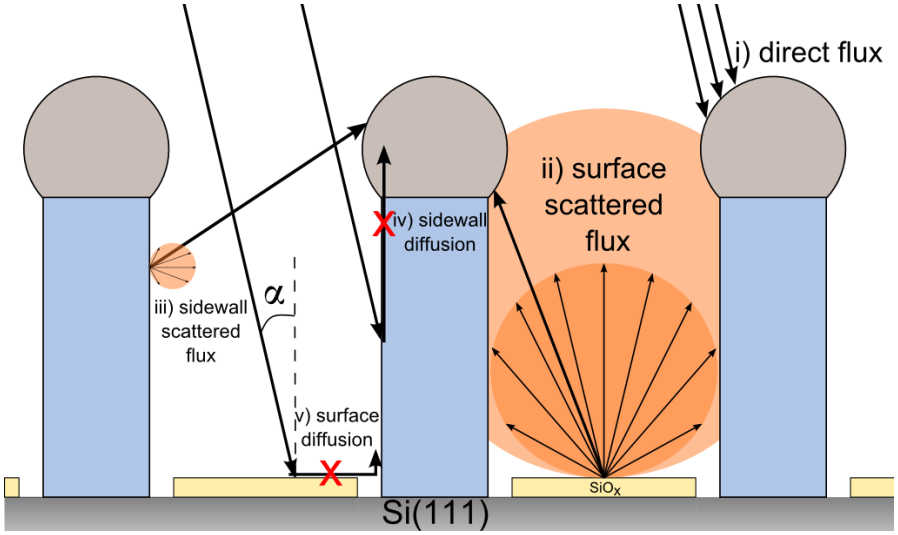

Figure 5.2: The different possible pathways for As flux to reach the droplet and contribute to axial growth: (i) direct flux impinging on the droplet at incoming angle α, or re-emitted flux of material desorbing off the (ii) oxide surface or (iii) neighboring nanowire sidewalls. There should be no significant contribution of As diffusing from either the (iv) sidewalls or (v) the oxide surface.

GaAs growth [36]. The surface diffusion of As over long distances (hundreds of nanometers) on the NW sidewalls or oxide is not expected based on theory [36] and experiment [44]. Therefore, the source of excess As responsible for fast axial growth must be the secondary adsorption of As re-emitted from the surrounding environment [44,95].

Figure 5.2 illustrates the different possible contributions to the overall As flux. In addition to the direct beam (i), As desorbing off the oxide surface (ii) and off the neighboring NW sidewalls (iii) might also potentially reach the droplet. However, as mentioned above, there will be no significant contribution to axial growth from As diffusing from sidewalls (iv) or the oxide surface (v). In previous treatments the

scattered contributions have been assumed to be proportional to the directly impinging flux, and its magnitude was fit to the experimental data [95]. This has been supported through experiments with self-assisted NWs grown on thin native oxides [17,44,121] and by recently presented growth models [36,95]. However, to predict the actual growth rates expected in arrays of different density, the expected magnitude of this secondary flux should be characterized. In particular, secondary adsorption of adatoms desorbing from the oxide surface surrounding the NWs has been previously discussed as an alternate route for adatom incorporation in self-assisted growth [36,44,55,66,76]. In the next section we calculate this contribution and characterize it as a function of the pattern pitch as the NW growth progresses.

Readsorption of adatoms desorbing from neighboring NW sidewalls (pathway (iii) in Figure 5.2) may also be a substantial source of group-V material, and this contribution has been recently proposed as the dominant pathway in several studies [44,122]. However, when sidewall scattered flux dominates, the axial NW growth rate would be expected to increase with increasing NW density, which is the opposite trend compared with our experimental observations. Therefore, we do not explicitly account for this contribution here, but will discuss the general implications further on.

In a study of Au-assisted InP NWs grown by SA-VLS [123], the growth mode was characterized by a significant additional secondary flux of adatoms impinging on the NW sidewalls due to complete desorption off the oxide surface. All adatoms directly impinging on the substrate surface between the NWs were assumed to scatter off the

substrate with a cosine law distribution. In a similar manner, we focus here on As_2 re-emission from the oxide surface. Due to the limited diffusion length of As_2 on the NW sidewalls and oxide surface under the present growth conditions, we further assume that only As_2 scattered directly onto the droplet surface contributes to axial growth.

Assuming a cylindrical NW with instantaneous length L and radius R, the contribution to the nanowire length (dL) per equivalent deposited film layer (dh) can be written as:

$$\frac{dL}{dh} = \kappa_1 \left(\frac{dL}{dh_{\mathrm{d}}} + \frac{dL}{dh_{\mathrm{s}}} \right) \tag{5.1}$$

where $\left(\frac{dL}{dh_{\mathrm{d}}} \right)$ and $\left(\frac{dL}{dh_{\mathrm{s}}} \right)$ are the contributions from direct and re-emitted (scattered) As flux, and the incorporation factor κ_1 represents subsequent losses through desorption from the droplet.

We assume the contact angle β of the droplet is stationary. With an incoming beam angle of $\alpha = 33^\circ$, the contact angle (found to be β = 145°) always satisfies $\beta \geq \alpha + 90^\circ$; therefore the contribution of the direct beam will be [124]:

$$\frac{dL}{dh_{\mathrm{d}}} = \left(\frac{1}{\sin^2 \beta} \right) \tag{5.2}$$

Next, we estimate the contribution to axial growth from subsequent As desorption from the oxide by assuming a cosine law distribution of the re-emitted flux.

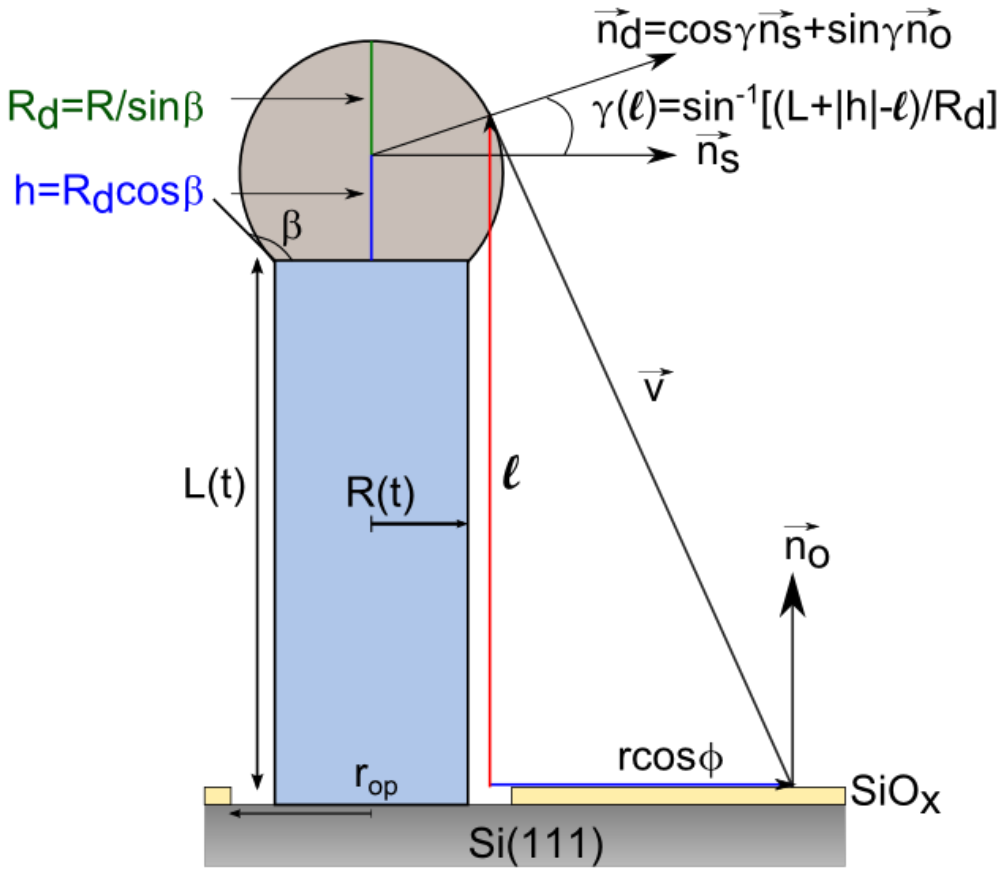

Figure 5.3: Geometry used in the calculation of the As flux re-emitted from a point on the oxide surface and intercepted by a point on the droplet surface.

In this case we must integrate the As flux impinging only on the curved surface of the droplet. The modified geometry used is illustrated in Figure 5.3.

Following a treatment similar to Ref. [123], a point on the Ga droplet surface at a height ℓ collects a flux of As originating from a point on the oxide surface defined by a horizontal distance r and an angle ϕ, connected by the vector $\vec{v}$. The oxide surface starts at the larger of either the edge of the patterned opening $\left(r_{op}\right)$ or the

instantaneous NW radius $R(t)$, as the NW will eventually overgrow the hole. The incremental axial growth due to this material is [123]:

$$dh_o = \frac{dh}{\pi}\left(\frac{\left(\overrightarrow{n_d}\cdot\vec{v}\right)\left(\overrightarrow{n_o}\cdot\vec{v}\right)}{\left(\vec{v}\cdot\vec{v}\right)^2}\right)rdrd\phi = \frac{dh}{\pi}\left(\frac{\cos\gamma\ell r^2\cos\phi}{\left(r^2+\ell^2\right)^2}+\frac{\sin\gamma\ell^2 r}{\left(r^2+\ell^2\right)^2}\right)drd\phi \quad (5.3)$$

where $\overrightarrow{n_o}$ and $\overrightarrow{n_d}$ are the surface normal to the oxide and the droplet, respectively, and $\vec{v}$ is the vector between them. For convenience, $\overrightarrow{n_d}$ has been re-expressed in terms of $\overrightarrow{n_o}$ and $\overrightarrow{n_s}$, the normal to the sidewall surface:

$$\overrightarrow{n_d} = \cos\gamma\overrightarrow{n_s} + \sin\gamma\overrightarrow{n_o} \quad (5.4)$$

where the angle γ between $\overrightarrow{n_d}$ and $\overrightarrow{n_s}$ is given by:

$$\gamma(\ell) = \sin^{-1}\left(\frac{L+|h|-\ell}{R_d}\right) \quad (5.5)$$

where R_d is the droplet radius and h is the distance from the droplet center to the NW top facet as illustrated in Figure 5.3.

The volume of material collected by the droplet over an element of height $d\ell$ is obtained by integrating over the exposed surface of the oxide ($r_0 \le r \le \infty$ where $r_0 = \max\left(r_{op}, R(t)\right)$ and $0 \le \phi \le \pi/2$ with a factor of 2) and multiplying by the circumference of the droplet. The increase in wire height L is then obtained by

integrating over the height of the droplet ($L \le \ell \le \ell_{\max}$ where $\ell_{\max} = \frac{R}{\sin\beta}(1-\cos\beta)$) and then dividing by the crystallized facet area at the top of the NW, which gives:

$$\frac{dL}{dh_s} = \int_{r_0}^{\infty} dr \int_{L}^{\ell_{\max}} d\ell \int_{0}^{\pi/2} d\phi \left[\left(\frac{2\pi R \cos\gamma}{\sin\beta} \right) \left(\frac{2\ell \cos\gamma \cdot r^2 \cos\phi}{(r^2+\ell^2)^2} - \frac{2\ell^2 \sin\gamma \cdot r}{(r^2+\ell^2)^2} \right) \left(\frac{1}{\pi R^2} \right) \right] \tag{5.6}$$

The radial growth on the sidewalls must also be included, since an increase in both the size of the droplet and NW sidewall radius is observed [76,84]. This type of droplet expansion is expected if the growth progresses in effectively Ga-rich conditions (i.e. a relatively low V/III flux ratio [36]). Rather than being group-V limited as in the axial VLS growth, we model the radial growth as vapour-solid deposition limited by the group-III flux as is the case in conventional vapour-solid MBE deposition. We therefore express the contributions to the radial growth as:

$$\frac{dR}{dh} = \kappa_2 \left(\frac{dR}{dh_d} + \frac{dR}{dh_s} \right) \tag{5.7}$$

where the overall radial growth rate $\left(\frac{dR}{dh} \right)$ is due to contributions from direct impinging Ga flux $\left(\frac{dR}{dh_d} \right)$ and substrate scattered flux $\left(\frac{dR}{dh_s} \right)$, respectively, impinging on the NW sidewalls, and the incorporation factor κ_2 represents any subsequent losses through desorption or diffusion of Ga along the NW sidewalls to the droplet.

We have assumed that Ga impinging on the oxide quickly desorbs and the Ga supply to the NW from diffusion is negligible. A negligible "sticking coefficient" of Ga on the oxide at our deposition conditions results in the observed selective growth mode, and a low barrier for Ga desorption on the oxide predicts a very short diffusion length [36]. While not precluded by the experimental data, the diffusion of Ga adatoms along the substrate would provide a large flux to the NWs that would necessitate approximately an order of magnitude lower incorporation factor to fit the data. We will show that the observed NW growth evolution can be successfully modeled by neglecting the diffusion pathway, and can instead be successfully explained entirely by a flux of re-emitted adatoms from the oxide surface. The direct and scattered contributions are written, respectively, as:

$$\frac{dR}{dh_{\mathrm{d}}} = \frac{2RL\sin\alpha}{2\pi RL} = \frac{\sin\alpha}{\pi} \tag{5.8}$$

$$\frac{dR}{dh_{\mathrm{s}}} = \int_{r_{op}}^{\infty} dr \int_{0}^{L} d\ell \int_{0}^{\pi/2} d\phi \left(2\pi R\right)\left(\frac{2lr^2\cos\phi}{(r^2+\ell^2)^2}\right)\left(\frac{1}{2\pi RL}\right) \tag{5.9}$$

The final NW length and radius is calculated by numerically integrating the instantaneous growth rates given by Equations (5.1) and (5.7) over the total equivalent deposited planar film thickness. In our case the nominal thin film growth rate is calibrated from previous GaAs growths on (100) GaAs substrates. Since for the case of self-assisted axial growth the regime is As limited, the nominal growth rate $\left(1.0^{\mu m}/_{hr}\right)$ is multiplied by the ratio of As to Ga flux $\left(As/Ga = 1.8\right)$ that was used.

Considering these equations (Equation (5.8) and (5.9)), is not surprising that droplet expansion and radial growth occurs under these growth conditions. Even though the incoming flux of As is higher, Ga adatoms can diffuse long distances the sidewalls [36]. This fact gives them a generally much larger effective collection area from which they may reach and incorporate in the droplet (i.e. the entire sidewall surface) compared to As, which must impinge on the droplet surface in order to be incorporated. Only with higher V/III ratios than used here for patterned growth would the demand for Ga from VLS crystallization be expected to outstrip the supply.

A pre-deposition of group-III material prior to the NW growth is normally carried out, since this step has been found to both pre-form droplets within the opening and significantly influence the vertical NW yield [84,87]. Here we assume that the initial droplet size is independent of the pattern pitch, but varies with the pre-deposition time and the hole diameter. In pre-deposition studies previously conducted [87], no significant change in droplet diameter for increasing pattern density was observed. A significant increase in droplet diameter with increasing hole size was reported, with multiple droplets forming per hole in the largest holes [84,87]. We assume the initial droplet radius r_o was 11 nm, in agreement with the value extrapolated from our previous experiments [76] and with the volume of Ga directly deposited within the 48 nm diameter openings during the 30 s pre-deposition phase.

Lastly, the reduction of the axial and radial growth rates with decreasing pattern pitch corresponds to an increase in the “shading” of the secondary flux by neighboring NWs in the array. Following the method outlined in Ref. [125], the unshaded surface

fraction $\eta(r)$ represents the fraction of the substrate surface at a radial distance r which is not blocked from the "line of sight" of the central NW. This factor will depend on the particular pattern, pitch and the instantaneous NW radius. Including the line-of-sight shading factor in the following discrete sum, the actual contribution to the axial and radial growth rates from substrate scattered flux may be calculated [125]:

$$\frac{dL}{dh_s} = \sum_{i=0}^{\infty} \eta_{r_i} \int_{r_i}^{r_{i+1}} dr \int_{L}^{\ell_{\max}} d\ell \int_{0}^{\pi/2} d\phi \left[\left(\frac{2\pi R \cos\gamma}{\sin\beta} \right) \left(\frac{2\ell \cos\gamma \cdot r^2 \cos\phi}{(r^2+\ell^2)^2} - \frac{2\ell^2 \sin\gamma \cdot r}{(r^2+\ell^2)^2} \right) \left(\frac{1}{\pi R^2} \right) \right]$$

$$\frac{dR}{dh_s} = \sum_{i=0}^{\infty} \eta_{r_i} \int_{r_i}^{r_{i+1}} dr \int_{0}^{L} d\ell \int_{0}^{\pi/2} d\phi \left(2\pi R\right) \left(\frac{2lr^2 \cos\phi}{(r^2+\ell^2)^2} \right) \left(\frac{1}{2\pi RL} \right) \tag{5.10}$$

where η_{r_i} is the unshaded annular surface fraction between the wires at the lattice positions r_{i+1} and r_i, as illustrated in Figure 5.4 (a). The summation begins at the oxide edge $r_0 = \max\left(r_{op}, R(t)\right)$ and is truncated when η_{r_i} approaches zero. Figure 5.4(b) illustrates the calculated reduction in re-emitted adatoms captured due to line-of-sight shading as a function of the distance from the central NW for a perfect hexagonal array of 80 nm diameter NWs.

In addition to this type of "line-of-sight" shading, there is also the shadowing of the direct flux in the array, since the incoming beam impinges at an angle ($\alpha = 33^\circ$). This was characterized for shadowing of both sidewall and substrate adatoms as a function of the NW length and the pattern pitch and is illustrated in Figure 5.4 (c) and (d) for a hexagonal array of identical NWs. The magnitude of the reduction in impinging

adatoms due to direct shadowing was found to be almost identical to the values previously reported by Madsen et al [113] for the example of a square array. It is expected that the effect of the direct flux shadowing becomes more important in dense arrays and as the NW increases in length, which can be seen clearly in these plots.

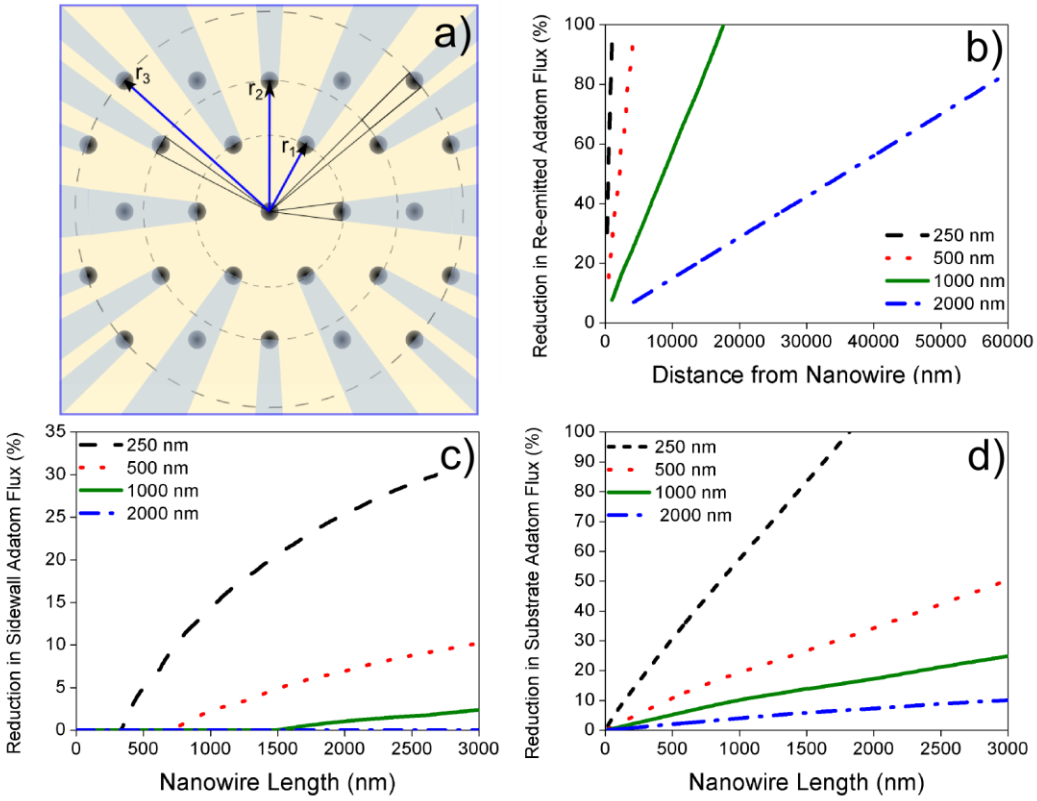

Figure 5.4: (a) Line-of-sight shading of secondary flux desorbing from the oxide surface is estimated by calculating the unshaded fraction of the annular area, η_{r_i}, between the NWs at position r_i and r_{i+1} Vectors defining the first three positions in the hexagonal array are illustrated. (b) Calculated reduction in re-emitted surface adatoms due to line-of-sight shading. (c, d) Reduction in sidewall and substrate adatoms, respectively, calculated as a function of NW length in a hexagonal array with different pattern pitch (250, 500, 1000 and 2000 nm) due to shadowing of the direct flux at $\alpha = 33^{\circ}$ by neighboring nanowires. An 80 nm NW diameter was assumed in each example.

5.4 Results and Discussion

The expected NW length and radius as a function of the pattern pitch was calculated by combining both the direct and re-emitted As flux impinging on the droplet, while also taking into account both the line-of-sight and direct flux shadowing in an array of identical NWs. This was done by solving the equations iteratively, so that the effects of shading and shadowing could be incorporated at each iteration as the NW morphology evolved.

Figure 5.5 illustrates a comparison of the calculated and experimental measurements of the NW length and radius as a function of pattern pitch. The measured radius of the opening was $r_{op} = 24 \text{ nm}$ and the initial droplet radius was $r_o = 11 \text{ nm}$. The parameters used for the calculation were a droplet contact angle $\beta = 145^\circ$ and the incorporation factors $\kappa_1 = 0.8$ and $\kappa_2 = 0.35$, adjusted for best fit with the experimental data. Approximately 80% of the As adatoms impinging on the droplet are incorporated towards axial growth ($\kappa_1 = 0.8$) with the remaining portion presumably lost due to desorption from the droplet, which is reasonable at our growth temperature. Approximately 35% of the Ga adatoms impinging on the sidewalls are incorporated into the sidewall growth ($\kappa_2 = 0.35$). The rest of the Ga flux is expected to diffuse along the NW sidewalls to the droplet where it contributes to the axial growth and to the subsequent droplet expansion.

The incorporation factor κ_1 represents the fraction of the total collected As which contributes to the axial NW growth beneath the droplet as compared with the loss of arsenic from the droplet due to re-evaporation. The incorporation factor κ_2 represents the fraction of Ga adatoms on the NW sidewalls that contribute toward radial growth, with the remainder desorbing or diffusing along the NW sidewalls to the droplet where it contributes to the axial growth and to the subsequent droplet expansion. The complicated thermodynamics of growth are therefore contained in these two parameters, which are obtained by fitting the model to the experimental data. It is beyond the scope of the present model to predict these values theoretically based on factors such as surface energies and deposition conditions, including temperature, impingement rate of growth species, and V/III flux ratio. However, the incorporation factors obtained here might be used in more fundamental studies to estimate unknown thermodynamic parameters.

Good agreement between the data and the calculated length and radius for each pattern pitch was obtained. In the largest pitch patterns (2000 nm), the shading is minimized. If only the directly impinging flux on the droplet is considered, the NWs could be only a maximum length of 1824 nm tall after 20 minutes of growth. Furthermore, the calculated contribution to the axial growth rate due to scattered As flux off the oxide is almost equal to the directly impinging As flux, and so the NW can grow nearly twice as fast. As the pattern pitch is decreased, shading reduces the area of the oxide surface from which the re-emitted flux is collected, and so the growth rate drops accordingly. In addition, our model predicts that NWs at the edges of the dense

patterns should receive both a higher overall As and Ga flux due to less shadowing compared to those NWs uniformly surrounded by neighbors within the array. As the effects of shadowing would be reduced, both axial and radial growth rates at the pattern perimeter should be higher than in the interior, in agreement with our observations (Figure 5.5 (b)).

It is interesting to note that this calculation confirms that there does not need to be a contribution to the axial growth due to As desorbing from the NW sidewalls in order to account for the growth rates observed here. It is likely that the significant radial growth occurring simultaneously on the NW sidewalls captures a large portion of the As incident on the sidewalls, such that the fraction which subsequently desorbs is reduced substantially. However, in a situation where little or no sidewall growth and/or droplet expansion occurs, this contribution could be significant, especially if multiple reflections are considered. This may explain the much higher growth rate elevation relative to the direct flux which has been measured, as well as the reversed direction of the pitch dependence reported in similar MBE studies where no radial growth was reported [26,44].

For typical growth times, both the axial and radial growth rates have been found to be approximately constant [76,84], regardless of hole diameter or pattern pitch [76]. For non-patterned, self-assisted GaAs growth on thin oxides the linear dependence of both length and diameter with increasing growth time has also been reported [46,66]. Figure 5.6 illustrates the calculated evolution of both the NW length and radius with time. After a transition period in the first few minutes of growth, the growth rate is

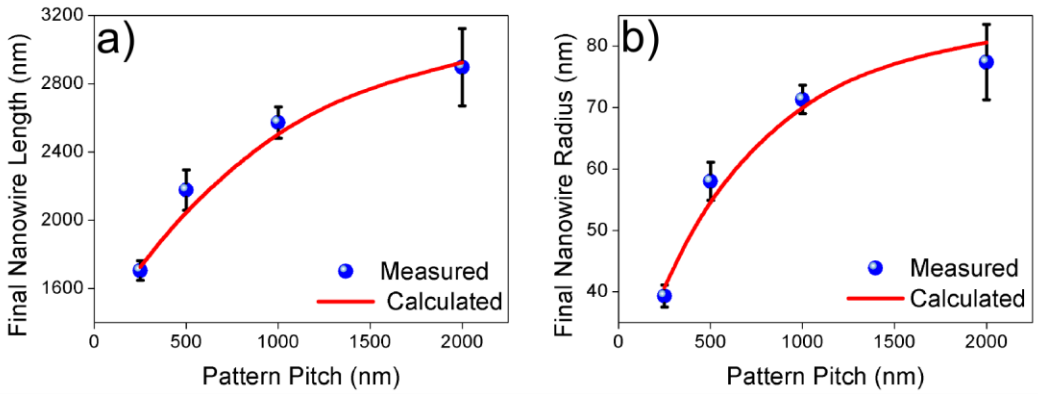

Figure 5.5: Comparison of the calculated (solid line) and experimental measurements (circles) of the final NW (a) length and (b) radius as a function of pattern pitch. The parameters used for the calculation were $r_{op} = 24$ nm, $r_o = 11$ nm, $\beta = 145^\circ$, $\kappa_1 = 0.8$ and $\kappa_2 = 0.35$.

approximately constant and decreases with decreasing array density, in agreement with the experimental results. Deviations from linearity increase slightly with decreasing pattern pitch.

The effects of shading calculated here will not correspond exactly to that during the growth due to some non-vertical NW growth, including the spreading of "crawling" GaAs NWs out of the holes onto the oxide surface. Although there is a fraction of non-vertical NWs in the array, the NWs were typically found in patches with a high yield of vertical NWs where reliable data could be obtained. Any GaAs spreading onto the oxide blocks a surface area that would have contributed to the scattered flux. However, if a vertical NW had grown at the same pattern position, it would also have blocked a

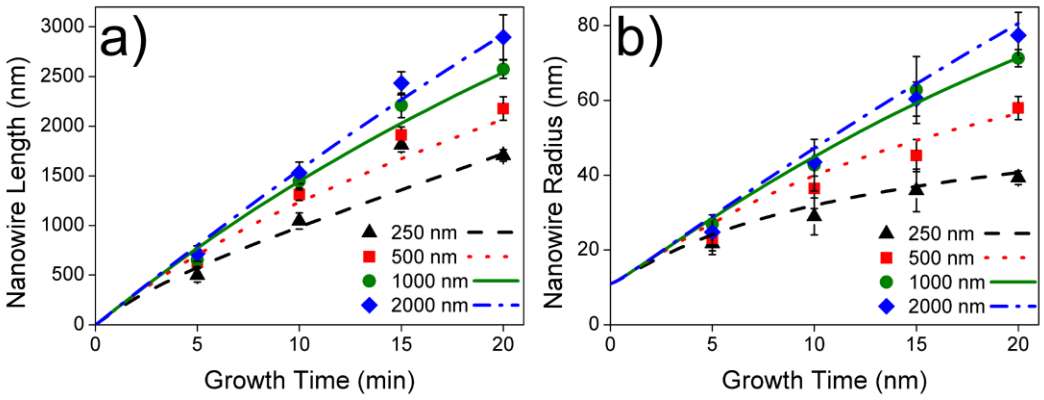

Figure 5.6: Calculated (a) length and (b) radius as a function of growth time and for different pattern pitch (250, 500, 1000 and 2000 nm). The same parameters as used in Figure 5.5 were also used here.

portion of the re-emitted flux. This likely mitigates somewhat any disparity due to these issues, , as evidenced by the height and diameter uniformity of the array array (note the error bars in Figure 5.5 and Figure 5.6).

5.5 Conclusions

Using an explicit geometrical calculation, we have shown significant contribution to the overall axial growth rate from adatoms re-emitted from the oxide surface between the NWs during patterned self-assisted growth. The reduced adatom flux due to both line-of-sight shading and direct shadowing was also estimated numerically for a hexagonal array as a function the pattern pitch and the instantaneous NW radius. This was used to calculate the NW length and radius as a function of time in a regime where significant radial growth and droplet expansion occurs. The final NW morphology predicted was in good agreement with measurements on arrays of different pitch.

Roughly constant axial and radial growth rates were also calculated, in agreement with measurements from previous experimental studies. We believe this model represents the first instance where secondary desorption of both group-V and group-III adatoms off a patterned oxide template has been used to account for the observed NW growth rates, without assuming competition for growth material. Since the important parameters such as the initial droplet size, contact angle and incorporation factors can be determined from just a few experimental results, this model could be used in a straightforward manner to predict and subsequently control the resulting NW dimensions.

6 Summary and Future Work

6.1 Thesis Summary

Positioned arrays of self-assisted GaAs NWs were grown on Si substrates by GS-MBE using patterned oxide templates. In the early process of developing and implementing the EBL patterning process several challenges and key considerations were uncovered. Repeatability and array uniformity requires the attention to any factor which can result in incomplete removal of the oxide layer or native oxide re-growth within the patterned holes, such as oxide quality and thickness variations as well as reactive dry etching effects such as ARDE-lag. As confirmed using cross-sectional TEM analysis, a thick residual oxide layer fully inhibits NW growth, while a thin oxide (several nm's) permits NWs to form by a similar mechanism as for unpatterned growth. This is manifest in a similar linear length-radius dependence, which was explained as resulting from the individual NWs beginning their growth at different times, accompanied by significant radial growth. The spread in obtained NW dimensions was then shown to be significantly decreased by ensuring completely clear holes.

With the ultimate objective of improving vertical NW yields, while at the same time establishing the margins for further device fabrication steps required for realization of a tandem solar cell concept, a number of growth parameters were surveyed. A Ga pre-deposition step was found to be important for producing higher yields of vertical NWs, although success was only obtained with a higher Ga flux (1 μm/hr). Parasitic film growth on the oxide mask can be avoided by maintaining a high enough substrate

temperature in combination with lower growth rates. Although the original Ga droplet was shown to be consumed during a pause with As overpressure, the undesired subsequent reformation of a VLS Ga droplet was observed during a preliminary attempt to form a radial p-n junction. In order to obtain uniform shells in the future, this process must be avoided through further decreases in growth rate and V/III flux ratio. Collaborative nanoprobe measurements indicated that a nominal Si doping level of 4 x 10^{18} cm^{-3} was insufficient to achieve conduction. As an alternative p-type dopant, Be was found to increase Ga droplet collection on the oxide mask. An investigation into the effect of oxide thickness was found to be complicated by the ARDE-lag effect, which can result in the production of different sized holes and underetching if the total etch time is kept constant. This effect may account for the previously reported dependence of the vertical NW yield on oxide thickness. Vertical NW yield and interface roughness was found to be very sensitive to the effective Si opening size, although the detailed cause is yet unclear and the apparent opening size which maximized vertical yield is challenging to reproduce in practice (~20 nm).

By performing several growths of different duration under identical conditions and with identical sample preparation, the axial and radial NW growth rates were systematically characterized, for the first time evaluating the effect of both interwire spacing and opening diameter. These results confirmed not only that significant accompanying radial growth occurs, but the growth rates increase significantly with increasing pattern pitch.

Using the hypothesis that the pitch dependence of the growth rates is due to shading of a significant flux of material desorbing from the oxide surface between the NWs, a phenomenological model was developed. This model is able to accurately predict the experimentally observed NW lengths and diameters as they evolve with increasing deposition time. This was done through the development of an explicit geometrical account of secondary adatom collection on both the droplet and sidewall from the scattered surface flux of both growth species. This secondary flux contribution had not previously been characterized in such a specific format. Therefore this work may eventually be used to inform more fundamental and comprehensive thermodynamic and kinetic models of this complex growth mode.

Ultimately, this work contributes to the overall understanding and development of a relatively new technique for patterned self-assisted NW growth and constitutes a step toward the realization of GaAs technologies on an integrated Si platform.

6.2 Future Work

Although much of the results presented here and by other recent reports corroborate the expected potential of this fabrication technique for producing high-quality NW arrays, there remains significant additional work to be done towards improving this fabrication method for future device applications.

Firstly, some additional effort should be applied to generating a more reliable and anisotropic dry etching procedure. In particular, the use of thinner EBL resist layers

could greatly reduce the effect of ARDE-lag. The further optimization of RIE dry etch parameters such as chamber pressure, power and even etch chemistry beyond that available in the table-top Technics system used here could certainly go a long way towards improving the etch anisotropy and cleanliness of this step of the process. Damage or contamination caused to the Si substrate due to overetching in the RIE step may be one factor limiting the obtained vertical NW yields, and certainly should be avoided if at all possible. In fact, if more reliable control of the pattern transfer step is attained, it should be possible to underetch by a specific amount in order to maintain a thin protective layer which can be removed by the final HF etch step prior to loading. There is also some indication in the literature that the use of aqueous ammonium fluoride (NH_4F) to remove native oxide rather than dilute HF may provide some additional benefit in smoothing Si(111) surfaces in particular [126,127], although making this change made no obvious improvement when attempted during the course of this work. Improvements to the EBL process include the use of lower beam currents to produce progressively smaller spots, although at this point solving the etching issues are likely more pressing.

Further investigation of the effect and importance of including an additional high temperature pre-annealing step (700 - 900°C) within the UHV environment prior to NW growth should be pursued, as this has recently been shown to greatly improve vertical NW yields on its own [29,32,84], although the cause has yet to be determined.

This should be followed by further optimization of the deposition conditions, most importantly Ga pre-deposition time, V/III flux ratio and substrate temperature, in

order to achieve higher vertical NW yields. Once this goal is achieved, further improvements such as the elimination of polytypism and planar defects from the NW as well as the controlled doping and radial junction formation, which will each eventually be required for future device applications, should be more fully pursued.

7 Bibliography

[1] S. Nadj-Perge, S. M. Frolov, E. P. A. M. Bakkers, and L. P. Kouwenhoven, Nature **468**, 1084 (2010).

[2] V. Mourik, K. Zuo, S. M. Frolov, S. R. Plissard, E. P. A. M. Bakkers, and L. P. Kouwenhoven, Science (80-.). **336**, 1003 (2012).

[3] H. J. Joyce, Q. Gao, H. H. Tan, C. Jagadish, Y. Kim, J. Zou, L. M. Smith, H. E. Jackson, J. M. Yarrison-Rice, P. Parkinson, M. B. Johnston, and H. Hoe Tan, Prog. Quantum Electron. **35**, 23 (2011).

[4] X. Duan, Y. Huang, R. Agarwal, and C. M. Lieber, Nature **421**, 241 (2003).

[5] F. Qian, Y. Li, S. Gradecak, H.-G. Park, Y. Dong, Y. Ding, Z. L. Wang, and C. M. Lieber, Nat. Mater. **7**, 701 (2008).

[6] M. P. van Kouwen, M. H. M. van Weert, M. E. Reimer, N. Akopian, U. Perinetti, R. E. Algra, E. P. A. M. Bakkers, L. P. Kouwenhoven, and V. Zwiller, Appl. Phys. Lett. **97**, 113108 (2010).

[7] C. P. T. Svensson, T. Mårtensson, J. Trägårdh, C. Larsson, M. Rask, D. Hessman, L. Samuelson, and J. Ohlsson, Nanotechnology **19**, 305201 (2008).

[8] P. Krogstrup, H. I. Jørgensen, M. Heiss, O. Demichel, J. V. Holm, M. Aagesen, J. Nygard, and A. Fontcuberta i Morral, Nat. Photonics **7**, 306 (2013).

[9] J. V Holm, H. I. Jørgensen, P. Krogstrup, J. Nygård, H. Liu, and M. Aagesen, Nat. Commun. **4**, 1498 (2013).

[10] T. Bryllert, L.-E. Wernersson, T. Löwgren, and L. Samuelson, Nanotechnology **17**, S227 (2006).

[11] Y. Li, F. Qian, J. Xiang, and C. M. Lieber, Mater. Today **9**, 18 (2006).

[12] H. A. Nilsson, T. Duty, S. Abay, C. Wilson, J. B. Wagner, C. Thelander, P. Delsing, and L. Samuelson, Nano Lett. **8**, 872 (2008).

[13] R. S. Wagner and W. C. Ellis, Appl. Phys. Lett. **4**, 89 (1964).

[14] M. Law, J. Goldberger, and P. Yang, Annu. Rev. Mater. Res. **34**, 83 (2004).

[15] P. Yang, R. Yan, and M. Fardy, Nano Lett. **10**, 1529 (2010).

[16] K. A. Dick, Prog. Cryst. Growth Charact. Mater. **54**, 138 (2008).

[17] C. Colombo, D. Spirkoska, M. Frimmer, G. Abstreiter, and A. Fontcuberta i Morral, Phys. Rev. B **77**, 155326 (2008).

[18] A. Fontcuberta i Morral, C. Colombo, G. Abstreiter, J. Arbiol, and J. R. Morante, Appl. Phys. Lett. **92**, 063112 (2008).

[19] B. Mandl, J. Stangl, E. Hilner, A. A. Zakharov, K. Hillerich, A. W. Dey, L. Samuelson, G. Bauer, K. Deppert, A. Mikkelsen, and I. Nanowires, Nano Lett. **10**, 4443 (2010).

[20] A. Fontcuberta i Morral, IEEE J. Sel. Top. Quantum Electron. **17**, 819 (2011).

[21] S. Wright and H. Kroemer, Appl. Phys. Lett. **36**, 210 (1980).

[22] M. H. Madsen, M. Aagesen, P. Krogstrup, C. Sørensen, and J. Nygård, Nanoscale Res. Lett. **6**, 516 (2011).

[23] E. Russo-Averchi, M. Heiss, L. Michelet, P. Krogstrup, J. Nygard, C. Magen, J. R. Morante, E. Uccelli, J. Arbiol, and A. Fontcuberta i Morral, Nanoscale **4**, 1486 (2012).

[24] F. Matteini, G. Tütüncüoğlu, D. Rüffer, E. Alarcón-Lladó, and A. Fontcuberta i Morral, J. Cryst. Growth **404**, 246 (2014).

[25] S. Plissard, K. A. Dick, G. Larrieu, S. Godey, A. Addad, X. Wallart, and P. Caroff, Nanotechnology **21**, 385602 (2010).

[26] B. Bauer, A. Rudolph, M. Soda, A. Fontcuberta, J. Zweck, D. Schuh, E. Reiger, and A. Fontcuberta i Morral, Nanotechnology **21**, 435601 (2010).

[27] B. Mandl, A. W. Dey, J. Stangl, M. Cantoro, L.-E. Wernersson, G. Bauer, L. Samuelson, K. Deppert, and C. Thelander, J. Cryst. Growth **334**, 51 (2011).

[28] K. A. Dick and P. Caroff, Nanoscale **6**, 3006 (2014).

[29] M. Heiss, E. Russo-Averchi, A. Dalmau-Mallorquí, G. Tütüncüoğlu, F. Matteini, D. Rüffer, S. Conesa-Boj, O. Demichel, E. Alarcon-Lladó, and A. Fontcuberta i Morral, Nanotechnology **25**, 014015 (2014).

[30] C. J. Novotny and P. K. L. Yu, Appl. Phys. Lett. **87**, 203111 (2005).

[31] M. Pozuelo, H. Zhou, S. Lin, S. A. Lipman, M. S. Goorsky, R. F. Hicks, and S. Kodambaka, J. Cryst. Growth **329**, 6 (2011).

[32] Y. Zhang, J. Wu, M. Aagesen, J. Holm, S. Hatch, M. Tang, S. Huo, and H. Liu, Nano Lett. **14**, 4542 (2014).

[33] S. Plissard, K. A. Dick, X. Wallart, and P. Caroff, Appl. Phys. Lett. **96**, 121901 (2010).

[34] M. Heiss, B. Ketterer, E. Uccelli, J. R. Morante, J. Arbiol, and A. Fontcuberta i Morral, Nanotechnology **22**, 195601 (2011).

[35] V. G. Dubrovskii, *Nucleation Theory and Growth of Nanostructures* (Springer-Verlag, Berlin Heidelberg, 2014).

[36] P. Krogstrup, H. I. Jørgensen, E. Johnson, M. H. Madsen, C. B. Sørensen, A. F. I. Morral, M. Aagesen, J. Nygård, and F. Glas, J. Phys. D. Appl. Phys. **46**, 313001 (2013).

[37] F. Glas, J.-C. Harmand, and G. Patriarche, Phys. Rev. Lett. **104**, 135501 (2010).

[38] D. Kashchiev, Cryst. Growth Des. **6**, 1154 (2006).

[39] V. Dubrovskii, G. Cirlin, I. Soshnikov, A. Tonkikh, N. Sibirev, Y. Samsonenko, and V. Ustinov, Phys. Rev. B **71**, 5 (2005).

[40] M. C. Plante and R. R. LaPierre, J. Appl. Phys. **105**, 114304 (2009).

[41] J. Johansson, C. P. T. Svensson, T. Mårtensson, L. Samuelson, and W. Seifert, J. Phys. Chem. B **109**, 13567 (2005).

[42] J. P. Boulanger and R. R. LaPierre, J. Cryst. Growth **388**, 116 (2014).

[43] V. Dubrovskii, N. Sibirev, G. Cirlin, I. Soshnikov, W. H. Chen, R. Larde, E. Cadel, P. Pareige, T. Xu, B. Grandidier, J.-P. Nys, D. Stievenard, M. Moewe, L. Chuang, and C. Chang-Hasnain, Phys. Rev. B **79**, 1 (2009).

[44] M. R. Ramdani, J. C. Harmand, F. Glas, G. Patriarche, and L. Travers, Cryst. Growth Des. **13**, 91 (2013).

[45] J. H. Paek, T. Nishiwaki, M. Yamaguchi, and N. Sawaki, Phys. Status Solidi **6**, 1436 (2009).

[46] G. Priante, S. Ambrosini, V. G. Dubrovskii, A. Franciosi, and S. Rubini, Cryst. Growth Des. **13**, 3976 (2013).

[47] M. Heiss, S. Conesa-Boj, J. Ren, H.-H. Tseng, A. Gali, A. Rudolph, E. Uccelli, F. Peiró, J. Morante, D. Schuh, E. Reiger, E. Kaxiras, J. Arbiol, and A. Fontcuberta i Morral, Phys. Rev. B **83**, 1 (2011).

[48] D. Spirkoska, J. Arbiol, a. Gustafsson, S. Conesa-Boj, F. Glas, I. Zardo, M. Heigoldt, M. H. Gass, a. L. Bleloch, S. Estrade, M. Kaniber, J. Rossler, F. Peiro, J. R. Morante, G. Abstreiter, L. Samuelson, and a. Fontcuberta i Morral, Phys. Rev. B **80**, 1 (2009).

[49] F. Glas, J.-C. Harmand, and G. Patriarche, Phys. Rev. Lett. **99**, 3 (2007).

[50] P. Krogstrup, S. Curiotto, E. Johnson, M. Aagesen, J. Nygård, and D. Chatain, Phys. Rev. Lett. **106**, 1 (2011).

[51] M. D. Stiles and D. R. Hamann, Phys. Rev. B **38**, (1988).

[52] M. D. Stiles and D. R. Hamann, Phys. Rev. B **41**, 5280 (1990).

[53] G. Cirlin, V. Dubrovskii, Y. Samsonenko, a. Bouravleuv, K. Durose, Y. Proskuryakov, B. Mendes, L. Bowen, M. Kaliteevski, R. Abram, and D. Zeze, Phys. Rev. B **82**, 1 (2010).

[54] V. G. Dubrovskii, G. E. Cirlin, N. V Sibirev, F. Jabeen, J. C. Harmand, and P. Werner, Nano Lett. **11**, 1247 (2011).

[55] P. Krogstrup, R. Popovitz-Biro, E. Johnson, M. H. Madsen, J. Nygård, and H. Shtrikman, Nano Lett. **10**, 4475 (2010).

[56] W. Braun, V. M. Kaganer, A. Trampert, H. Scho, Q. Gong, R. No, L. Da, and K. H. Ploog, J. Cryst. Growth **228**, 51 (2001).

[57] E. Uccelli, J. Arbiol, C. Magen, P. Krogstrup, E. Russo-averchi, M. Heiss, G. Mugny, J. Nyg, J. R. Morante, and A. Fontcuberta i Morral, Nano Lett. **11**, 3827 (2011).

[58] S. A. Fortuna and X. Li, Semicond. Sci. Technol. **25**, 024005 (2010).

[59] L. C. Chuang, M. Moewe, C. Chase, N. P. Kobayashi, C. Chang-Hasnain, and S. Crankshaw, Appl. Phys. Lett. **90**, 043115 (2007).

[60] G. E. Cirlin, V. G. Dubrovskii, I. P. Soshnikov, N. V. Sibirev, Y. B. Samsonenko, A. D. Bouravleuv, J. C. Harmand, and F. Glas, Phys. Status Solidi - Rapid Res. Lett. **3**, 112 (2009).

[61] A. Biermanns, S. Breuer, A. Trampert, A. Davydok, L. Geelhaar, and U. Pietsch, Nanotechnology **23**, 305703 (2012).

[62] F. Glas, Phys. Rev. B **74**, 121302 (2006).

[63] C. M. Haapamaki, J. Baugh, and R. R. LaPierre, J. Appl. Phys. **112**, 124305 (2012).

[64] S. Raychaudhuri and E. T. Yu, J. Appl. Phys. **99**, 114308 (2006).

[65] D. Spirkoska, C. Colombo, M. Heiss, G. Abstreiter, and A. Fontcuberta i Morral, J. Phys. Condens. Matter **20**, 454225 (2008).

[66] T. Rieger, S. Heiderich, S. Lenk, M. I. Lepsa, and D. Grützmacher, J. Cryst. Growth **353**, 39 (2012).

[67] A. J. Tavendale and S. J. Pearton, J. Phys. C Solid State Phys. **16**, 1665 (1983).

[68] D. E. Perea, J. E. Allen, S. J. May, B. W. Wessels, D. N. Seidman, and L. J. Lauhon, Nano Lett. **6**, 181 (2006).

[69] M. Bar-Sadan, J. Barthel, H. Shtrikman, and L. Houben, Nano Lett. **12**, 2352 (2012).

[70] S. Breuer, C. Pfüller, T. Flissikowski, O. Brandt, H. T. Grahn, L. Geelhaar, H. Riechert, and C. Pf, Nano Lett. **11**, 1276 (2011).

[71] N. Jiang, Q. Gao, P. Parkinson, J. Wong-Leung, S. Mokkapati, S. Breuer, H. H. Tan, C. L. Zheng, J. Etheridge, and C. Jagadish, Nano Lett. **13**, 5135 (2013).

[72] R. R. LaPierre, A. C. E. Chia, S. J. Gibson, C. M. Haapamaki, J. Boulanger, R. Yee, P. Kuyanov, J. Zhang, N. Tajik, N. Jewell, and K. M. A. Rahman, Phys. Status Solidi - Rapid Res. Lett. **7**, 815 (2013).

[73] R. R. LaPierre, J. Appl. Phys. **110**, 014310 (2011).

[74] B. M. Kayes, H. A. Atwater, and N. S. Lewis, J. Appl. Phys. **97**, 114302 (2005).

[75] S. J. Gibson, J. P. Boulanger, and R. R. LaPierre, Semicond. Sci. Technol. **28**, 105025 (2013).

[76] S. Gibson and R. LaPierre, Phys. Status Solidi - Rapid Res. Lett. **7**, 845 (2013).

[77] C. Sartel, D. L. Dheeraj, F. Jabeen, and J. C. Harmand, J. Cryst. Growth **312**, 2073 (2010).

[78] M. T. Borgström, G. Immink, B. Ketelaars, R. Algra, and E. P. A. M. Bakkers, Nat. Nanotechnol. **2**, 541 (2007).

[79] L. Reimer, *Scanning Electron Microscopy,* (Springer-Verlag, Berlin, 1985).

[80] E. Hecht, *Optics* (Addison Wesley, San Francisco, 2002).

[81] D. B. Williams and C. B. Carter, *Transmission Electron Microscopy* (Plenum Press, New York, 1996).

[82] P. Gnauck, P. Hoffrogge, and J. Greiser, *A New CrossBeam Inspection Tool Combining an Ultrahigh Resolution Field Emission SEM and a High Resolution FIB* (WWW Document, Http://www.zeiss.com/, Accesed on August 20, 2014, n.d.).

[83] L. A. Giannuzzi and F. A. Stevie, *Introduction to Focussed Ion Beams* (Springer, New York, 2005).

[84] A. M. Munshi, D. L. Dheeraj, V. T. Fauske, D.-C. C. Kim, J. Huh, J. F. Reinertsen, L. Ahtapodov, K. D. Lee, B. Heidari, A. T. J. van Helvoort, B.-O. O. Fimland, and H. Weman, Nano Lett. **14**, 960 (2014).

[85] Zhang, Y, J. Wu, M. Aagesen, J. Holm, S. Hatch, M. Tang, S. Huo, and H. Liu, Nano Lett. **14**, 4542 (2014).

[86] A. S. Jugessur, M. Yagnyukova, and J. S. Aitchison, J. Vac. Sci. Technol. B Microelectron. Nanom. Struct. **29**, 06FF06 (2011).

[87] S. Plissard, G. Larrieu, X. Wallart, and P. Caroff, Nanotechnology **22**, 275602 (2011).

[88] J. Plummer, M. Deal, and G. PB, *Silicon VLSI Technology; Fundamentals, Practice and Modeling*, volume 1 (Prentice Hall Inc., Upper Saddle River New Jersey, 2000), pp. 638–643.

[89] F. Jabeen, V. Grillo, S. Rubini, and F. Martelli, Nanotechnology **19**, 275711 (2008).

[90] S. Wright and H. Kroemer, Appl. Phys. Lett. **36**, 360 (1980).

[91] C. Cochran and L. Foster, J. Electrochem. Soc. **109**, 144 (1962).

[92] E. Kasper, M. Bauer, and M. Oehme, Thin Solid Films **321**, 148 (1998).

[93] A. M. Munshi, D. L. Dheeraj, V. T. Fauske, D. C. Kim, J. Huh, J. F. Reinertsen, L. Ahtapodov, K. D. Lee, B. Heidari, A. T. J. van Helvoort, B. O. Fimland, and H. Weman, Nano Lett. **14**, 960 (2014).

[94] D. Rudolph, L. Schweickert, S. Morkötter, B. Loitsch, S. Hertenberger, J. Becker, M. Bichler, G. Abstreiter, J. J. Finley, and G. Koblmüller, Appl. Phys. Lett. **105**, 033111 (2014).

[95] F. Glas, M. R. Ramdani, G. Patriarche, and J.-C. Harmand, Phys. Rev. B **88**, 195304 (2013).

[96] F. Allegretti, M. Inoue, and T. Nishinaga, J. Cryst. Growth **146**, 354 (1995).

[97] M. Heiß, E. Riedlberger, D. Spirkoska, M. Bichler, G. Abstreiter, and A. F. I. Morral, J. Cryst. Growth **310**, 1049 (2008).

[98] A. C. E. Chia and R. R. LaPierre, J. Appl. Phys. **112**, 063705 (2012).

[99] C. Somaschini, S. Bietti, A. Trampert, U. Jahn, C. Hauswald, H. Riechert, S. Sanguinetti, and L. Geelhaar, Nano Lett. **13**, 3607 (2013).

[100] J. Dufouleur, C. Colombo, T. Garma, B. Ketterer, E. Uccelli, M. Nicotra, and A. Fontcuberta i Morral, Nano Lett. **10**, 1734 (2010).

[101] C. Colombo, M. Heiβ, M. Grätzel, A. F. Morral, and M. Hei, **173108**, (2011).

[102] B. Ketterer, E. Mikheev, E. Uccelli, and A. Fontcuberta i Morral, Appl. Phys. Lett. **97**, 223103 (2010).

[103] O. Salehzadeh, M. X. Chen, K. L. Kavanagh, and S. P. Watkins, Appl. Phys. Lett. **99**, 182102 (2011).

[104] A. Darbandi, O. Salehzadeh, P. Kuyanov, R. R. LaPierre, and S. P. Watkins, J. Appl. Phys. **115**, 234305 (2014).

[105] D. L. Dheeraj, A. M. Munshi, O. M. Christoffersen, D. C. Kim, G. Signorello, H. Riel, A. T. J. van Helvoort, H. Weman, and B. O. Fimland, J. Cryst. Growth **378**, 532 (2013).

[106] A. Okamoto and K. Ohata, J. Electron. Mater. **18**, 111 (1989).

[107] M. Hilse, M. Ramsteiner, S. Breuer, L. Geelhaar, and H. Riechert, Appl. Phys. Lett. **96**, 193104 (2010).

[108] S. Franssila, *Introduction to Microfabrication*, 2nd ed. (John Wiley & Sons, Inc., West Sussex, UK, 2010), pp. 266–267.

[109] B. Zheng, Y. Y. Wu, P. D. Yang, and J. Liu, Adv. Mater. **14**, 122 (2002).

[110] H. Keck and D. J. Broder, Phys. Rev. B **90**, 521 (1953).

[111] K. Suzuki, M. Ito, and Y. Horikoshi, Jpn. J. Appl. Phys. **1**, 6197 (1999).

[112] T. Sugaya, Y. Okada, and M. Kawabe, Jpn. J. Appl. Phys. **2**, 713 (1992).

[113] M. H. Madsen, P. Krogstrup, E. Johnson, S. Venkatesan, E. Mühlbauer, C. Scheu, C. B. Sørensen, and J. Nygård, J. Cryst. Growth **364**, 16 (2013).

[114] K. Ikejiri, T. Sato, H. Yoshida, K. Hiruma, J. Motohisa, S. Hara, and T. Fukui, Nanotechnology **19**, 265604 (2008).

[115] N. V. Sibirev, M. Tchernycheva, M. A. Timofeeva, J.-C. Harmand, G. E. Cirlin, and V. G. Dubrovskii, J. Appl. Phys. **111**, 104317 (2012).

[116] A. I. Persson, L. E. Fröberg, S. Jeppesen, M. T. Björk, and L. Samuelson, J. Appl. Phys. **101**, 034313 (2007).

[117] L. E. Jensen, M. T. Bjork, A. I. Persson, B. J. Ohlsson, and L. Samuelson, Nano Lett. **4**, 1961 (2004).

[118] K. Tomioka, K. Ikejiri, T. Tanaka, J. Motohisa, S. Hara, K. Hiruma, and T. Fukui, J. Mater. Res. **26**, 2127 (2011).

[119] S. Hertenberger, D. Rudolph, M. Bichler, J. J. Finley, G. Abstreiter, and G. Koblmüller, J. Appl. Phys. **108**, 114316 (2010).

[120] M. T. Björk, H. Schmid, C. M. Breslin, L. Gignac, and H. Riel, J. Cryst. Growth **344**, 31 (2012).

[121] D. Rudolph, S. Hertenberger, S. Bolte, W. Paosangthong, D. Spirkoska, M. Döblinger, M. Bichler, J. J. Finley, G. Abstreiter, and G. Koblmüller, Nano Lett. **11**, 3848 (2011).

[122] A. Li, N. V. Sibirev, D. Ercolani, V. G. Dubrovskii, and L. Sorba, Cryst. Growth Des. **13**, 878 (2013).

[123] D. Dalacu, A. Kam, D. Guy Austing, X. Wu, J. Lapointe, G. C. Aers, and P. J. Poole, Nanotechnology **20**, 395602 (2009).

[124] F. Glas, Phys. Status Solidi **247**, 254 (2010).

[125] A. Kelrich, Y. Calahorra, Y. Greenberg, A. Gavrilov, S. Cohen, and D. Ritter, Nanotechnology **24**, 475302 (2013).

[126] M. Niwano, Y. Takeda, Y. Ishibashi, K. Kurita, and N. Miyamoto, J. Appl. Phys. **71**, 5646 (1992).

[127] S. Bae, M. Oh, N. Min, S. Paek, S. Hong, and C. J. Lee, Bull. Korean Chem. Soc. **25**, 1822 (2004).

8 Appendix

8.1 Appendix A: Procedure for Electron Beam Lithography

The following table details the steps involved in the fabrication of a patterned oxide template. The standard EBL preparation and development procedure was developed for use with the EBPG 5000+ EBL instrument at the Toronto Nanofabrication Centre at the University of Toronto:

Procedure Step	Description
Si cleaning "out of the box": • RCA -1 and RCA-2 • Our wafers: Si(111), Sb-doped <0.01 Ω·cm, micro-roughness <5 Å	*Piranha etch (removes organics):* • 10 min in 1:2 HCl:H_2O_2 on 90° C hotplate; rinse in DI water for 2 min. *HCl etch (removes metals, particles):* • 10 min 1:1:4 H_2SO_4:H_2O_2:DI H_2O on 90° C hotplate, rinse in DI water for 2 min. *Oxide etch:* • 5 min 1:10 Buffered HF in H_2O; rinse in DI water for 2 min. • N_2 dry
Oxide Growth/Deposition: • Dry thermal oxides generally used • Uniformity and thickness are more controllable with CVD grown oxides	• Jipelec JetFirst 100 rapid thermal annealer (RTA) dry O_2 environment (~1000 °C). • 200-400 s at fixed 35% lamp power OR • Deposit a 25 nm oxide layer by PE-CVD • Measure oxide thickness using VASE
Cleaning Prior to Spinning Resist: • Degrease, remove dust prior to resist spin	• 1 min ultrasonication in acetone • 1 min ultrasonication in IPA • N_2 dry
Resist Coating: • Typical ZEP-520A prep procedure	• Set hotplate to 180°C • Set spinner to 6000 RPM, acceleration to 587, duration to 60 s • Dispense enough ZEP-520A to create a droplet half the diameter of the substrate • After the resist spin, immediately bake for 3 min at 180°C, place on glass dish to cool • Measure thickness and uniformity using an optical thin film thickness measurement system, ~400 nm expected if spun as specified

Mounting and EBL Writing: • EBL pattern is made in CAD software environment such as L-edit • Pattern file is converted (fractured) Positioning, dosing and markers are added in Layout Beamer software	• Samples mounted to holder using copper clips (# 8 or 10), making certain there is no movement and no lifting due to excessive pressure • Holder placed in HeNe laser Z height measurement station • (X,Y) position zeroed at Faraday cup, Z height zeroed at Si alignment bar • Samples leveled using adjustable set screws on holder axes (Z ± 10 µm) • (X,Y) centre positions for each pattern is measured, input into EBL script • Holder is loaded and final EBL script is run
Development: • Typical ZEP-520A development	• In two beakers pour ZEP-N50 and MIBK:IPA 90:10 • Place substrate in ZEP-N50 for 60 s and gently agitate • Move to MIBK:IPA beaker for 30 s • N_2 dry • Check pattern with light microscope
Pattern transfer: • CF_4 RIE used for SiO_2 etching • 2 min etches ~25 nm of SiO_2 (more reliably than 1 min.) for the E-beam doses used.	• CF_4 RIE etch • 320 mTorr, 8.0 sccm CF_4, 100 W, 1-2 min. duration
Lift-off: • Procedure results in smooth surface free of particulates at high magnification with low kV SEM • Surface considered “clean”	• Soak in ZDMAC for <1 hr • Transfer to new beaker, ultrasonicate in ZDMAC for 5 min • Ultrasonication in acetone for 5 min • Ultrasonication in IPA for 1 min • N_2 dry
Optional: O_2 plasma clean • This procedure is meant to remove residual organics which may have been deposited in the hole using the pattern transfer step in RIE	• 1 min at 100 W, 3 mTorr chamber pressure.
Immediately Prior to MBE Loading: • Used if growing on Si substrate to etch any native oxide from the bottom of the patterned holes • Replacing this step with 40% NH_4F etch, which etches much slower, may be more reliable in future	• 1 min dilute (1%) HF etch • Rinse in DI water and N_2 dry • Immediately load into MBE load lock and evacuate chamber

8.2 Appendix B: MATLAB Code for Secondary Adsorption Growth Model

A MATLAB program was developed to calculate the predicted the NW length and radii using the phenomenological model presented in Chapter 5. The first script "length_radius_vs_pitch" takes in the model parameters, calls the function "ode_soln" to solve the time-dependant ODE and then writes the data to a Microsoft EXCEL file.

```
%% length_radius_vs_pitch- Solve NW length/radius for several pitches and record the data.
 %% MODEL PARAMETERS: (units are nm and min)
t_total = 20; %t_total - the total growth time in min.
r_o = 11; %r_o - initial droplet radius in nm.
r_op = 24; %r_op - oxide opening (hole) radius in nm.
G = 16.66666666667; %G - The nominal thin film growth rate in nm/min.
beta = degtorad(145); %beta - the contact angle of the droplet.
alpha = degtorad(33); %alpha - the incoming angle of the beam.
k1 = 0.8; %k1 - incorporation fraction for axial growth.
k2 = 0.35; %k2 - incorporation fraction for radial growth.
ratio = 1.8; %ratio – the V/III flux ratio during growth.
file_name = 'model_fit_date.xls'; worksheet_name = 'run_#'; %% Create an excel file, worksheet.
%% Write the model parameter labels to the spreadsheet, followed by the values.
variable_labels = [{'run #'} {'t_total (min)'} {'r_o (nm)'}  {'beta (degrees)'} {'k1'}];
xlswrite(file_name, variable_labels, worksheet_name, 'B3');
variables = [{worksheet_name} t_total r_o radtodeg(beta) k1];
 xlswrite(file_name, variables, worksheet_name, 'B4');
variable_labels = [{'G (nm/min)'} {'r_op (nm)'} {'alpha (degrees)'} {'k2'}];
xlswrite(file_name, variable_labels, worksheet_name, 'C5');
variables = [G r_op radtodeg(alpha) k2]; xlswrite(file_name, variables, worksheet_name, 'C6');
%Write the data labels to the spreadsheet.
labels = [{'p(nm)'} {'l(nm)'} {' r(nm)'}];
xlswrite(file_name, labels, worksheet_name, 'B7');
%% Initialize the data storage vector, then fill it.
data = zeros(5,3);
j = 1;
for i = 0:4;
if(i == 0)
p = 250; %p - pattern pitch in nm
sol = ode_soln(t_total,r_o,p,r_op,G,beta,alpha,k1,k2,ratio); %ode_soln – solve the ode
l = sol(end,1); %l - NW length at the end of growth.
r = sol(end,2); %r - NW radius at the end of growth.
data(j,:) = [p l r];
j = j+1;
else
```

```
p = i*500; %p - pattern pitch in nm
sol = ode_soln(t_total,r_o,p,r_op,G,beta,alpha,k1,k2,ratio); %ode_soln – solve the ode
l = sol(end,1); %l - NW length at the end of growth.
r = sol(end,2); %r - NW radius at the end of growth.
data(j,:) = [p l r];
j = j+1;
end
end
%% Write the data to the spreadsheet.
xlswrite(file_name, data, worksheet_name, 'B8');
```

The function “ode_soln” simply calls the built-in MATLAB solver ode45, which uses an variable-step Runge-Kutta Method to solve the ODE system iteratively. The code supplies the solver with the initial conditions and then points to the function “dF_dt” which specifies current state of the ODE in vector form as it evolves with time at each iteration.

```
function ode_soln = ode_soln(t_total,r_o,p,r_op,G,beta,alpha,k1,k2,ratio)
%% ode-soln - solves the non-linear ODE specified by the vector @dF_dt.
%X_o - vector containing the initial conditions for the ODE.
%The initial NW height is assumed to be zero, the initial radis is r_o.
%Units are nm and min.
X_o = [0, r_o];
t_span = [0, t_total];
[t,F] = ode45('dF_dt',t_span,X_o,[],p,r_op,G,beta,alpha,k1,k2,ratio);
ode_soln = [F t];
return
```

The function “dF_dt” sets up the ODE in vector form, with calls to several other functions which each calculate the fraction of reduced adatoms due to the various types of shadowing, given the instantaneous length and radius of the NWs supplied via “ode_soln”.

```
function [dF_dt] = dF_dt(~,F,flag,p,r_op,G,beta,alpha,k1,k2,ratio)
%% dF_dt - Prepares a vector in the form of a non-linear ODE with the axial & radial growth rates.
%F - the instantaneous solution to the ODE computed via ode_soln.
L = F(1,:); %L - the instananeous length of the NWs.
R = F(2,:); %R - the instananeous radius of the NWs.
```

```
 vec = hex_lattice_sites(p,R);  %vector defining the shadowing of scattered flux from the oxide.
norm = vec(:,6); %norm(i) - the distances from (0,0) to the NW at position r(i).
%eta_left(i)/right(i) give the additional shaded fraction behind the left/right of the NW at the site
%identified at lattice point i due to NW_i alone.
eta_left = vec(:,4);
eta_right = vec(:,5);
%eta is the total unshaded fraction of the annular area between the NW identified at site r(i) and
%the NW at site r(i+1). This value must include the contribution of all the previous NW shadows..
%Intialize and calculate eta(i);
eta = ones(size(norm,1),1);
eta(1) = 1-((eta_left(1)+ eta_right(1))/(pi/6));
for k = 2:(size(eta,1));
   eta(k) = eta(k-1)-((eta_left(k)+eta_right(k))/(pi/6));
end
%Initialize unshaded fraction between the NW at (0,0) and the first NW at (0,p). This region does
%not start at zero, however, but starts at r_0.
if(r_op > R)
%If the opening is larger than the current NW radius, which starts at
%t=0 at r_o,the droplet diameter, then we should account for the fact that
%there is no contribution of adatoms from that surface close to the NW.
hole = (pi)*(r_op^2);
hole_shade = ones(size(norm,1),1);
hole_shade(1) = ((0.25*hole)/((pi/12)*((norm(1)^2)-(r_op^2))));
hole_shade(2) = hole_shade(1) + ((0.5*hole)/((pi/12)*((norm(2)^2)-(norm(1)^2))));
hole_shade(3) = hole_shade(2) + ((0.75*hole)/((pi/12)*((norm(3)^2)-(norm(2)^2))));
for k = 4:(size(hole_shade,1));
   hole_shade(k) = hole_shade(k-1)+((hole)/((pi/12)*((norm(k)^2)-(norm(k-1)^2))));
end
r_0 = r_op;
rmin = r_op;
rmax = norm(1);
scattered_flux = (1-hole_shade(1))*droplet_flux(beta,R,L,rmin,rmax);
scattered_flux_2 = (1-hole_shade(1))*(atan(norm(1)/(L))-atan(r_0/(L)));
for k = 1:(size(eta,1)-1)
   unshaded_fraction = eta(k)-hole_shade(k+1);
   if(unshaded_fraction > 1E-6)
   rmin = norm(k);
   rmax = norm(k+1);
   scattered_flux = scattered_flux + (eta(k)-hole_shade(k+1))*droplet_flux(beta,R,L,rmin,rmax);
   scattered_flux_2 = scattered_flux_2 + (eta(k)-hole_shade(k+1))*(atan(norm(k+1)/(L))-
atan(norm(k)/(L)));
   end
end
else
r_0 = R;
rmin = R;
rmax = norm(1);
hole = (pi)*(R^2);
hole_shade = ones(size(norm,1),1);
```

```
hole_shade(1) = ((0.25*hole)/((pi/12)*((norm(1)^2)-(r_op^2))));
hole_shade(2) = hole_shade(1) + ((0.5*hole)/((pi/12)*((norm(2)^2)-(norm(1)^2))));
hole_shade(3) = hole_shade(2) + ((0.75*hole)/((pi/12)*((norm(3)^2)-(norm(2)^2))));
for k = 4:(size(hole_shade,1));
   hole_shade(k) = hole_shade(k-1)+((hole)/((pi/12)*((norm(k)^2)-(norm(k-1)^2))));
end

scattered_flux = (1-hole_shade(1))*droplet_flux(beta,R,L,rmin,rmax);
scattered_flux_2 = (1-hole_shade(1))*(atan(norm(1)/(L))-atan(r_0/(L)));
for k = 1:(size(eta,1)-1)
   unshaded_fraction = eta(k)-hole_shade(k+1);
   if(unshaded_fraction > 1E-6)
   rmin = norm(k);
   rmax = norm(k+1);
   scattered_flux = scattered_flux + (eta(k)-hole_shade(k+1))*droplet_flux(beta,R,L,rmin,rmax);
   scattered_flux_2 = scattered_flux_2+(eta(k)-hole_shade(k+1))*(atan(norm(k+1)/(L))-
atan(norm(k)/(L)));
end
end
end
dL_dt = G*ratio*k1*(1/(sin(beta)^2)+ substrate_shadow(L,R,p,alpha)*scattered_flux);
dR_dt = G*k2*(sidewall_shadow(L,R,p,alpha)*sin(alpha)/pi+(1/pi)*(sidewall_shadow(L,R,p,alpha)
*substrate_shadow(L,R,p,alpha))*scattered_flux_2);
dF_dt = [dL_dt;dR_dt];
return
end
```

The function “droplet_flux” computes the magnitude of the scattered flux collected by the droplet (without shading). This is done by solving Equation (5.6).

```
function [droplet_flux] = droplet_flux(beta,R,L,rmin,rmax)
%% droplet_flux - calculates the magnitude of the scattered flux on the droplet.
R_d = (R/sin(beta));
h = (R_d*cos(beta));
lmin = L;
lmax = (L-h+R_d);
fun1 = @(l,r)(2.*(l.^2).*cos(asin((h+(l-L))./(R_d))).*sin(asin((h+(l-L))./(R_d))).*r)./((r.^2+l.^2).^2);
fun2 = @(l,r)(2.*l.*cos(asin((h+(l-L))./(R_d))).*cos(asin((h+(l-L))./(R_d))).*r.^2)./((r.^2+l.^2).^2);
int1 = integral2(fun1,lmin,lmax,rmin,rmax);
int2 = integral2(fun2,lmin,lmax,rmin,rmax);
droplet_flux = (2)/(pi*R*sin(beta))*(int2-int1);
return
```

The function “sidewall_shadow” computes the reduction of adatoms due to shadowing of direct sidewall flux due to the shadows of neighboring NWs. This takes into account

the incoming angle of the MBE beam and the fact that the substrate rotates during growth. See Figure 5.4 (c) for an example of the calculated results.

```
function [sidewall_shadow] = sidewall_shadow(L,R,p,alpha)
% sidewall_shadow - calculates the degree of sidewall shadowing due to neighboring nanowires.
 %L - the instananeous length of the NWs.
%R - the instananeous radius of the NWs.
%p - the pitch of the array.
%alpha - the angle of the incoming beam.
%Intitialize vec, the data vector defining the shadowing of the scattered flux from the oxide;
vec = hex_lattice_sites(p,R);
%norm(i) gives the distances from (0,0) to the NW at position r(i) in the periodic section pi/4.
norm = vec(:,6);
vx = vec(:,1);
vy = vec(:,2);
ratio = 0;
for k = 1:size(norm,1)
if(L*tan(alpha) > norm(k))
shadow_rectangle = (L*tan(alpha)-norm(k))*2*R;
full_sidewall = L*sin(alpha)*2*R;
phi_k = atan(vx(k)/vy(k));
phi_k_min = phi_k -2*atan(R/norm(k));
phi_k_max = phi_k + 2*atan(R/norm(k));
fun1 = @(phi)(1-((abs(phi-phi_k)/(2*atan(R/norm(k))))))*(shadow_rectangle/full_sidewall);
int1 = integral(fun1,phi_k_min,phi_k_max);
ratio = ratio + (int1)*(pi/4);
end
end
sidewall_shadow = (1-ratio);
return
```

The function “substrate_shadow” computes the degree of shadowing of direct flux hitting the oxide surface between the NWs due to the shadows of neighboring NWs. This takes into account the incoming angle of the MBE beam and the fact that the substrate rotates during growth. See Figure 5.4 (d) for an example of the calculated results.

```
function [substrate_shadow] = substrate_shadow(L,R,p,alpha)
%% substrate_shadow - calculates the degree of substrate shadowing due to neighboring NWs.
 %L - the instananeous length of the NWs.
%R - the instananeous radius of the NWs.
```

```
%p - the pitch of the array.
%alpha - the angle of the incoming beam.
%Intitialize vec, the data vector defining the shadowing of the scattered flux from the oxide;
vec = hex_lattice_sites(p,R);
%norm(i) gives the distances from (0,0) to the NW at position r(i) in the periodic section pi/4.
norm = vec(:,6);
vx = vec(:,1);
vy = vec(:,2);
ratio = (L*tan(alpha)*2*R)/(pi*p^2); %initalize; always the shadow of the central NW itself
for k = 1:(size(norm,1)-1)
if(L*tan(alpha) > norm(k))
shadow_rectangle = (L*tan(alpha)-norm(k))*2*R;
phi_k = atan(vx(k)/vy(k));
phi_k_min = phi_k -2*atan(R/norm(k));
phi_k_max = phi_k + 2*atan(R/norm(k));
fun1 = @(phi)(1-((abs(phi-phi_k)/(2*atan(R/norm(k))))))*(shadow_rectangle/(pi*norm(k)^2));
int1 = integral(fun1,phi_k_min,phi_k_max);
ratio_sidewall = (int1)*(pi/6);
ratio = ratio + (1/4)*(L*tan(alpha)*2*R)/(pi*norm(k)^2)+
(3/4)*(L*tan(alpha)*2*R)/(pi*norm(k+1)^2)-ratio_sidewall;
else
ratio = ratio + (L*tan(alpha)*2*R)/(pi*norm(k)^2);
end
end
substrate_shadow = (1-ratio);
if(substrate_shadow < 0)
substrate_shadow = 0;
end
return
```

The function “hex_lattice_sites” computes all of the lattice sites (divided into even and odd for efficiency) which contribute to “line-of-sight” substrate shading in a 30° area of interest (which is all that is required since the hexagonal array is symmetric). NWs which are blocked in the line-of-sight of a previous NW are not taken into account. It then computes the shaded area fraction on the left and right of each contributing NW, taking into account any partial overlaps between shadows. See Figure 5.4 (b) for an example of the calculated results.

```
function vectors = hex_lattice_sites(p,r)
```

```
%hex_lattice_sites - returns all vectors pointing to the contributing lattice positions in the
%hexagonal array, in order of increasing length. Also computes and stores the unshaded
%fractional annular area (eta_total). It is truncated when eta_total is zero.
 %INPUTS:
%p - pitch of the hexagonal array.
%r - the instantaneous radius of the NWs.
 %Initalize all_v with the shortest odd vector r1, which is not otherwise accounted for in the sum.
v1 = [1/2*p (sqrt(3)/2)*p];
norm1 = norm(v1,2);
%Initialize the total unshaded fractional annular area, eta_total, using the first nearest neighbor
%NW, which only contributes 1/2 of its angle to the shading.
eta_left = atan(r/norm1);
eta_right = 0;
eta_total = 1-((eta_left + eta_right)/(pi/6));
unit_v = [0 1]; %Initialize a unit vector in the y direction.
theta = acos(dot(unit_v,v1)/(norm1)); %Initialize angle between current vec. and the unit_v vec.
all_v  = zeros(50,6); %Add the final 4 columns to all_v
all_v(1,:) = [v1 theta eta_left eta_right norm1];
i = 0; j = 1; %initialize the counters, i for "x-coordinate " and j for "y-coordinate".
v_even = [i*p j*(sqrt(3))*p]; %All of the "even" lattice sites, specified by the vector v_even.
v_odd = [0.5*i*p j*(sqrt(3))*p]; %All of the "odd" lattice sites, specified by the vector v_odd.
%The second nearest-neighbor bounds the 30 deg. area of interest.
norm1 = norm(v_even,2);
theta = acos(dot(unit_v,v_even)/norm1);
eta_left = 0;
eta_right = atan(r/norm1);
eta_total = eta_total - ((eta_left + eta_right)/(pi/6));
all_v(2,:) = [v_even theta eta_left eta_right norm1];
rows = 2;.
i = 1;    j = 1.5;
v_odd = [0.5*i*p j*sqrt(3)*p];
norm1 = norm(v_odd,2);
eta_left = atan(r/norm1);
eta_right = atan(r/norm1);
theta_odd = acos(dot(unit_v,v_odd)/norm1);
while(eta_total > 1E-6)
%Start by going through a row of odd lattice sites, where i starts at one.
while(theta_odd < (pi/6))
l = 0; %First, initialize l = 0;
 %Is this NW directly in the shadow of any of the NWs already accounted for?
%Search the 3rd column of all_v. If an equal theta_even has already been
%recorded, then assign l > 1 and do not add this NW position to the total.
for k = 1:rows
if(abs(theta_odd - all_v(k,3))< 1E-6)
l = l+1;
end
end
if(l == 0)
%If l=0, append this vector onto the total.
```

```
rows = rows+1;
all_v(rows,:) = [v_odd theta_odd eta_left eta_right norm1];
%Use this value of eta_left and eta_right in the calculation of the total
%unshaded fractional annular area up to this point.
total = sum(all_v);
eta_total = 1-((total(4)+total(5))/(pi/6));
if(eta_total < 1E-6)
   break;
end
end
%Increase i by 2 and look at the next odd lattice site.
i = i+2;
v_odd = [0.5*i*p j*sqrt(3)*p];
norm1 = norm(v_odd,2);
eta_left = atan(r/norm1);
eta_right = atan(r/norm1);
theta_odd = acos(dot(unit_v,v_odd)/norm1);
end
%Now that we have scanned to the boundary of the region of interest (pi/6),
%we need to re-initialize i to back to 1 and add 1/2 to j
%in order to go through the next row of even lattice sites.
i = 1; j = j+0.5;
v_even = [i*p j*sqrt(3)*p];
norm1 = norm(v_even,2);
eta_left = atan(r/norm1);
eta_right = atan(r/norm1);
theta_even = acos(dot(unit_v,v_even)/norm1);
while(theta_even < (pi/6))
 l = 0;
for k = 1:rows
if(abs(theta_even - all_v(k,3))< 1E-6)
l = 1;
end
end
if(l == 0)
%If the angle is new, append this vector onto the total.
rows = rows+1;
all_v(rows,:) = [v_even theta_even eta_left eta_right norm1];
%Use this value of eta_left and eta_right in the calculation of the total
%unshaded fractional annular area up to this point.
total = sum(all_v);
eta_total = 1-((total(4)+total(5))/(pi/6));
if(eta_total < 1E-6)
   break;
end
end
i = i+1; %Increase i by 1 and look at the next even lattice site.
v_even = [i*p j*sqrt(3)*p];
norm1 = norm(v_even,2);
```

```
eta_left = atan(r/norm1);
eta_right = atan(r/norm1);
theta_even = acos(dot(unit_v,v_even)/norm1);
end
i = 1;j = j + 0.5; %Go back to the odd sites
v_odd = [0.5*i*p j*sqrt(3)*p];
norm1 = norm(v_odd,2);
eta_left = atan(r/norm1);
eta_right = atan(r/norm1);
theta_odd = acos(dot(unit_v,v_odd)/norm1);
end
%. The vectors pointing to the contributing lattice points have all been calculated.  Remove any
extra rows and re-sort all_v in order of increasing length.
while(size(all_v,1) > rows)
all_v(rows+1,:)= [];
end
all_v = sortrows(all_v,6);
vectors = all_v; return
```